Studies on The Giant Magnetoresistance in Magnetic Superlattices(Dissertation_全文)

AUTHOR(S):

Suzuki, Motofumi

Studies on

The Giant Magnetoresistance in Magnetic Superlattices

Motofumi Suzuki

1997

Acknowledgment

I would like to express my sincere gratitude to Professor Michi-hiko Mannami of Kyoto University for the guidance, constructive suggestions, discussions and encouragement throughout this study.

I would also like to thank Professor Masayuki Shiga and Professor Takashi Fujimoto of Kyoto University for their critical suggestion and reading.

I am especially indebted to Dr. Yasunori Taga of TOYOTA Central Research and Development Laboratories, Inc. (TCRDL) for his continuous support, valuable discussions, advises and encouragement over the period of this study.

I would like to acknowledge Professor Hiroshi Yasuoka and Dr. Atushi Goto of Institute of Solid State Physics of University of Tokyo for useful discussions and the support for NMR measurements.

I wish to thank members of Special Research Laboratory in TCRDL. I would like to my sincere thanks to Dr. Takeshi Ohwaki and Mr. Kengo Ishiyama for their useful discussions and advises. The skilled technical assistance and advises provided by Ms. Yuko Aoki, Ms. Atuko Inoue, Mr. Atsushi Miura, Mr. Takahiro Shiga and other members are also appreciated. Without their helps, this work could not be completed.

I am grateful to Dr. Akira Hosono of TCRDL for their support for this study and giving me the opportunity to prepare this thesis.

I would like to express my gratitude to Dr. Osami Kamigaito and Dr. Riichi Takahashi of TCRDL for giving me a excellent circumstance and chance to prepare this thesis.

Finally, I wish deeply to express my appreciation to my wife Miho and our parents for their encouragement throughout of this study. This thesis is dedicated to Miho and my son Kai.

Contents

1 Introduction **1**
1.1 Prior to discovery of GMR 2
1.2 GMR and AF coupling in magnetic superlattices 4
1.3 Origin of the GMR 7
1.4 Outline 9
References 11

2 Experiments **17**
Abstract 17
2.1 Preparation of Co/Cu superlattices 18
2.2 Characterization 19
2.2.1 Measurements of GMR and magnetization 19
2.2.2 X-ray diffraction 19
2.2.3 ^{59}Co NMR 20
References 22

3 Role of buffer layer in GMR **23**
Abstract 23
3.1 Introduction 24
3.2 Experiments 24
3.3 Results and discussion 25
3.3.1 Relationship between GMR and thicknesses of Co and Cu 25
3.3.2 Critical thickness of Fe buffer layer 27
3.3.3 Dependence of GMR on substance of buffer layer . . . 32
3.4 Conclusion 33
References 34

4 Interfacial structure of Co/Cu superlattices 37
Abstract . . . 37
4.1 Introduction . . . 38
4.2 Experiment . . . 39
4.3 Results and discussion . . . 40
4.3.1 XRD . . . 40
4.3.2 NMR . . . 45
4.4 Conclusion . . . 51
References . . . 52

5 GMR in Co/Cu superlattices with mixed interfaces I 57
Abstract . . . 57
5.1 Introduction . . . 58
5.2 Experiment . . . 59
5.3 Results and discussion . . . 59
5.4 Conclusion . . . 66
References . . . 67

6 GMR in Co/Cu superlattices with mixed interfaces II 69
Abstract . . . 69
6.1 Introduction . . . 70
6.2 Experiment . . . 71
6.3 Results and discussion . . . 72
6.3.1 Relationship between GMR and magnetization . . . 72
6.3.2 Temperature dependence of GMR . . . 78
6.4 Conclusion . . . 84
References . . . 85

7 Influence of bound *d* state on GMR 89
Abstract . . . 89
7.1 Introduction . . . 90
7.2 Model . . . 91
7.3 Superlattice state for d band . . . 94
7.4 Calculation of resistivity . . . 95
7.4.1 s–s scattering . . . 96
7.4.2 s–d scattering . . . 97
7.5 GMR . . . 99
7.6 Interfacial scattering in Co/Cu . . . 102
7.7 Conclusion . . . 106
References . . . 107

8 GMR sensors using Co/Cu superlattices 111
Abstract 111
8.1 Introduction 112
8.2 Experiments 113
8.3 Results and discussion 117
8.3.1 Refinement of Co/Cu superlattices 117
8.3.2 Characteristics of GMR sensors 118
8.3.3 Thermal durability of GMR sensors 123
8.4 Conclusion 126
References 127

List of Publications 129

Chapter 1

Introduction

This thesis is on the studies on the giant magnetoresistance (GMR) in Co/Cu superlattices. The transport properties of Co/Cu superlattices have been experimentally investigated with the special emphasis on the relationship between the magnetoresistance (MR) and the superlattices structures, which include the crystallographic, long- and short-range interfacial roughness. The theoretical model consistent with the experimental results has been also proposed. Furthermore, we have demonstrated the usefulness of the GMR in Co/Cu superlattices for the practical application to the magnetic rotation sensor.

In this chapter, brief introduction to the GMR in metallic multilayers and the outline of this thesis are described.

1.1 Prior to discovery of GMR

The physical properties of the artificial nanostructured materials have been studied since a hundred years ago. The optical properties of the metallic fine particles embedded in the dielectric materials were initiated at the beginning of this century by Maxwell Garnett [1, 2], and are still active in the various field in present [3]. Although, the studies on the artificial multilayered materials prepared by vacuum deposition also have a long history, the vacuum condition before 1960's was not heigh enough to produce reliable samples. Around 1970, ultra high vacuum techniques have been introduced in the field of material fabrication, studies on the semiconductor superlattices were initiated by Esaki's group [4]. Recently, even a monolayer–monolayer superlattices of GaAs/AlAs has been successfully synthesized [5].

On the other hand, it is past 1980's that significant developments in the

research on physical properties of metallic superlattices have been made, although x-ray optics of the metallic multilayers were investigated before 1960's. Prior to the discovery of the GMR, most researchers have focused their attention on the magnetism and the superconductivity among the fundamental physical properties of metallic superlattices, since the superlattices are useful to investigate magnetic anomalies at interfaces and properties of two-dimensional magnetic systems. In these studies, many interesting phenomena have been found such as the enhancement of the magnetic moment of Ni atoms at interfaces between Ni and Cu [6, 7] and perpendicular magnetization in Co/Pd superlattices [8].

The peculiar magnetic structure in Fe/Cr/Fe sandwich films found by Grünberg *et al.* in 1986 is one of the most important discovery in the studies on the metallic superlattices [9]. They found the strong antiferromagnetic (AF) coupling between two ferromagnetic (F) Fe layers. Due to the AF coupling, magnetization of Fe layers align antiparallel in the weak magnetic field, while they align parallel in the stronger field than the saturation. They also measured the magnetoresistance (MR) in these sandwich films. Unfortunately, measured MR ratio, which is the relative change in resistivity, is less than 1 %, so that this work did not attract the attention from the standpoint of the MR effect. However, it is clear that this work is on the frontiers of the discovery of GMR.

1.2 GMR and AF coupling in magnetic superlattices

Following the work of Grünberg *et al.*, Fert's group have prepare Fe/Cr superlattices, and have measured transport properties [10]. As the results, it has been found that the resistance in $[\mathrm{Fe}(3.0\ \mathrm{nm})/\mathrm{Cr}(0.9\ \mathrm{nm})]_n$ ($n = 60$) superlattice at 0 field decreases down to the half value at the magnetic field of 20 kOe as shown in Fig. 1.1, where the subscript n indicates the number of bilayers in the sample. This is the first report on the GMR in magnetic superlattices and made a great impact on the fundamental and applied physics. Since the samples with large MR ratio had the small remanence magnetization, they considered that the magnetization of the adjacent Fe layers aligned antiparallel in the weak magnetic field due to the strong AF interlayer coupling, while the magnetization of Fe layers aligned parallel in the magnetic field large enough to predominate over the AF coupling. In Fig. 1.1, proposed configuration of the magnetization of Fe layers is indicated. In fact, the AF alignment was confirmed immediately by neutron diffraction [11].

Relating to the change in the magnetic structure, the GMR is understood phenomenologically as follows: In the ferromagnetic metals, the current is carried separately by up- and down-spin conduction electrons (two-current model) as [12]

$$\rho = \frac{\rho_\uparrow \rho_\downarrow}{\rho_\uparrow + \rho_\downarrow}, \tag{1.1}$$

where $\rho_\uparrow$ and $\rho_\downarrow$ are the resistivity of up- and down-spin channels, respectively, and ρ is the total resistivity. Moreover, it is known that the scattering of conduction electrons can be strongly spin dependent in a ferromagnetic

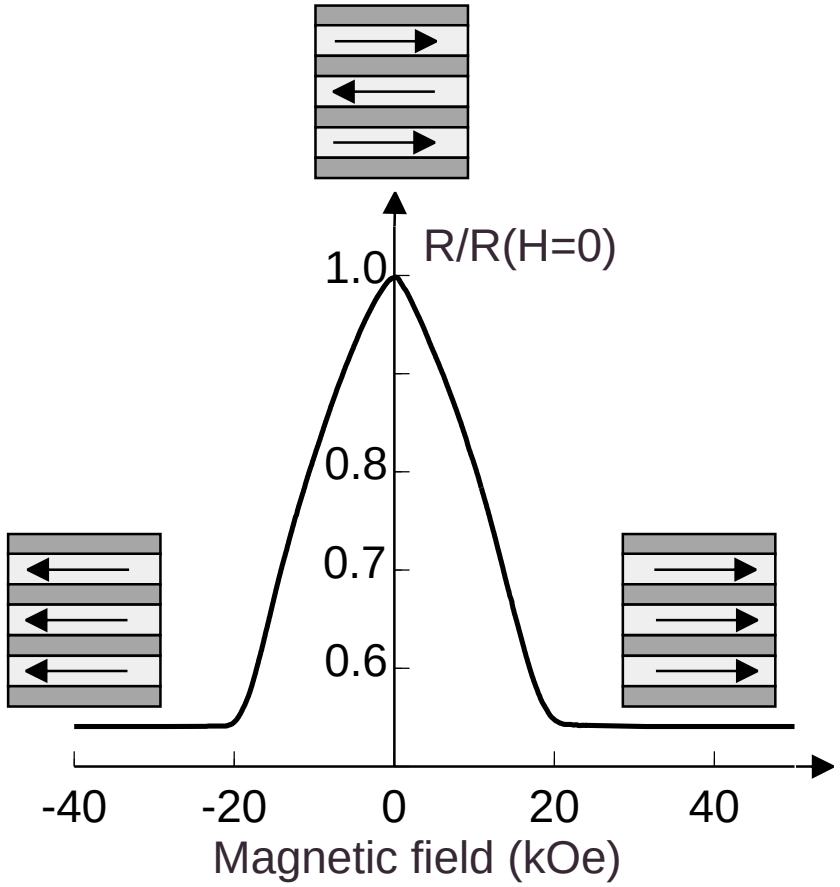

Fig. 1.1: Magnetoresistance of the Fe/Cr superlattice at 4.2 K [10]. The current and the applied field are in the plane of the layers. Allows indicate the schematic configuration of the magnetization of Fe layers.

transition metal ($\rho_\uparrow \gg \rho_\downarrow$ or $\rho_\uparrow \ll \rho_\downarrow$). In the superlattices in ferromagnetic (F) alignment, electrons of one spin direction always travel in the channel of small resistivity, while electrons of another spin direction travel in the channel of large resistivity. On the other hand, in the superlattices in AF alignment, electrons of both spin directions alternately travel in the channels of small and large resistivity. Therefore, total resistivity for F alignment becomes much smaller than that for AF alignment.

The discovery of the GMR in magnetic superlattices raised two questions on the origins of the AF interlayer coupling and the mechanism of the spin-dependent conduction electron scattering. These problems have attracted much attention from both fundamental and practical standpoints. Other than the Fe/Cr superlattices, the GMR and the AF interlayer coupling have been observed in the various systems such as Co/Cu [13, 14], NiFe/Cu [15], CoFe/Cu [16] and Co/Ag [17]. Especially the transition metal/Cu systems are significant for the practical application to the MR sensors, since their MR ratio is considerably large even at room temperature, and the saturation field is small. Moreover, Parkin *et al.* reported remarkable results on the GMR and the interlayer coupling in superlattices [14, 18]. They measured the MR ratio and the magnetization curves as a function of the thickness of the nonmagnetic layer, so that the magnitude of the MR ratio and the saturation field were found to oscillate with the nonmagnetic layer thickness with a period of 10–15 Å (see Fig 3.1 in Chapter 3). This oscillation has been attributed to that the interlayer exchange coupling between the adjacent magnetic layers oscillates between F and AF coupling as a function of the nonmagnetic layer thickness. According to this interpretation, the interlayer exchange coupling plays an important role in the GMR in superlattices.

For the GMR, however, the interlayer coupling is not essential, but the AF alignment of the magnetization of the adjacent magnetic layers is. In fact, Shinjo and Yamamoto reported the GMR in the superlattices in which the adjacent magnetic layers were not coupled [19]. They prepared a superlattice of $[\mathrm{Co}(30\ \text{Å})/\mathrm{Cu}(50\ \text{Å})/\mathrm{NiFe}(30\ \text{Å})/\mathrm{Cu}(50\ \text{Å})]_{15}$. In this superlattice, AF alignment of the magnetization was achieved by the difference in the co-

ercive force of two magnetic layers, since Co and NiFe are magnetically hard and soft materials, respectively. Another uncoupled sandwich structure, the so-called spin valve, is proposed as the sensitive GMR system [20–23]. In the spin valve structure, the magnetization of magnetic layers is aligned antiferromagnetically by pinning the magnetization of one of the ferromagnetic layers using the exchange-biasing layer. Therefore, the GMR and the interlayer exchange coupling are the problems independent of each other. The theme of this thesis is the GMR in Co/Cu superlattices, so that we will not enter into detailed discussions on the interlayer exchange coupling.

1.3 Origin of the GMR

The origin of the GMR can be attributed to the spin-dependent scattering of conduction electrons as described in the previous section. However, mechanism of the spin-dependent scattering still remains unclear. Many experimental studies deal with the correlation between the GMR and the interfacial roughness to understand the role of interfaces [15,24–27]. For Fe/Cr superlattices [24, 25], the enhancement of both the magnitude and temperature dependence of the GMR due to interfacial roughness has been reported, so that the origin of the GMR in Fe/Cr is attributed to the interfacial scattering [28]. However, for transition metal (M)/Cu superlattices, no one has reported that the interfacial roughness enhances the GMR [15, 26, 27]. This suggests that the spin-dependent bulk scattering is important for the occurrence of the GMR. Nevertheless, the importance of interfacial scattering has been pointed out indirectly in studies on the layer thickness dependence of the GMR [29, 30]. Parkin [29] has reported that the GMR is enhanced by

very thin Co layers inserted at interfaces of NiFe/Cu multilayers. He claimed that the *interfacial state* as well as roughness plays an important role in the GMR. These experimental results require a theory to take account of both the spin-dependent bulk scattering and the interfacial electronic states.

On the other hand, there are many theoretical studies discussing the origin of the GMR. Camley and Barnaś [31, 32] have proposed a semi-classical model for the GMR by extending the Fuchs-Sondheimer model [33, 34]. In their model, the GMR is described with many phenomenological parameters for conduction electrons such as spin-dependent mean free paths in layers, reflection, transmission and diffuse scattering coefficients at interfaces. Quantum mechanical models by Hood and Falicov [35] and by Visscher [36] relate these phenomenological parameters to superlattice potentials and the potentials of bulk and interfacial scatterers. Since these theories are based on a single band free electron model, spin-dependent scattering is attributed to spin-dependent potentials. For Fe/Cr superlattices, the spin-dependent potentials due to interfacial roughness have been indicated by microscopic theories [37–39].

In discussing the GMR in M/Cu, however, the above theories are not appropriate, since they do not include the information about the band structure being very different from that of Fe/Cr. If we take account of the electronic band structure, the formalism for the bulk and interfacial scattering will be modified. For M/Cu systems, Edwards *et al.* [40] claimed in their resistor network theory that the spin-dependent s–d scattering in bulk is the dominant process giving arise to the GMR. Xing *et al.* [41, 42] also insist on the importance of spin-dependent density of states (DOS) of d bands in magnetic

layers. In these models, the GMR is attributed to the scattering of s electrons into unfilled d bands which have spin-dependent DOS. These models semi-quantitatively agree with the layer thickness dependence of GMR in M/Cu systems. However, the influence of the interfacial state has not been treated explicitly, since the Fermi surfaces of s and d bands are treated as simple spheres. Recently, Schep *et al.* [43] calculated the GMR in a method based on the full electronic structure. They reported the importance of the s–d hybridization for the origin of the GMR in the current-perpendicular-to-the-plane (CPP) geometry. However, their theory does not satisfactorily explain the considerable MR observed in the current-in-the-plane (CIP) geometry. They suggest that some additional scattering mechanism is necessary for explaining the CIP MR. The mechanism of the GMR in M/Cu superlattices still remains unclear.

In this thesis, we discuss the origin of the GMR in Co/Cu superlattices based on the experimental data for the Co/Cu superlattices with well-controlled interfacial roughness and the theoretical s–d scattering model taking account of the interfacial states.

1.4 Outline

The outline of this thesis is as follows:

Chapter 2 describes the experimental methods; preparation of samples and the structural analysis by using the x-ray diffraction and the NMR.

In Chapter 3, the characteristic features of the GMR and the structures of Co/Cu superlattices deposited on various buffer layers are surveyed. A drastic changes in the MR ratio and the saturation field are found, depending

on the thickness and the substance of the buffer layer. The strong correlation between the GMR and the structures is discussed briefly.

In Chapter 4, an attempt is made to clarify the effect of interfacial mixing on the x-ray diffraction (XRD) and ^{59}Co NMR of Co/Cu superlattices. Systematic and quantitative modification of interfaces has been achieved by codeposition of Co and Cu at interfaces. We show that high and low angle XRD patterns are not affected by the existence of compositionally mixed regions thinner than 0.3 nm, and that significant change in the distribution of hyperfine field of ^{59}Co is found.

In Chapter 5 and 6, the detailed GMR and magnetic properties of the Co/Cu superlattices with intentionally mixed interfaces are shown. The results are discussed using the spin-split DOS model of Xing *et al.* [41, 42]. The magnetization dependence of the GMR has precluded the existence of a strong spin dependence in the potential not only for the bulk but also for the interfacial scattering. The temperature dependence of the GMR is hardly influenced by the interfacial roughness, while the residual resistivity changes significantly. This reveals that the spin-dependent s–d scattering in the bulk is crucial for the GMR in Co/Cu superlattices. The interfacial roughness mainly contributes to the residual resistivity, and the spin dependence in the scattering at interfaces is weaker than that in the bulk.

In Chapter 7, we discuss theoretically the GMR in magnetic superlattices with an s–d scattering model on the assumption that d states are bound in magnetic layers. The GMR is calculated by using the quantum Boltzmann equation using Kronig-Penney type potentials. Spin-dependent interfacial scattering depends on the number of scatterers, the height of the scatter-

ing potentials and the amplitude of the wave function of the d state at interfaces, while spin-dependent bulk scattering is attributed to the spin-dependent DOS of d states. Our model agrees well with the measured GMR in Co/Cu superlattices with artificially mixed interfaces, when we assume that the minority spin d states are strongly bound in Co layers. Therefore, the spin-dependent scattering in Co/Cu superlattices is attributed to the spin-dependent DOS of the d states in the Co layers.

Finally, in Chapter 8, we demonstrate the usefulness of the GMR in Co/Cu superlattices for the practical application to the magnetic rotation sensor. Optimized Co/Cu superlattices have been fabricated into the sensors with appropriate passivation layers. The sensor output changes more than 20% synchronizing the rotation of magnet rotor. It is remarkable that the degradation of the GMR sensors is not significant even after the sensors are left in air at 150 °C for 1000 h. This confirms the high reliability of the GMR sensors and promises us that the GMR sensors can be used in automobiles and aircraft under the sever conditions.

References

[1] J. C. Maxwell Garnett, Philos. Trans. R. Soc. London, Ser. A **203**, 385 (1904).

[2] J. C. Maxwell Garnett, Philos. Trans. R. Soc. London, Ser. A **205**, 237 (1906).

[3] M. Suzuki and Y. Taga, J. Appl. Phys. **71**, 2848 (1992).

[4] P. Voisin, G. Bastard, C. E. T. Goncalves da Silva, M. Voos, L. L. Chang, and L. Esaki, Solid State Commun. **39**, 79 (1981).

[5] H. Terauchi, S. Sekimoto, K. Kamigaki, H. Sakashita, N. Sano, H. Kato, and M. Nakayama, J. Phys. Soc. Jpn. **54**, 4576 (1985).

[6] B. J. Thaler and J. B. Ketterson, Phys. Rev. Lett. **41**, 336 (1978).

[7] E. M. Gyorgy, D. B. McWhan, J. E. Dillon Jr., L. R. Walker, and J. V. Waszczak, Phys. Rev. B **25**, 6739 (1982).

[8] P. F. Carcia, A. D. Meinhaldt, and A. Suna, Appl. Phys. Lett. **47**, 178 (1985).

[9] P. Grünberg, R. Schreiber, Y. Pang, M. B. Brodsky, and H. Sower, Phys. Rev. Lett. **57**, 2442 (1986).

[10] M. N. Baibich, J. M. Broto, A. Fert, F. Nguyen Van Dau, F. Petroff, P. Etienne, G. Creuzet, A. Friederich, and J. Chazelas, Phys. Rev. Lett. **61**, 2472 (1988).

[11] N. Hosoito, S. Araki, K. Mibu, and T. Shinjo, J. Phys. Soc. Jpn. **59**, 1925 (1990).

[12] A. Fert and I. A. Campbell, J. Phys. C **6**, 849 (1976).

[13] D. H. Mosca, F. Petroff, A. Fert, P. A. Schroeder, W. P. Pratt Jr., and R. Laloee, J. Magn. Magn. Mater. **94**, L1 (1991).

[14] S. S. P. Parkin, R. Bhadra, and K. P. Roche, Phys. Rev. Lett. **66**, 2152 (1991).

[15] V. S. Speriosu, J. P. Nozieres, B. A. Gurney, B. Dieny, T. C. Huang, and H. Lefakis, Phys. Rev. B **47**, 11579 (1993).

[16] Y. Saito, S. Hashimoto, and K. Inomata, Appl. Phys. Lett. **60**, 2436 (1992).

[17] W. P. Pratt Jr., S. F. Lee, J. M. Slaughter, R. Loloee, P. A. Schroeder, and J. Bass, Phys. Rev. Lett. **66**, 3060 (1991).

[18] S. S. P. Parkin, N. More, and K. P. Roche, Phys. Rev. Lett. **64**, 2304 (1990).

[19] T. Shinjo and H. Yamamoto, J. Phys. Soc. Jpn. **59**, 3061 (1990).

[20] B. Dieny, V. S. Speriosu, S. S. P. Parkin, B. A. Gurney, D. R. Wilhoit, and D. Mauri, Phys. Rev. B **43**, 1297 (1991).

[21] B. Dieny, V. S. Speriosu, S. Metin, S. S. P. Parkin, B. A. Gurney, P. Baumgart, and D. R. Wilhoit, J. Appl. Phys. **69**, 4774 (1991).

[22] A. Chaiken, P. Lubitz, J. J. Krebs, G. A. Prinz, and M. Z. Harford, Appl. Phys. Lett. **59**, 240 (1991).

[23] A. Chaiken, P. Lubitz, J. J. Krebs, G. A. Prinz, and M. Z. Harford, J. Appl. Phys. **70**, 5864 (1991).

[24] F. Petroff, A. Barthélémy, A. Hamzić, A. Fert, P. Etienne, S. Lequien, and G. Creuzet, J. Magn. Magn. Mater. **93**, 95 (1991).

[25] E. E. Fullerton, D. M. Kelly, J. Guimpel, I. K. Schuller, and Y. Bruynseraede, Phys. Rev. Lett. **68**, 859 (1992).

[26] M. J. Hall, B. J. Hickey, M. A. Howson, C. Hammond, M. J. Walker, D. G. Wright, D. Greig, and N. Wiser, J. Phys. Condens. Mater. **4**, L495 (1992).

[27] Y. Saito, K. Inomata, A. Goto, and H. Yasuoka, J. Phys. Soc. Jpn. **62**, 1450 (1993).

[28] S. Zhang and P. M. Levy, Phys. Rev. B **43**, 11048 (1991).

[29] S. S. P. Parkin, Phys. Rev. Lett. **71**, 1641 (1993).

[30] S. K. J. Lenczowski, M. A. M. Gijs, J. B. Geisbers, R. J. M. van de Veerdonk, and W. J. M. de Jonge, Phys. Rev. B **50**, 9982 (1994).

[31] R. E. Camley and J. Barnaś, Phys. Rev. Lett. **63**, 664 (1989).

[32] J. Barnaś, A. Fuss., R. E. Camley, P. Grünberg, and W. Zinn, Phys. Rev. B **42**, 8110 (1990).

[33] K. Fuchs, Proc. Cambridge Philos. Soc. **34**, 100 (1938).

[34] E. H. Sondheimer, Adv. Phys. **1**, 1 (1952).

[35] R. Q. Hood and L. M. Falicov, Phys. Rev. B **46**, 8287 (1992).

[36] P. B. Visscher, Phys. Rev. B **49**, 3907 (1994).

[37] P. M. Levy, S. Zhang, and A. Fert, Phys. Rev. Lett. **65**, 1643 (1990).

[38] P. M. Levy, S. Zhang, and A. Fert, Phys. Rev. B **45**, 8689 (1992).

[39] J. Inoue, A. Oguri, and S. Maekawa, J. Phys. Soc. Jpn. **60**, 376 (1991).

[40] D. M. Edwards, J. Mathon, and R. B. Muniz, IEEE Trans. Magn. **27**, 3548 (1991).

[41] L. Xing and Y. C. Chang, Phys. Rev. B **48**, 4156 (1993).

[42] L. Xing, Y. C. Chang, M. B. Salamon, D. M. Frenkel, J. Shi, and J. P. Lu, Phys. Rev. B **48**, 6728 (1993).

[43] K. M. Schep, P. J. Kelly, and G. E. W. Bauer, Phys. Rev. Lett. **74**, 586 (1995).

Chapter 2

Experiments

Abstract

In this chapter, we describe the experimental methods; preparation of samples and the structural analysis by using the x-ray diffraction and NMR.

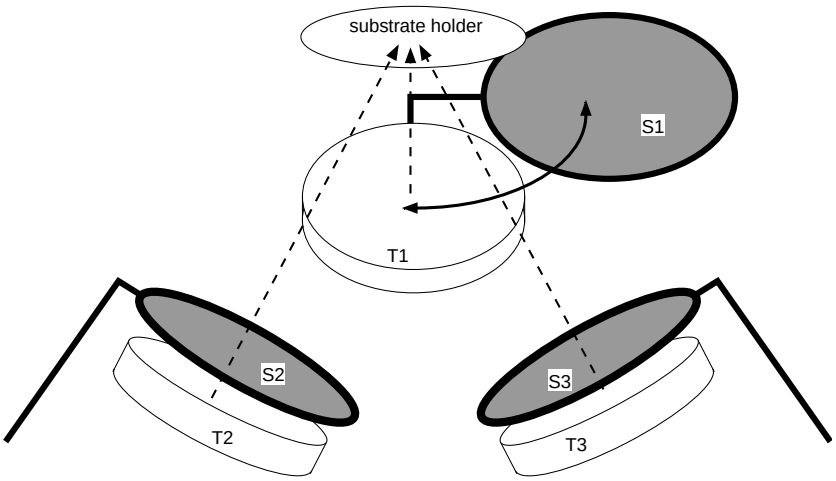

Fig. 2.1: Configuration of the targets, shutters and a substrate holder of the sputtering system. T1–T3 are targets independent of each other. S1–S3 are shutters.

2.1 Preparation of Co/Cu superlattices

The Co/Cu superlattices were deposited on insulating substrates (surface-oxidized Si or glass) in a magnetron sputtering system with a base pressure of 2×10^{-7} Torr. Figure 2.1 indicates the configuration of the sputtering system. The sputtering chamber is equipped with a substrate holder of 3 inch in diameter and three targets of 3 inch in diameter. All targets face to the substrate, and the distance between the substrate and each target is 150 mm. In order to control the amount of the deposition, each target has a mechanical shutter driven by a stepping motor which is controlled by a personal computer. This shutter system promises the resolution of the deposition time of 0.01 s.

Before deposition of the Co/Cu superlattice, the sputtering chamber was evacuated down to the base pressure. In order to shorten the time to reach

the base pressure, the sputtering chamber was baked at 100 °C for 2.5 h and then cooled to room temperature. Immediately before the deposition, substrate surface was cleaned by rf sputtering at 1 W/cm^2 for 4 min in an Ar pressure of 3×10^{-3} Torr. These processes are important to obtain Co/Cu superlattices with a lage MR ratio.

In most cases, we deposited a metal buffer layer between the substrate and the superlattice. After deposition of a buffer layer, 16–24 Co/Cu bilayers were grown at room temperature in an Ar pressure of 3×10^{-3} Torr at a deposition rate of 0.2–0.3 nm/s.

2.2 Characterization

2.2.1 Measurements of GMR and magnetization

The in-plane magnetoresistance (MR) was measured with a standard dc four-terminal geometry. The magnetization was also measured with a superconducting quantum interface device (SQUID) magnetometer.

2.2.2 X-ray diffraction

Using a conventional powder diffractometer, high and low angle x-ray diffraction (XRD) measurements were performed in a symmetrical reflection($\theta-2\theta$) geometry to characterize the crystallographic structure and the periodicity of superlattices. The divergence of the incident Co $K\alpha$ radiation ($\lambda = 0.179$ nm) was 1° for high angle XRD and 1/6° for low angle XRD. The scattered x-ray was detected with a proportional counter, after the Co $K\beta$ radiation was eliminated with a graphite monochromator. Since we used a bright x-ray source and the dynamic range of the counter was not so high, the total reflec-

tion was not recorded in the low angle XRD. Thus, we could not deduce the value of an x-ray reflectivity. Nevertheless, our samples for XRD were large enough compared with the beam size of an x-ray, so that the reproducibility of diffraction patterns measured at $2\theta \geq 2^\circ$ was very good in the absolute value. This fact confirms that the measured intensity in our experiment was proportional to the reflectivity of an x-ray.

2.2.3 ^{59}Co NMR

NMR experiments were carried out in zero field at liquid helium temperature. Figure 2.2 is the schematic drawing of the probe for the NMR measurement. In order to apply the rf field and to detect the spin echo signal, three coils of Cu wire of 1 mm in diameter are equipped at the bottom of the probe. Two of them are excitation and receiver coils of two turns and another is the tuning coil of three turns. The tuning coil is connected with the cylindrical condenser of Cu and bakelite, and it is tuned to get impedance matching between the exciting and receiver coils at each frequency. A sample was divided into rectangular pieces of 10×20 mm^2. Ten of them were stacked up and were fitted into coils. Thus, the rf field of 5–10 W was applied parallel to the film plane. Using a variable frequency spin-echo apparatus, the distribution of the hyperfine field of ^{59}Co was measured in a frequency range of 120–240 MHz.

The frequency spectrum was obtained by plotting the spin-echo amplitude at each frequency point by point. The pulse width and the separation of two rf pulses were kept at constant values of 1.2 μs and 15 μs, respectively. To obtain the number of atoms which resonate at a particular frequency

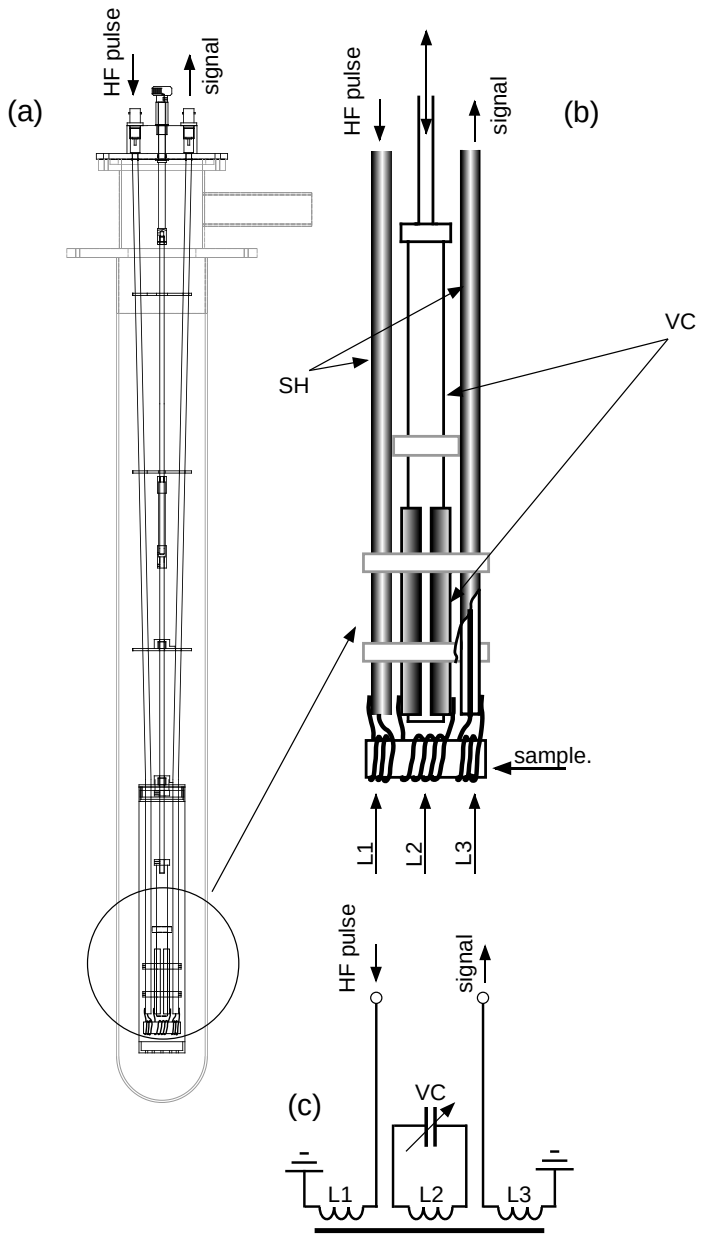

Fig. 2.2: Schematic drawing of the NMR probe (a), (b) and the equivalent circuit(c). SH; shielding pipe. VC; variable condenser. L1; exciting coil. L2; tuning coil. L3; receiver coil.

from the observed spin-echo amplitude, we collected the variation of the Boltzmann factor ($\propto \omega$) and the frequency dependence of the enhancement effect of nuclear signals ($\propto \omega$) [1]. Moreover, the frequency dependence of the detected voltage induced by the processing magnetization ($\propto \omega$) should be took into account. Thus, the spin-echo amplitude divided by ω^3 was taken to be proportional to the number of nuclei with a given resonance frequency. If the reference signal together with the spin echo signal was measured, the ω^2 dependence of the spin-echo amplitude was corrected.

References

[1] H. Yasuoka, in *Metallic Superlattices*, edited by T. Shinjo and T. Takada (Elsevier, Amsterdam, 1987), p. 159.

Chapter 3

Role of buffer layer in GMR

Abstract

The giant magnetoresistance (GMR) in the Co/Cu superlattices deposited on the various buffer layers has been investigated. A drastic changes in the MR ratio and the saturation field are found, depending on the thickness and the substance of the buffer layer. Changes in the crystallinity and interfacial roughness are responsible for the behavior of the GMR

3.1 Introduction

Much attention has been devoted to the giant magnetoresistance (GMR) and antiferromagnetic coupling of several multilayered systems, such as Fe/Cr [1], and Co/Cu [2, 3]. Among them, the largest MR ratio has been found in (111) textured magnetron sputtered Co/Cu systems. The key to achieve the large MR ratio was to insert an Fe buffer layer between Co/Cu and the substrate [3, 4].

In this chapter, we report the investigation on the effect of the buffer layer on the GMR property, crystallographic structures and interfacial roughness of magnetron sputtered Co/Cu superlattices.

3.2 Experiments

The Co/Cu superlattices were deposited on surface-oxidized Si substrates in a magnetron sputtering system with a base pressure of 2×10^{-7} Torr. After deposition of a buffer layer, 16–24 Co/Cu bilayers were grown at room temperature in an Ar pressure of 3×10^{-3} Torr at a deposition rate of $0.2 - 0.3$ nm/s.

In order to find the best combination of the layer thickness of Co and Cu, we prepared the Co/Cu superlattices on an Fe buffer layer of thickness 5.0 nm with various combination of thicknesses of Co (t_{Co}) and Cu (t_{Cu}). The number of bilayers of Co/Cu was chosen between 16 and 24 so that the total thickness was kept larger than 50 nm for all samples in order to reduce the effect of the spin-independent surface scattering. The in-plane magnetoresistance (MR) was measured at room temperature with a stan-

dard dc four-terminal geometry. The dimension of the samples used for this measurement was 3×50 mm^2, and the current used was 1 mA.

Using the optimized combination of t_{Co} and t_{Cu}, we investigated the effect of the substance and the thickness of the buffer layer. The substance of the buffer layer was selected among Cr, Fe, Co, NiFe, NiCo, Cu and Pt, and its thickness t_M (M =Cr, Fe, Co, NiFe, NiCo, Cu, Pt) was varied between 0 and 15.0 nm.

The crystallographic structure of the sample was characterized by x-ray diffraction, and the interfacial atomic structures were evaluated from the distribution of the hyperfine field associated with the Co atoms near interfaces. To obtain the hyperfine field, we have employed ^{59}Co NMR in zero field at 4.2 K using the variable frequency spin-echo apparatus.

3.3 Results and discussion

3.3.1 Relationship between GMR and thicknesses of Co and Cu

The MR properties as a function of t_{Cu} and t_{Co} are investigated for a series of the samples with an Fe buffer layer of thickness 5.0 nm. As indicated in Fig. 3.1, the MR ratio and the saturation field H_{s} oscillate as a function of the Cu layer thickness and show peaks at $t_{\mathrm{Cu}} = 0.9 \pm 0.05$ and $t_{\mathrm{Cu}} = 2.1 \pm 0.1$ nm. This is consistent with Refs. [2, 3]. The MR ratio and H_{s} at the first peak are 45% and 6 kOe, respectively, whereas they are 33% and 1.0 kOe at the second peak. Here, the MR ratio is defined as

$$\text{MR ratio} = (\rho_{\max} - \rho_{\mathrm{s}})/\rho_{\mathrm{s}} = \Delta\rho/\rho_{\mathrm{s}}, \tag{3.1}$$

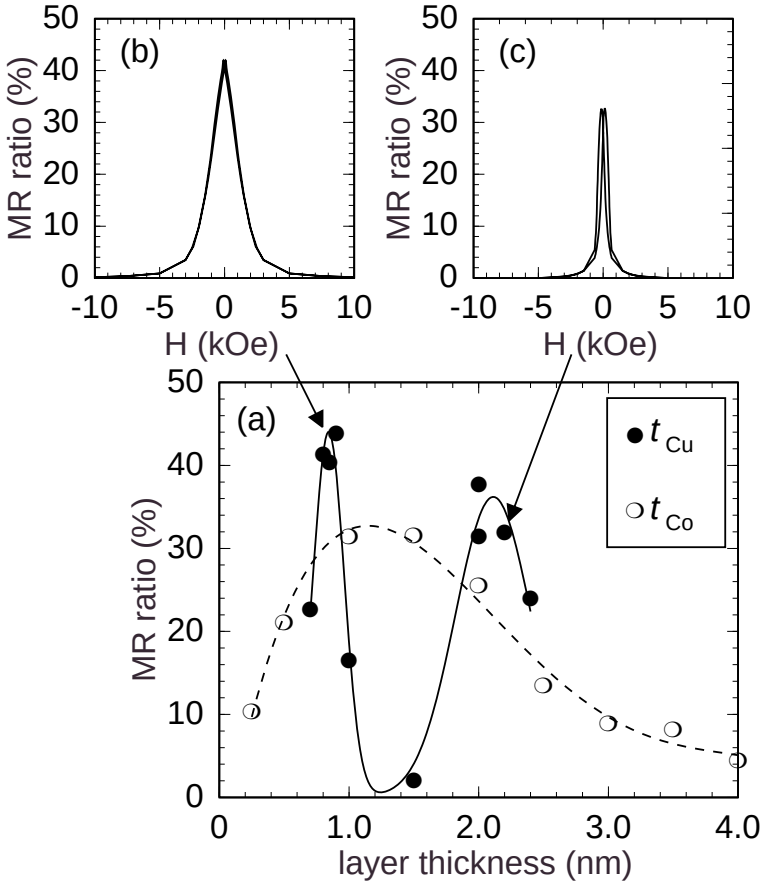

Fig. 3.1: (a) The layer thickness dependence of the GMR in Co/Cu superlattices deposited on an Fe buffer layer of 5.0 nm. Solid circles indicate the MR ratio for the samples of [Co(1.0 nm)/Cu(t_{Cu} nm)]$_n$, and open circles indicates the MR ratio for the samples of [Co(t_{Co} nm)/Cu(2.0 nm)]$_n$. (b) The MR curves for the samples of [Co(1.0 nm)/Cu(0.9 nm)]$_{24}$. (c) Those for [Co(1.0 nm)/Cu(2.2 nm)]$_{16}$ (c) are also indicated.

where ρ_{max} and ρ_s are the maximum and saturation resistivity, respectively. On the other hand, as a function of the Co layer thickness, the MR ratio shows a broad peak at around $t_{Co} = 1.0$ nm. Since the MR ratio at around $t_{Cu} = 0.9$ nm is very sensitive to the Cu layer thickness, it is difficult to prepare samples with almost identical GMR properties. Therefore, we focus our attention on the MR properties at the second peak of the oscillatory property of the GMR as a function of the Cu layer thickness. The structure of the Co/Cu superlattices discussed here is as follows: substrate/buffer layer/Cu(2.1 ± 0.1 nm)/[Co(1.0 ± 0.2 nm)/Cu(2.1 ± 0.1 nm)/]$_{16}$.

3.3.2 Critical thickness of Fe buffer layer

The variation of the saturation MR ratio and the x-ray diffraction intensity of the (111), (200) and (220) as a function of t_{Fe} is shown in Fig. 3.2. The x-ray diffraction intensity is normalized by the relative intensity of powder diffraction of fcc crystals. A drastic change in the MR ratio is found at about $t_{Fe} = 3.0$ nm. The saturation field H_s also changes at $t_{Fe} = 3.0$ nm. For $t_{Fe} < 3.0$, H_s is almost constant at 500 Oe, while it is also constant at 1 kOe for $t_{Fe} \geq 3.0$.

The preferred orientation for the sample is also transformed suddenly from (111) to (110) at the critical Fe buffer layer thickness of 3.0 nm as shown in Fig. 3.2(b). Obviously, there exists a strong correlation between the MR values and the textured structures. The size of grains with each texture estimated from FWHM of (111), (200) and (220) diffraction peak is about 20 nm, 8 nm and 10 nm respectively, and they are independent of t_{Fe}. Thus, the Fe buffer layer determines the number of grain nuclei with

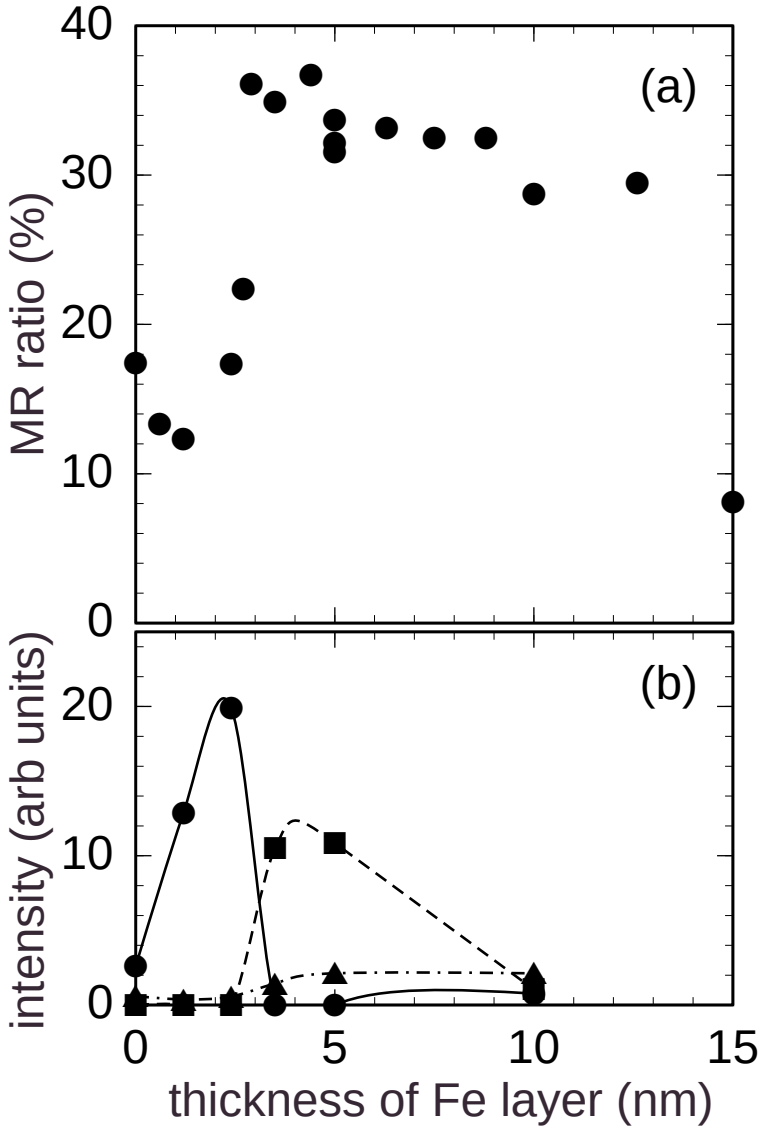

Fig. 3.2: Variation of (a) MR ratio at 300 K and (b) X-ray diffraction intensity of (111) (•), (200) (▲) and (220) (■) of Cu(2.0 nm)/[Co(1.0 nm)/Cu(2.0 nm)]$_{16}$ with t_{Fe}.

each texture at the initial stage of the growth. Once initiating the growth of the texture, grains with each texture grow up to certain size depending on its crystallographic orientation. This difference in the crystallinity should be reflected to the interfacial roughness.

Figs. 3.3(a) and (b) are typical examples of the NMR spectra of $t_{\mathrm{Fe}} < 3.0$ nm and $t_{\mathrm{Fe}} \geq 3.0$ nm, respectively. We correct the frequency dependence of the spin-echo signal to obtain the number of atoms which resonate at a particular frequency [5], and it is normalized by the main peak intensity at around 213 MHz, which is attributed to the signal from the fcc Co atoms with 12 nearest-neighbor Co atoms. There exists a wide distribution of the hyperfine field in the lower frequency region of the main peak down to 120 MHz. Other samples of $t_{\mathrm{Fe}} < 3.0$ nm and $t_{\mathrm{Fe}} \geq 3.0$ nm showed a similar spectrum as Figs. 3.3(a) and (b), respectively. It is well known that the tail in the lower frequency region of the main peak is attributed to the Co atoms near interfaces [6–9]. Therefore, the samples of $t_{\mathrm{Fe}} < 3.0$ nm and $t_{\mathrm{Fe}} \geq 3.0$ nm may have not only different crystallinity but also a different interfacial structure.

Following Gronckel *et al.* [7], we deconvoluted the spectrum into Gaussians with constant width, and roughly estimated the interfacial structure taking into account the chemical composition profile (CCP) and the atomic short range order (ASRO) parameter [10]. Figure 3.4 is a schematic view of the typical interfacial structure which reproduce the observed NMR spectra. For the samples of $t_{\mathrm{Fe}} < 3.0$ nm, the atomic mixing occurs in the 4 atomic layers at interface. However, the amount of the mixed atoms considerably small (less than 10%). Furthermore, ASRO parameters indicate the strong

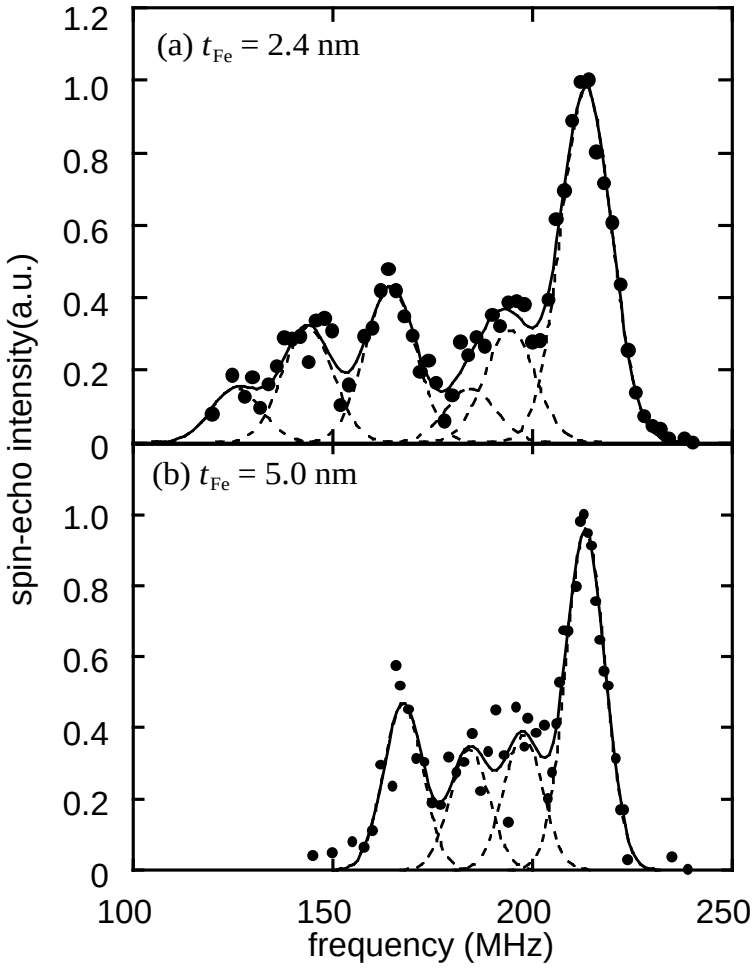

Fig. 3.3: Typical examples of ^{59}Co NMR spectra. The thickness of the Fe buffer layer for the samples are (a) $t_{\mathrm{Fe}} < 3.0$ nm and (b) $t_{\mathrm{Fe}} \geq 3.0$ nm. The solid line represents the results of a fit with Gaussians.

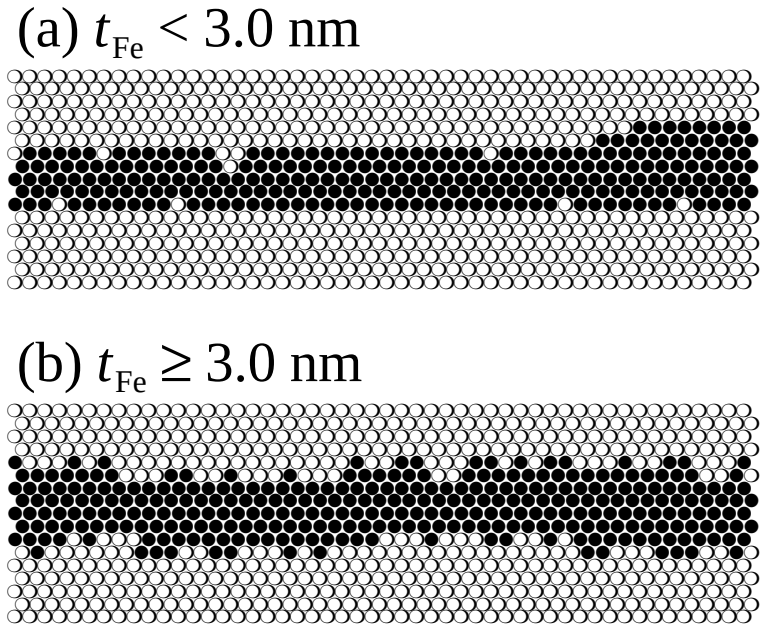

Fig. 3.4: Schematic views of the interfacial structure of Co/Cu superlattices of (a) $t_{Fe} < 3.0$ nm and (b) $t_{Fe} \geq 3.0$ nm. Solid (open) circles indicate the Co(Cu) atoms.

tendency of clustering of Co atoms at the interface. Thus, there exist a large steps or islands as shown in Fig. 3.4(a). For the samples of $t_{Fe} \geq 3.0$ nm, the interlayer mixing is found in only two atomic layers at the interface. However, the amount of the mixed atoms is larger (30–40%) than that of the samples of $t_{Fe} < 3.0$ nm. In addition, the Co atoms at the interface are distributed randomly. These CCP and ASRO parameters resulted in considerable rough interfaces as shown in Fig. 3.4(b). At least, we can conclude that the fraction of these grains with rough interface is larger for the samples of $t_{Fe} \geq 3.0$ nm than that for the samples of $t_{Fe} < 3.0$ nm.

Table 3.1: MR properties of Co/Cu superlattices deposited on various buffer layers. The structure of the superlattices is substrate/buffer layer/Cu(2.1 nm)/[Co(1.0 nm)/Cu(2.1 nm)]$_{16}$.

buffer layer			MR ratio (%)	H_s (Oe)	preferred orientation
material		thickness (nm)			
bcc	Fe	1.2	10.8	$\sim$ 500	(111)
	Fe	5.0	33.0	$\sim$1000	(110)
	Cr	1.5	5.1	$\sim$ 500	(111)
	Cr	5.0	19.3	$\sim$1000	(110)
fcc	Cu	5.0	4.3	$\sim$ 500	(111)
	Pt	5.0	10.3	$\sim$ 500	(111)
	Co	5.0	17.3	$\sim$ 500	(111)
	NiCo	5.0	17.4	$\sim$ 500	(111)
	NiFe	5.0	24.5	$\sim$ 500	(111)

3.3.3 Dependence of GMR on substance of buffer layer

Typical MR properties and the preferred orientation for the samples deposited on the various buffer layers are indicated in Table 3.1. The critical behaviors in GMR and crystallographic structure similar to the samples deposited on the Fe buffer layer were also found for the samples deposited on Cr buffer layers at about $t_{Cr} = 3.0$ nm. Contrary to this, the GMR properties and the crystallographic structure are almost independent of the thickness of the buffer layer of Cu, Pt, Co, NiCo and NiFe, when $t_M \geq 1.0$ nm.

For all samples with (111) preferred orientation, the value of H_s is about 500 Oe, whereas for the samples with (110) preferred orientation it is about 1.0 kOe. The value of H_s is closely related to the preferred orientation and independent of the substance of the buffer layer. For the samples with (111) orientation, however, the magnitude of the MR ratio varies from 4% to 25% depending strongly on the substance of the buffer layer. No significant corre-

lation were found between the MR ratio and the (111) diffraction intensity. Moreover, we observed the differences in the low angle x-ray diffraction due to the artificial period. As indicated in 3.3.2, interfacial atomic structures should be also different for these samples. The differences in both the crystallinity and the interfacial roughness may be responsible for the dependence of the GMR on the substance of the buffer layer.

The relationship between the GMR and the structures is quite complicated. Therefore, it is important to control the crystallographic and the interfacial structures in order to investigate the mechanism of the spin-dependent scattering on magnetic superlattices. In the following chapters, we will discuss the relationship between the GMR and the interfacial roughness for the superlattices with well-controlled interfaces.

3.4 Conclusion

We have investigated the role of the buffer layer in the GMR and the structure of Co/Cu superlattices. The GMR properties and the textured structure change depending on the thickness and the substance of the buffer layer. The value of H_s is closely related to the preferred orientation and is smaller for the samples with (111) preferred orientation than those with (110). However, the difference in the MR ratio cannot be attributed only to the differences in the preferred orientation, since the difference in the textured structure affects the interfacial roughness.

Unfortunately, we cannot conclude from the results in this chapter which is more responsible for the critical behavior of MR ratio, the interfacial roughness or crystallinity. In the following chapters, we will discuss the role of the

interfaces with the special emphasis on the interfacial atomic structures.

References

[1] M. N. Baibich, J. M. Broto, A. Fert, F. Nguyen Van Dau, F. Petroff, P. Etienne, G. Creuzet, A. Friederich, and J. Chazelas, Phys. Rev. Lett. **61**, 2472 (1988).

[2] D. H. Mosca, F. Petroff, A. Fert, P. A. Schroeder, W. P. Pratt Jr., and R. Laloee, J. Magn. Magn. Mater. **94**, L1 (1991).

[3] S. S. P. Parkin, R. Bhadra, and K. P. Roche, Phys. Rev. Lett. **66**, 2152 (1991).

[4] M. E. Tomlinson, R. J. Pollard, D. J. Lord, and P. J. Grundy, J. Magn. Magn. Mater. **111**, 79 (1992).

[5] H. Yasuoka, in *Metallic Superlattices*, edited by T. Shinjo and T. Takada (Elsevier, Amsterdam, 1987), p. 159.

[6] K. L. Dang, P. Veillet, H. He, F. J. Lamelas, C. H. Lee, and R. Clarke, Phys. Rev. B **41**, 12902 (1990).

[7] H. A. M. de Gronckel, K. Kopinga, W. J. M. de Jonge, P. Panissod, J. P. Schillé, and F. J. A. den Broeder, Phys. Rev. B **44**, 9100 (1991).

[8] Y. Suzuki, T. Katayama, and H. Yasuoka, J. Magn. Magn. Mater. **104**–**107**, 1843 (1992).

[9] C. Mény, P. Panissod, and R. Loloee, Phys. Rev. B **45**, 12269 (1992).

[10] N. Hamada, K. Terakura, K. Takanashi, and H. Yasuoka, J. Phys. F **15**, 835 (1985).

Chapter 4

Interfacial structure of Co/Cu superlattices

Abstract

An attempt has been made to clarify the effect of interfacial mixing on the x-ray diffraction (XRD) and ^{59}Co NMR of Co/Cu superlattices. Systematic and quantitative modification of interfaces has been achieved by codeposition of Co and Cu at interfaces. We show that high and low angle XRD patterns are not affected by the existence of compositionally mixed regions thinner than 0.3 nm, and that significant change in the distribution of hyperfine field of ^{59}Co is found. The interfacial modification by codeposition is a powerful method to investigate the interfacial effects on the properties of superlattices, since only the interfacial structures are modified, while the other structures remain unchanged.

4.1 Introduction

Up to now, many attempts have been devoted to reveal the relation between the giant magnetoresistance (GMR) and interfacial states for Fe/Cr [1, 2], Co/Cu [3, 4] and NiFe/Cu [5, 6]. In many cases, the interfacial structure is investigated by x-ray diffraction (XRD) because of its easy manipulation. Basically, XRD is a method to analyze a long range order of samples, and it gives ambiguous information for the lateral scale of interfacial structure. It is difficult to determine the lateral length of roughness, if it causes a significant change in XRD pattern. Fortunately, we can use the ^{59}Co NMR for the structural analysis of Co/Cu superlattices. Contrary to XRD, NMR is very sensitive to the atomic short range order (ASRO), since the hyperfine interaction has a substantial contribution from the moment in the environment of nearest-neighbor atoms. Several studies on NMR for Co/Cu superlattices have been already reported [4, 7–12]. However, it has not been clarified how the structure observed by NMR appears in XRD pattern or vice versa.

As well as the structural analysis, it is important to modify the interfacial structure in order to investigate the relationship between the properties of superlattices and interfacial states. In previous studies, the interfacial modification has been performed by annealing samples [1, 3, 6] or changing the deposition conditions [2, 4]. However, the annealing of superlattices causes not only the interdiffusion at interfaces but also the change in crystallinity due to self-diffusion in the layer. Moreover, diffusion at grain boundaries or stress-induced diffusion can often be more rapid than that in bulk [13–16], so that we cannot preclude the possibility that the diffused atoms do not localize near interfaces. On the other hand, changing the deposition condition,

especially for sputtered superlattices, causes the changes in morphology and preferred orientation [17–20].

From the standpoint of this, we tried to modify the interfaces of Co/Cu superlattices directly by codeposition [21]. As described in Chapters 5 and 6, we were successful to prepare samples for which the GMR is very different from each other. In the present chapter, we perform XRD and NMR measurements for the samples with the modified interfaces by codeposition. We show here that there exists an interfacial structure which causes a significant change in NMR spectra but not detected by XRD. Furthermore, we propose that the interfacial modification by codeposition is a powerful method to change only the interfacial structure and to investigate the effects of interfaces on the properties.

4.2 Experiment

The Co/Cu superlattices were deposited on surface-oxidized Si substrates in a magnetron sputtering system with a base pressure of 2×10^{-7} Torr. After deposition of an Fe buffer layer with a thickness of 5.0 nm, 16 Co/Cu bilayers were grown at room temperature in an Ar pressure of 3×10^{-3} Torr at a deposition rate of 0.2–0.3 nm/s. Interfaces between Co and Cu layers were modified by codeposition, which was performed with a computer controlled shutter system. The nominal thickness of the codeposited region t_{mix} was estimated from the deposition rate, and the chemical composition of Co and Cu in the mixed region was to be about 40 and 60 at.%, respectively. The amount of Co and Cu in each bilayer was kept constant at 1.0 and 2.2 nm for pure Co and Cu. The nominal structure of sam-

ples was as follows: substrate/Fe(5.0)/Cu(2.2−t_{mix}/2)/CoCu(t_{mix})/[Co(1.0−t_{mix})/CoCu(t_{mix})/Cu(2.2−t_{mix})/CoCu(t_{mix})]$_{15}$/Co(1.0−t_{mix})/Cu(2.2−t_{mix}/2), where the values in the parentheses are the thickness of layers in unit of nm. As indicated in Fig. 3.1, this structure corresponds to the second peak of oscillatory properties of GMR and the antiferromagnetic coupling between adjacent Co layers. The value of magnetoresistance (MR) ratio of the sample of $t_{\mathrm{mix}} = 0$ nm was 35% at 300 K [21]. The details of transport properties of these samples is discussed in Chapters 5 and 6 [22].

Using a conventional powder diffractometer, high and low angle XRD measurements were performed in a symmetrical reflection($\theta - 2\theta$) geometry to characterize the crystallographic structure and the periodicity of superlattices. We discuss the interfacial flatness and sharpness of Co/Cu superlattices by comparing the XRD patterns measured at $2^\circ \leq 2\theta \leq 8^\circ$ with the theoretical calculations as described later.

NMR experiments were carried out in zero field at liquid helium temperature. In order to calibrate the frequency dependence of the measurement system, we measured the reference signal together with the spin echo signal. Moreover, we correct the ω^2 dependence of the spin-echo signal to obtain the number of atoms which resonate at a particular frequency [23].

4.3 Results and discussion

4.3.1 XRD

Figure 4.1 shows a typical high angle XRD pattern for the samples. Three peaks for fcc Co/Cu are observed. Comparing with the relative intensity of powder diffraction of fcc crystals, our samples show a strong tendency to

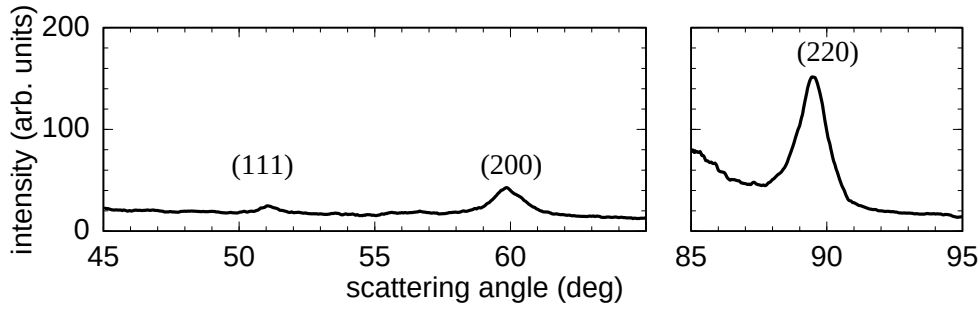

Fig. 4.1: High angle x-ray diffraction pattern for the sample of $t_{\mathrm{mix}} =$ 0 nm. Samples of $t_{\mathrm{mix}} \neq 0$ nm show almost the same diffraction pattern.

(110) textured structure. Contrary to most of the sputtered Co/Cu superlattices reported by other workers [24, 25], (110) preferred orientation of our samples is characteristic, and is likely to be closely related to the structure of the Fe buffer layer [12]. The diffraction patters of samples with different t_{mix} cannot be distinguished from each other. Thus, the crystallographic structures of present samples are independent of t_{mix}, while those of the samples prepared on glass substrates depend on t_{mix} as we report in Chapter 5 [21]. Unfortunately, we cannot deduce the information on the interfacial structure from the high angle XRD, since the diffraction intensities are not so strong.

Low angle XRD patterns are also independent of t_{mix} as indicated in Fig. 4.2. For all the samples different in t_{mix}, Bragg peaks due to the artificial period and Kiessig fringes are clearly visible. Since the superlattice period is kept constant, these peaks appear at almost the same position. It is remarkable that no significant differences in the amplitude of peaks can be observed between samples. One might occasionally refer to these diffraction patterns as the evidence of the flat and sharp interfaces. However, there must be considerable differences in interfacial structure.

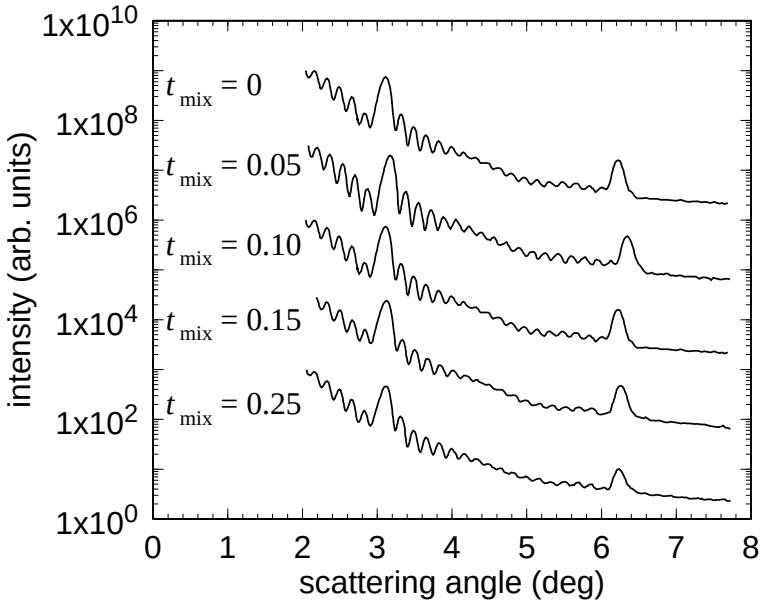

Fig. 4.2: Measured low angle x-ray diffraction patterns. The large peaks at $2\theta = 3.1^\circ$ and 6.2° correspond to the Bragg diffraction for the superlattice period. Each pattern is shifted for better understanding.

For semiquantitative interpretation of the interfacial structure, we performed the low angle XRD simulation. To take the low angle corrections into account, we use a standard optical model by applying a recursive Fresnel formalism described by Underwood and Barbee [26]. The optical constants were determined assuming the same lattice constant for Co and Cu evaluated from the high angle XRD. At first, we discuss the effect of the thickness fluctuation of each layer. Following Fullerton *et al.* [27], we take the effect of the thickness fluctuation into account by Monte Calro method. The mean layer thicknesses of Co and Cu are set at 1.0 and 2.2 nm, respectively, and the thickness of each layer is selected randomly as its distribution follows the Gaussian distribution function around the mean thickness. Since the

calculated reflectivity brings the phase information, the averaged intensity depends on the averaging procedure. The averaged intensity, excluding the phase information, is given as [27]

$$I = \frac{1}{N_{\mathrm{av}}} \sum_{n=1}^{N_{\mathrm{av}}} |R_n|^2, \tag{4.1}$$

where R_n is the superlattice reflectivity for a superlattices with a particular random sequence of thickness, while the reflectivity including the phase information is written as

$$I = \frac{1}{N_{\mathrm{av}}} \left| \sum_{n=1}^{N_{\mathrm{av}}} R_n \right|^2. \tag{4.2}$$

For a more realistic calculation, we must take account of both effects simultaneously. In the present case, however, we compare the experiments only with the calculation of Eqs. (4.1) and (4.2) separately.

Figure 4.3(a) shows the calculated XRD patterns excluding the phase information for the different thickness fluctuations. In this thesis, the magnitude of the thickness fluctuation is expressed by σ_f, the standard deviation of the Gaussian distribution of the thickness. With increasing σ_f, the intensity of Bragg peaks and the amplitude of Kiessig fringes decrease rapidly. On the other hand, the decrease with increasing 2θ of the background of the calculated intensity is almost independent of σ_f. If we average the reflectivity of the x-ray including the phase information, the dependence of the calculated intensity on σ_f is varied as shown in Fig. 4.3(b). Contrary to the case excluding the phase information, the background of the calculated intensity decreases more rapidly with 2θ for the large value of σ_f.

Obviously, the low angle XRD is very sensitive to the thickness fluctuation. Comparing the calculated XRD patterns with the measured ones, the

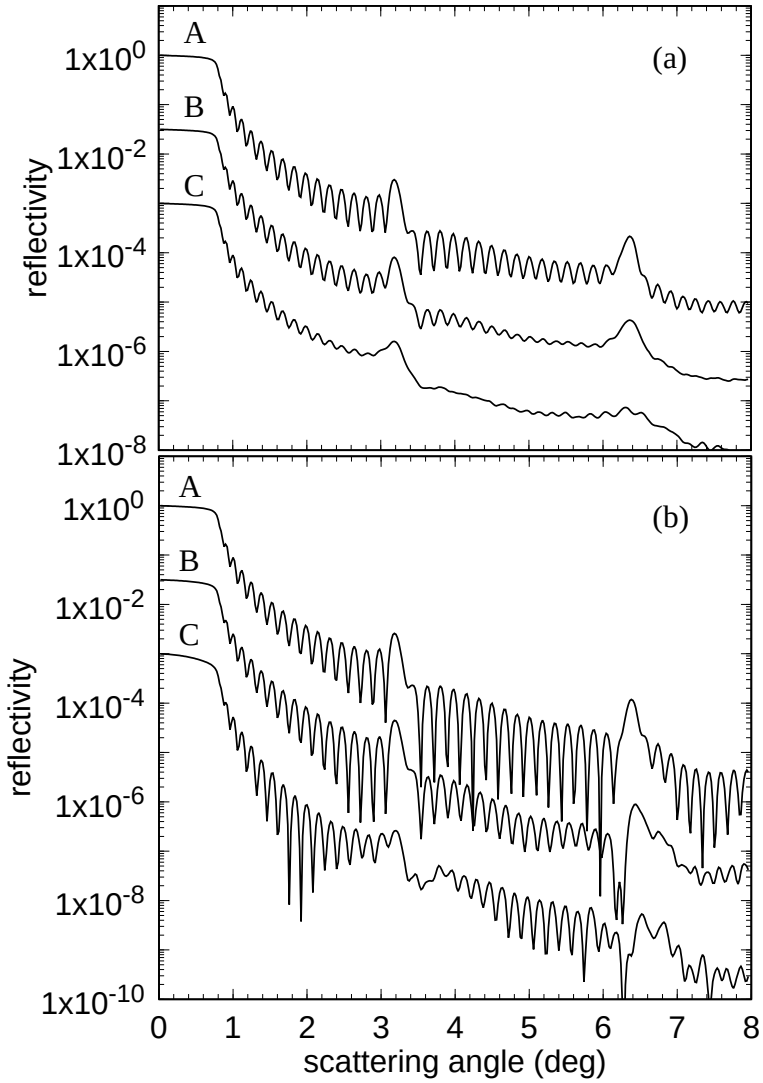

Fig. 4.3: Calculated low angle x-ray diffraction patterns for models with thickness fluctuation of $\sigma_f = 0.05$ (line A), 0.10 (line B) and 0.20 nm (line C). The x-ray reflectivity is averaged (a) excluding the phase information and (b) including the phase information.

value of σ_f for our samples should be less than 0.1 nm and is independent of t_{mix}. If the codeposited region of $t_{\mathrm{mix}} \leq 0.25$ nm is regarded as the thickness fluctuation for the x-ray, the differences in the XRD patterns between our samples must be observed. This fact suggests that the lateral length of the thickness fluctuation is much shorter than the coherent length of the x-ray.

When the lateral length of the thickness fluctuation becomes much shorter than the coherent length of the x-ray, the transition of optical constants from the Co to the Cu layer will take place over a finite distance. We can take this effect into account by a sequence of thin layers with average optical constants approximating the continuous change in the optical constants in the transition region [26, 27]. Because of the low contrast in the scattering power for the Co-Cu system, the calculated XRD patterns remain unchanged, if we assume the transition region of the thickness less than 0.25 nm. Consequently, such a transition region will exist at interfaces of our samples. However, we cannot deduce the lateral length of roughness and the thickness of the transition region from the XRD data.

4.3.2 NMR

In contrast to the XRD, the NMR is sensitive to the ASRO. Figure 4.4 shows the frequency spectra of spin-echo intensity of ^{59}Co in the sample of various t_{mix}. The main peak observed around 210 MHz is attributed to the signal from the fcc Co atoms with 12 nearest-neighbor Co atoms, while the resonance frequency is slightly lower than that for bulk Co of 217 MHz. Since no significant signal was observed on the higher frequency side of the main peak, the amount of the hcp Co is negligible. There exists a wide distribution

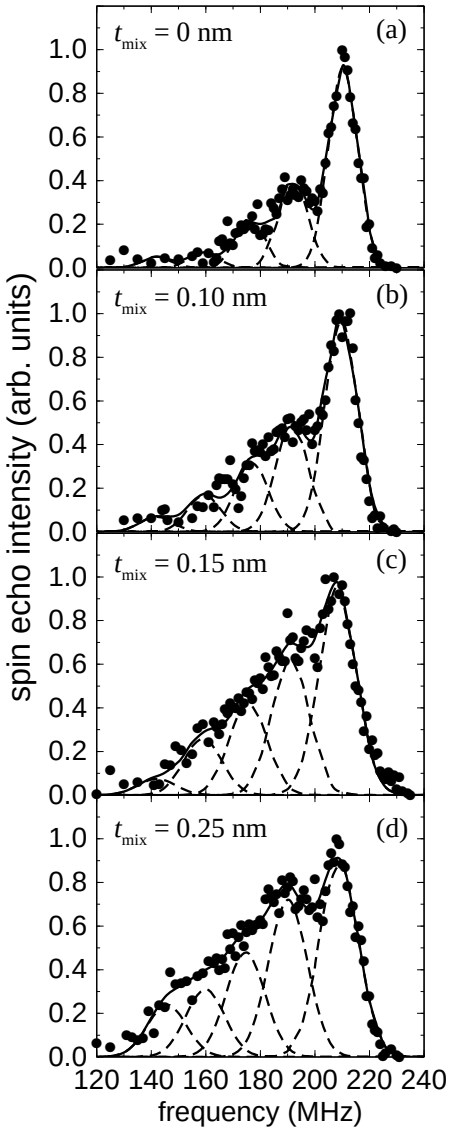

Fig. 4.4: Frequency spectra of spin-echo intensity of ^{59}Co. The measured data (•) are fitted with five Gaussians (dashed lines). The solid lines indicate the summation of five Gaussians.

of the hyperfine field in the lower frequency region of the main peak down to 120 MHz. The tail at the frequency lower than that of main peak is due to the Co atoms near interfaces. Please note that the intensity of tail increases with t_{mix}. This indicates that the amount of the mixing of Co and Cu atoms increases with t_{mix}.

For the more quantitative interpretation of the NMR spectra, it is necessary to extract the number of Co atoms with one or more Cu atoms in their nearest-neighbor shell. The experiment in dilute CoCu alloy indicates that the resonance frequency shifts with respect to that of bulk by 18 MHz per Cu atom in nearest-neighbor shell of Co atoms [28]. The similar effect has been observed for Co/Cu superlattices, although the values of the spacing between the resonance peaks are not identical with the alloy case due to the strain [4, 7–12]. Therefore, we analyze the frequency spectra by fitting with Gaussians. The measured spectra are well fitted with five Gaussians of constant width as indicated by solid lines in Fig. 4.4, where we treat one width of Gaussians, five peak positions and five peak intensities as free parameters. The fits are insensitive to the initial parameters and always converge to the same lines indicated in Fig. 4.4. The errors for the peak positions are less than 1 MHz, and those for intensities are less than 5 %. The spacing between the peak positions of each Gaussian is 15±3 MHz. This value is almost independent of the samples and is the same with the value reported for (110) oriented Co/Cu superlattices [4]. The fits with less than four Gaussians are poor, while those with more than six Gaussians result in the significant increase in the scatter of the spacing between peaks depending on the samples. Therefore, we attribute the five Gaussians to the resonance of the Co atoms

with 12–8 Co atoms in their nearest-neighbor shell.

Assuming the fcc (110) stacking for the superlattices, the probability of finding the Co atoms, which are surrounded by N nearest-neighbor Co atoms, in the ith atomic layer is given as [29],

$$P_i(N) = \sum{}' \Phi(n_{i-2}; 1, p_{i-2})\Phi(n_{i-1}; 4, p_{i-1}) \times\Phi(n_i; 2, p_i)\Phi(n_{i+1}; 4, p_{i+1})\Phi(n_{i+2}; 1, p_{i+2}), \tag{4.3}$$

with the binomial distribution function defined by

$$\Phi(n; z, p) = \frac{z!}{n!(z-n)!}p^n(1-p)^{z-n}, \tag{4.4}$$

where n_j is the number of nearest-neighbor Co atoms in the jth atomic layer, and the summation is taken for all sets satisfying $N = \sum_{j=i-2}^{i+2} n_j$. The value of p_i is the probability of finding a Co atom at a particular nearest-neighbor site of Co atom, and is given by

$$p_i = x_i + \alpha_i(1 - x_i), \tag{4.5}$$

where x_i is the concentration of Co atoms in the ith atomic layer, and α_i is the ASRO parameter. In the case of $\alpha_i = 0$, Co and Cu atoms distribute randomly, while $\alpha_i < 0$ ($\alpha_i > 0$) corresponds to the ordering (segregation) of the Co and Cu atoms. Using Eqs. (4.3)–(4.5), we can calculate the number of Co atoms in one superlattice period with N nearest-neighbor Co atoms as

$$P(N) = \sum_i x_i P_i(N), \tag{4.6}$$

in unit of monolayers (ML), where the summation is taken over one superlattice period.

The frequency spectrum for appropriate chemical composition profile (CCP) and the ASRO parameters are calculated assuming that the spin-echo intensity is proportional to $P(N)$ and using the results of Gaussian fitting for the value of the frequency and the width of ^{59}Co resonance. We deduced the optimum CCP's and ASRO parameters to reproduce the measured frequency spectra by the Davidon-Fletcher-Powell (DFP) method [30]. In the present case, 8 ML of Co exist in a (110) stacked Co layer with a thickness of 1.0 nm. Thus, we started from the ideal structure consisting of 8 ML of Co, and x_i and α_i of six atomic layers near interfaces were treated as parameters.

Resulting CCP's are shown in Fig. 4.5. The ASRO parameters are almost zero in all atomic layers for all samples. The calculated frequency spectra corresponding to CCP's in Fig. 4.5 coincide with the initial Gaussian fittings as indicated by solid lines in Fig. 4.4. The shape of the spectrum depends drastically upon CCP (parameters x_i). For example, there are significant change in the shape of the spectra for the samples of $t_{\rm mix} = 0,\ 0.10$ and 0.15 nm [Fig. 4.4(a)–(c)], while the differences in CCP's for these samples are not so large [Fig. 4.5(a)–(c)]. This indicates that the NMR has the power to detect the small differences in the CCP. Because of this high sensitivity of NMR to local composition, CCP's were determined within the errors indicated by bars in Fig. 4.5, in spite of the many fitting parameters. For the sample of $t_{\rm mix} = 0$ nm, the intermixing extends over 2 atomic layers near interface. The concentrations of Co in the first and second atomic layers from the interface are 84 and 97 %, respectively. With increasing $t_{\rm mix}$, the amount of the intermixing increases. On the other hand, the shape of the spectrum is not so

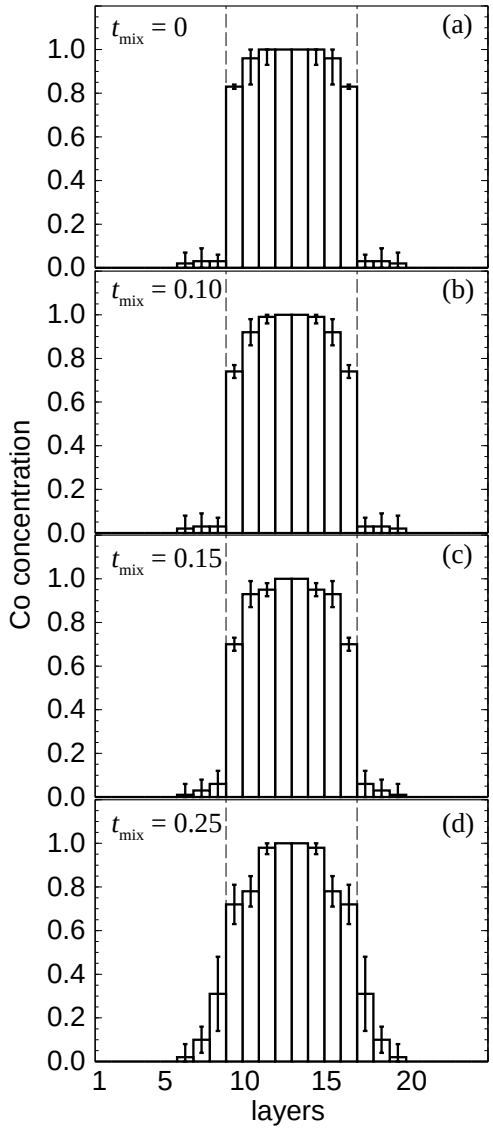

Fig. 4.5: Estimated chemical composition profile in one superlattice period. The histogram shows the estimated Co concentration x_i. The dashed lines indicate the boundaries of the Co layer of 8 ML with ideal structure. The bars indicate the statistical error.

sensitive to the ASRO parameters (α_i) in the present case. However, their values of almost zero are reliable enough to preclude the strong ordering or segregation of the Co and Cu atoms. Therefore, atoms of Co and Cu are distributed randomly in the mixed regions.

The results for XRD and NMR are consistent with each other. Since Co and Cu are randomly mixing at interfaces, the optical constants for x-ray will change from the Co to Cu layer over a finite distance. On the other hand, the thickness of the mixing region is uniform in the sample as expected from the XRD measurements. Therefore, no significant change in the XRD pattern for the samples of different t_{mix} is observed. These facts confirm that our samples with different t_{mix} are only different in the distribution of Co atoms near interfaces, while the superlattice period, the thickness fluctuation and crystallinity remain unchanged. Consequently, we can control the atomic roughness of the interfaces in the Co/Cu superlattices by codeposition.

4.4 Conclusion

We have investigated the interfacial structure of Co/Cu superlattices with artificially mixed interfaces by XRD and ^{59}Co NMR. For the samples of different t_{mix}, no significant change was observed in the XRD patterns. NMR measurements clarified that Co and Cu atoms distributed randomly in the interfacial mixed region, and that the CCP of Co was systematically changed depending on t_{mix}. This indicates clearly that the atomically mixed region in Co/Cu superlattices cannot be detected by XRD. On the other hand, dynamical simulation for low angle XRD revealed that the XRD was very sensitive to the thickness fluctuation. Therefore, XRD and NMR are compensative

with each other.

Using the well-controlled codeposition technique, we can modify only the CCP in a very thin region near interfaces. The thickness fluctuation, crystallinity and morphology of superlattices are unchanged. Contrary to the thermal treatment or the sample preparations under various deposition conditions, the interfacial modification by codeposition is a powerful method to investigate the interfacial phenomena such as GMR. The dependence of GMR on t_{mix} at room temperature will be reported in Chapter 5 [21], and its temperature dependence will be reported in Chapter 6 [22].

References

[1] F. Petroff, A. Barthélémy, A. Hamzić, A. Fert, P. Etienne, S. Lequien, and G. Creuzet, J. Magn. Magn. Mater. **93**, 95 (1991).

[2] E. E. Fullerton, D. M. Kelly, J. Guimpel, I. K. Schuller, and Y. Bruynseraede, Phys. Rev. Lett. **68**, 859 (1992).

[3] M. J. Hall, B. J. Hickey, M. A. Howson, C. Hammond, M. J. Walker, D. G. Wright, D. Greig, and N. Wiser, J. Phys. Condens. Mater. **4**, L495 (1992).

[4] Y. Saito, K. Inomata, A. Goto, and H. Yasuoka, J. Phys. Soc. Jpn. **62**, 1450 (1993).

[5] T. C. Huang, J.-P. Nozieres, V. S. Speriosu, H. Lefakis, and B. A. Gurney, Appl. Phys. Lett. **60**, 1573 (1992).

[6] V. S. Speriosu, J. P. Nozieres, B. A. Gurney, B. Dieny, T. C. Huang, and H. Lefakis, Phys. Rev. B **47**, 11579 (1993).

[7] K. L. Dang, P. Veillet, H. He, F. J. Lamelas, C. H. Lee, and R. Clarke, Phys. Rev. B **41**, 12902 (1990).

[8] H. A. M. de Gronckel, K. Kopinga, W. J. M. de Jonge, P. Panissod, J. P. Schillé, and F. J. A. den Broeder, Phys. Rev. B **44**, 9100 (1991).

[9] C. Mény, P. Panissod, and R. Loloee, Phys. Rev. B **45**, 12269 (1992).

[10] Y. Suzuki, T. Katayama, and H. Yasuoka, J. Magn. Magn. Mater. **104**–**107**, 1843 (1992).

[11] J. S. Lord, H. Kubo, P. C. Riedi, and H. J. Walker, J. Appl. Phys. **73**, 6381 (1993).

[12] M. Suzuki, Y. Taga, A. Goto, and H. Yasuoka, J. Magn. Magn. Mater. **126**, 495 (1993).

[13] A. K. Schmid, D. Atlan, H. Itoh, B. Heinrich, T. Ichinokawa, and J. Kirschner, Phys. Rev. B **48**, 2855 (1993).

[14] G. R. Harp, S. S. P. Parkin, R. F. C. Farrow, R. F. Marks, M. F. Toney, Q. H. Lam, T. A. Rabedeau, and R. J. Savoy, Phys. Rev. B **47**, 8721 (1993).

[15] M. T. Kief and W. F. Egelhoff Jr., Phys. Rev. B **47**, 10785 (1993).

[16] R. M. Tromp, A. W. Denier van der Gon, and M. C. Reuter, Phys. Rev. Lett. **68**, 2313 (1992).

[17] J. A. Thornton, Annu. Rev. Mater. Sci. **7**, 239 (1977).

[18] Y. Saito, S. Hashimoto, and K. Inomata, Appl. Phys. Lett. **60**, 2436 (1992).

[19] R. J. Highmore, W. C. Shih, R. E. Somekh, and J. E. Evetts, J. Magn. Magn. Mater. **116**, 249 (1992).

[20] K. Takanashi, Y. Obi, Y. Mitani, and H. Fujimori, J. Phys. Soc. Jpn. **61**, 1169 (1992).

[21] M. Suzuki and Y. Taga, J. Appl. Phys. **74**, 4660 (1993).

[22] M. Suzuki and Y. Taga, Phys. Rev. B **52**, 361 (1995).

[23] H. Yasuoka, in *Metallic Superlattices*, edited by T. Shinjo and T. Takada (Elsevier, Amsterdam, 1987), p. 159.

[24] S. S. P. Parkin, R. Bhadra, and K. P. Roche, Phys. Rev. Lett. **66**, 2152 (1991).

[25] D. H. Mosca, F. Petroff, A. Fert, P. A. Schroeder, W. P. Pratt Jr., and R. Laloee, J. Magn. Magn. Mater. **94**, L1 (1991).

[26] J. H. Underwood and T. W. Barbee Jr., Appl. Opt. **20**, 3027 (1981).

[27] E. E. Fullerton, I. K. Schuller, H. Vanderstraeten, and Y. Bruynseraede, Phys. Rev. B **45**, 9292 (1992).

[28] S. Nasu, H. Yasuoka, Y. Nakamura, and Y. Murakami, Acta Metall. **22**, 1057 (1974).

[29] N. Hamada, K. Terakura, K. Takanashi, and H. Yasuoka, J. Phys. F **15**, 835 (1985).

[30] R. Fletcher and M. J. Powell, The Computer Journal **6**, 163 (1963).

Chapter 5

GMR in Co/Cu superlattices with mixed interfaces I

~ Effect of interfacial roughness on GMR and AF coupling

Abstract

Magnetoresistance, antiferromagnetic coupling and crystallographic orientation of Co/Cu superlattices with intentionally mixed interfaces have been studied as a function of the thickness of the mixed region. The antiferromagnetic coupling is weakened, and spin-independent scattering of free electrons is enhanced with increasing thickness of the mixed region, although the morphology and superlattice period remain unchanged. Saturation magnetoresistance is reduced from 27 % to 4 % as the result of formation of 0.15 nm mixed region at interfaces. Giant magnetoresistance and antiferromagnetic coupling of Co/Cu superlattices are governed by the events in thin region at interfaces less than 1 monolayer.

5.1 Introduction

Much attention has been devoted to the giant magnetoresistance (GMR) in magnetic superlattices [1]. The origin of the GMR has been mainly attributed to the spin-dependent scattering of free electrons at interfaces since the GMR was discovered [1]. It is pointed out theoretically and revealed experimentally that the GMR depends on interfacial roughness [2–7]. Based on the nuclear magnetic resonance (NMR) method, we reported in Chapter 3 and 4 that the Co/Cu superlattices with large MR value have the atomically rough interfaces, where Co and Cu atoms distribute randomly [8, 9]. From these previous investigations, we expect to enhance the value of MR by appropriate modifications of interfacial structures.

Another interest in this field is the oscillatory properties of antiferromagnetic (AF) coupling between adjacent magnetic layers [10–12]. The orientation dependence of AF coupling is suggested theoretically by Bruno and Chappert that AF coupling is stronger along <100> and <110> than along <111> [13]. However, experimental results of researchers on this subject are inconsistent [14–18]. Johnson *et al.* [16] and Parkin *et al.* [17] explained that these differing results were attributed to the ferromagnetic bridging through the pinholes. However, it is possible that AF coupling is also governed by the interfacial atomic distribution, since the preferred orientations are closely related to the interfacial atomic distribution.

In this chapter, we report the GMR and AF coupling of magnetron sputtered Co/Cu superlattices with an intentionally mixed interfacial region. AF coupling is broken down, and spin-independent scattering is enhanced by increasing the interfacial mixed region, while the spin-dependent scattering is

almost constant.

5.2 Experiment

The Co/Cu superlattices with artificially mixed interfaces were prepared in the same manner as described in Chapter 4, except for the substrates. The samples discussed in this chapter were deposited on a glass substrate. The amount of Co and Cu deposited in each Co/Cu bilayer was kept constant at 1.0 and 2.0 nm for pure Co and Cu. This combination of thickness of Co and Cu corresponds to the second peak of oscillatory properties of GMR and AF coupling as a function of Cu layer thickness [10–12]. Since the second peak is broader than the first peak around the Cu layer thickness of 1.0 nm (see Fig. 3.1), the influence of the variation of Cu layer thickness on the GMR and AF coupling is considered to be small.

The MR was measured at room temperature, using a conventional four-point geometry. The current is in the plane of the film with the magnetic field in-plane and orthogonal to the current direction. The in-plane magnetization of the samples was also measured with SQUID magnetometer at room temperature. The structures of samples were characterized by x-ray diffraction.

5.3 Results and discussion

Comparison of the magnetoresistance (MR) and magnetization curves between the samples with and without mixed interfaces is shown in Fig. 5.1. The MR ratio at magnetic field H is defined as $[\rho(H) - \rho_{\rm s}]/\rho_{\rm s}$, where $\rho(H)$ is the resistivity at the field of H, and $\rho_{\rm s}$ is the saturation resistivity. In

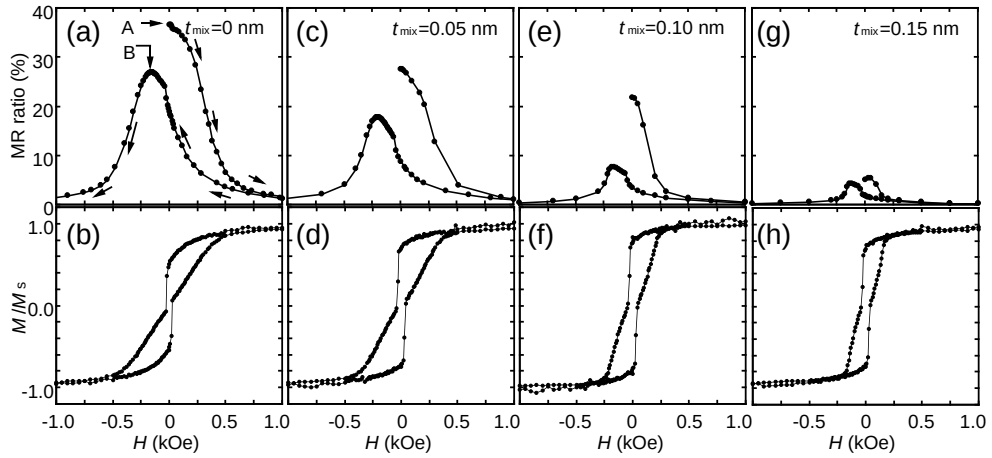

Fig. 5.1: Comparison of magnetoresistance and magnetization curves for the samples with different artificial mixed interfaces. All samples were deposited on an Fe (5.0 nm) buffer layer.

general, the resistivity of our samples decreased from the initial value, as indicated by arrow A in Fig. 5.1(a), with increasing H and saturated at the value of ρ_s in large field. After saturation, the resistivity is stabilized and has a peak at the finite field as indicated by arrow B in Fig. 5.1(a). For the sample without mixed region, the peak value of MR ratio is 27 %, while the initial value of MR ratio is 37 %. The magnetization of Co/Cu at the field of resistivity peak is almost zero if we correct the magnetization of the Fe buffer layer. For the Cu layers of 2.0 nm, the AF coupling is no longer strong enough, compared to the random coercive or pinning forces that oppose realignment with the magnetic layers, so that the magnetic configurations of the multilayers are not defined uniquely. According to Zhang and Levy [19], the sample of $t_{mix} = 0$ nm is considered to be a mixture of AF and the uncoupled configurations at the field of resistivity peak. The initial MR ratio of our sample at $H = 0$, where the magnetization of Co/Cu is completely

zero, was larger than the peak value of the MR ratio. These indicate that the Co/Cu superlattices are more completely AF coupled at the initial stage.

The value of MR ratio and saturation field H_s decrease with increasing t_{mix}. Figure 5.2 shows the variation of H_s, ρ_s, $\Delta\rho$ and $\Delta\rho_0$ with t_{mix}, where $\Delta\rho$ is the difference between ρ_s and peak resistivity ρ_p, and $\Delta\rho_0$ is the difference between ρ_s and initial resistivity ρ_0. Clearly, the H_s decreases with increasing t_{mix} to 0.15 nm, which is comparable with 1 ML. The decrease of H_s cannot be attributed to the increase of ferromagnetic bridging of Co layers through the pinholes due to the change in topological roughness. Figure 5.3 shows the low angle x-ray diffraction patterns of samples deposited on the Fe buffer layer of 5.0 nm. Since the amount of Co and Cu deposited in each Co/Cu bilayer was kept constant, there is not significant change in the position of the peak due to the artificial period. Moreover, the intensity and width of these peaks are also almost identical for all samples. As described in Chapter 4, no significant change in topological roughness can be found [9]. Therefore, the decrease of H_s is attributed to the weakening of AF coupling between adjacent Co layers.

It is remarkable that the interfacial mixing thinner than 1 ML breaks the interlayer AF coupling. This variation in AF coupling cannot be explained by the orientation dependence of AF coupling. Figure 5.4 shows the high angle x-ray diffraction patterns for samples with different t_{mix}. The sample without the mixed region shows the weak (111) and (200) diffraction peaks. For the sample with the mixed region of $t_{mix} = 0.05$ and 0.10 nm, the (111) diffraction peak disappears while the intensity of (220) peak increases. When the interfacial region is mixed by a 0.15 nm thickness, the diffraction pat-

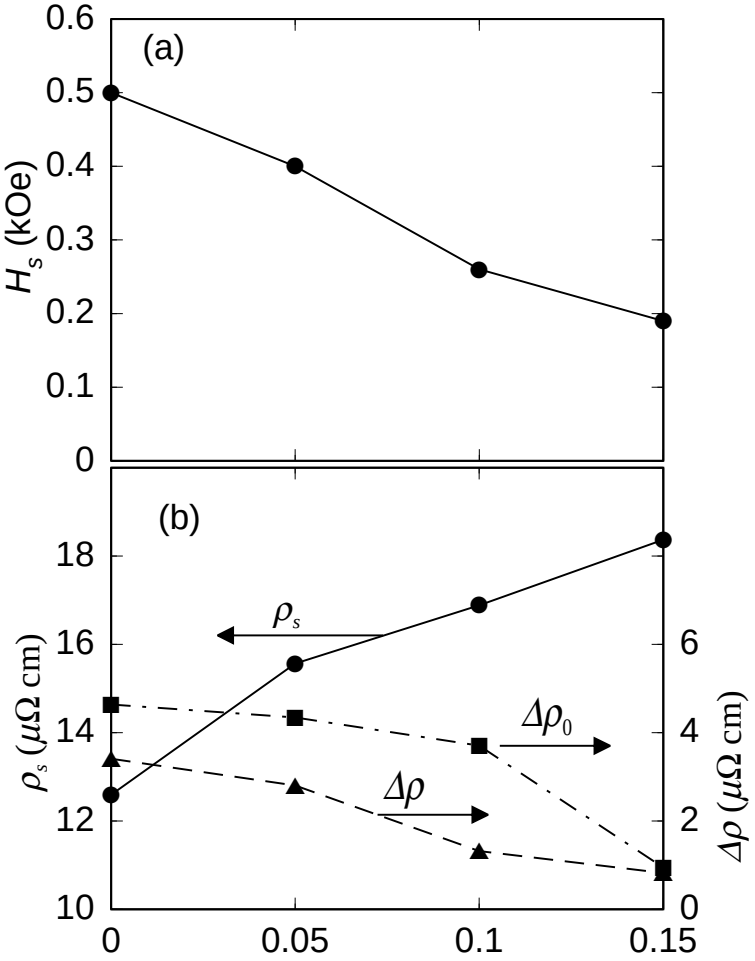

Fig. 5.2: The variation of the saturation field (a), saturation resistivity, and magnetoresistivity (b) depending on the thickness of mixed region for samples deposited on Fe (5.0 nm) buffer layer.

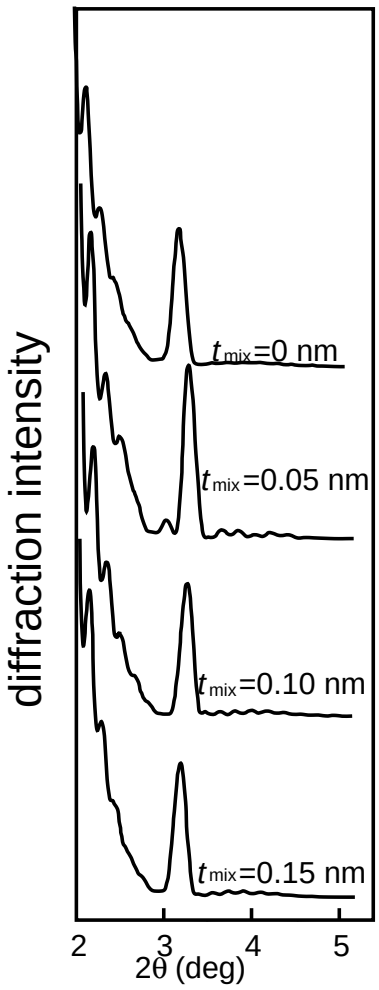

Fig. 5.3: Low angle x-ray diffraction patterns for the samples with artificial mixed interfaces of different thickness. All samples were deposited on an Fe (5.0 nm) buffer layer.

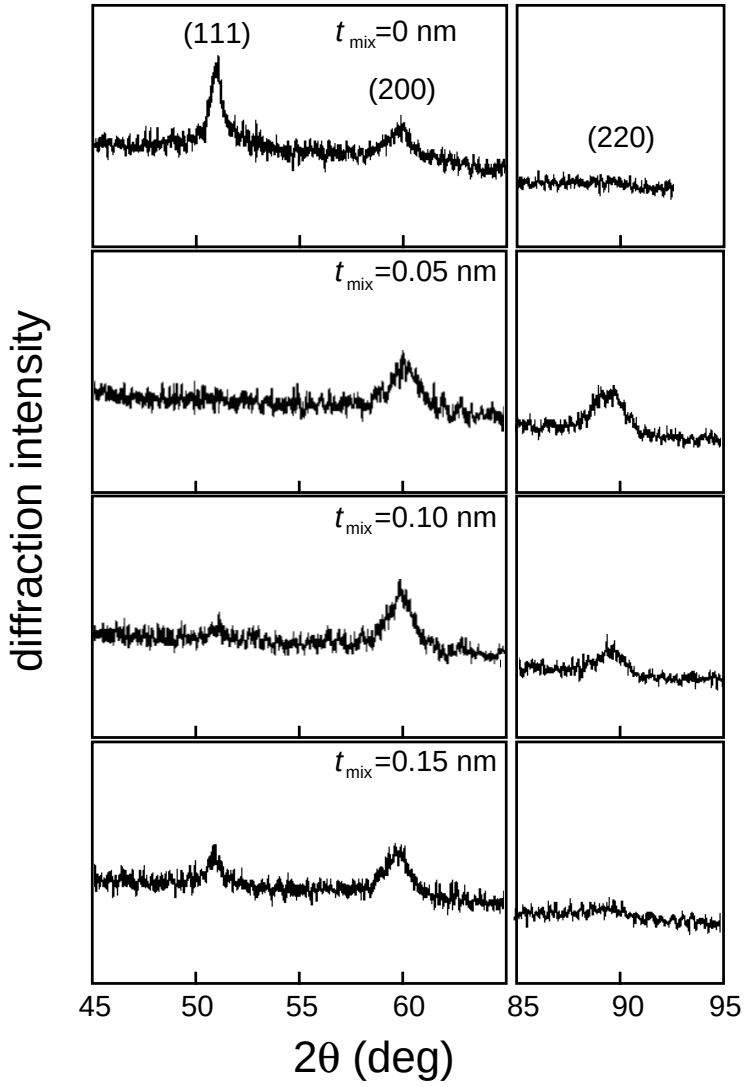

Fig. 5.4: High angle x-ray diffraction patterns for samples with artificial mixed interfaces of different thickness. All samples were deposited on an Fe (5.0 nm) buffer layer.

tern is similar to that of the sample without the mixed region. Therefore, it seems that there is no correlation between the preferred orientation and AF coupling. It is surprising that the addition of a very thin mixed region less than 1 ML changes the crystallinity of Co/Cu superlattices. This dependence of the preferred orientation on t_{mix} is a characteristic feature for the samples deposited on the glass substrate, and cannot be found for the samples deposited on the surface-oxidized Si substrate as shown in Chapter 4.

In previous studies, it was reported that strong AF coupling and larger MR were observed for magnetron sputtered Co/Cu and NiFe/Co superlattices with a weak tendency to (111) textured structure [8,14,18]. Egelhoff and Kief indicated that (111) stacked single crystal Co/Cu grown by molecular beam epitaxy (MBE) did not show the AF coupling [15]. Recently, Johnson *et al.* [16] and Parkin *et al.* [17], however, observed strong AF coupling for MBE grown (111) stacked and magnetron sputtered (111) textured Co/Cu superlattices. The complication between these investigations may be due to not only the ferromagnetic bridging, but also the existence of very thin interfacial mixing.

The weakening of AF coupling is one of the reasons why the MR ratio decreases with increasing t_{mix}. The other is the increase of saturation resistivity ρ_{s}, as shown in Fig. 5.2(b). The increase of ρ_{s} is attributed to the increase of spin-independent scattering. Therefore, the interfacial mixed region is considered to play a role in spin-independent scattering center.

We can expect that the highly disordered interfacial structure enhances the spin-dependent scattering. Oguri *et al.* suggest in their theoretical inves-

tigation that spin-dependent scattering is enhanced by increasing the degree of randomness of the interfacial atomic distribution [7]. In fact, Co and Cu atoms distribute randomly in the interfacial mixed region as described in the previous chapter. However, we can observe no significant enhancement of the spin-dependent scattering, since the $\Delta\rho_0$ is almost constant up to $t_{\mathrm{mix}} = 0.10$ nm. The dependence of $\Delta\rho_0$ on t_{mix} will be the results of not only the variation of the spin-dependent interfacial scattering but also the variation of the strength of the AF coupling. Thus, we can only conclude here that the interfacial scattering in Co/Cu superlattices is less spin-dependent than that in Fe/Cr superlattices in which the MR ratio increases with increasing interfacial roughness [2, 20]. Detailed analysis of the spin-dependence of the interfacial scattering will be discussed in the next chapter.

5.4 Conclusion

We have prepared Co/Cu superlattices with mixed region less than 1 ML on the glass substrates and have studied MR and AF coupling. The decrease of the MR ratio with increasing thickness of the mixed region can be attributed to the weakening of AF coupling and enhancement of spin-independent scattering of free electrons.

The interfacial mixed region discussed here is so thin that similar mixing can be formed in the deposition process or annealing after deposition. For example, many energetic ions and neutral particles bombard the sample surface during deposition by sputtering. The energy of these particles is sometimes great enough to cause interfacial mixing. Mixing by thermal diffusion also occurs, if the temperature of the samples rises during deposition.

We consider that the existence of the mixed regions complicates studies on AF coupling and GMR of the magnetic superlattice.

In the next chapter, we discuss the detailed properties of the interfacial scattering based on the temperature and magnetization dependence of the GMR.

References

[1] M. N. Baibich, J. M. Broto, A. Fert, F. Nguyen Van Dau, F. Petroff, P. Etienne, G. Creuzet, A. Friederich, and J. Chazelas, Phys. Rev. Lett. **61**, 2472 (1988).

[2] E. E. Fullerton, D. M. Kelly, J. Guimpel, I. K. Schuller, and Y. Bruynseraede, Phys. Rev. Lett. **68**, 859 (1992).

[3] Y. Saito, K. Inomata, A. Goto, and H. Yasuoka, J. Phys. Soc. Jpn. **62**, 1450 (1993).

[4] H. Hasegawa, Phys. Rev. B **42**, 2368 (1990).

[5] P. M. Levy, K. Ounadjela, S. Zhang, Y. Wang, C. B. Sommers, and A. Fert, J. Appl. Phys. **67**, 5914 (1990).

[6] Y. Wang, P. M. Levy, and L. L. Fry, Phys. Rev. Lett. **65**, 2732 (1990).

[7] A. Oguri, Y. Asano, and S. Maekawa, J. Phys. Soc. Jpn. **61**, 2652 (1992).

[8] M. Suzuki, Y. Taga, A. Goto, and H. Yasuoka, J. Magn. Magn. Mater. **126**, 495 (1993).

[9] M. Suzuki, Y. Taga, A. Goto, and H. Yasuoka, Phys. Rev. B **50**, 18580 (1994).

[10] S. S. P. Parkin, R. Bhadra, and K. P. Roche, Phys. Rev. Lett. **66**, 2152 (1991).

[11] D. H. Mosca, F. Petroff, A. Fert, P. A. Schroeder, W. P. Pratt Jr., and R. Laloee, J. Magn. Magn. Mater. **94**, L1 (1991).

[12] S. S. P. Parkin, Phys. Rev. Lett. **67**, 3598 (1991).

[13] P. Bruno and C. Chappert, Phys. Rev. Lett. **67**, 1602 (1991).

[14] M. E. Tomlinson, R. J. Pollard, D. J. Lord, and P. J. Grundy, J. Magn. Magn. Mater. **111**, 79 (1992).

[15] W. F. Egelhoff Jr. and M. T. Kief, Phys. Rev. B **45**, 7795 (1992).

[16] M. T. Johnson, R. Coehoorn, J. J. de Vries, N. W. E. McGee, J. aan de Stegge, and P. J. H. Bloemen, Phys. Rev. Lett. **69**, 969 (1992).

[17] S. S. P. Parkin, R. F. Marks, R. F. C. Farrow, G. R. Harp, Q. H. Lam, and R. J. Savoy, Phys. Rev. B **46**, 9262 (1992).

[18] R. Nakatani, T. Dei, and Y. Sugita, Jpn. J. Appl. Phys. **31**, L1417 (1992).

[19] S. Zhang and P. M. Levy, Phys. Rev. B **47**, 6776 (1993).

[20] F. Petroff, A. Barthélémy, A. Hamzić, A. Fert, P. Etienne, S. Lequien, and G. Creuzet, J. Magn. Magn. Mater. **93**, 95 (1991).

Chapter 6

GMR in Co/Cu superlattices with mixed interfaces II
∼ Mechanism of spin-dependent scattering

Abstract

We have measured both the magnetization and the temperature dependence of the giant magnetoresistance (GMR) in Co/Cu superlattices with different interfacial roughness. The magnetization dependence of the magnetoresistance (MR) has precluded the existence of a strong spin dependence in the potential not only for the bulk but also for the interfacial scattering. The temperature dependence of the GMR is hardly influenced by the interfacial roughness, while the residual resistivity changes significantly. The residual MR ratio decreases with increasing interfacial roughness. This reveals that the spin-dependent s–d scattering in the bulk is crucial for the GMR in Co/Cu superlattices. The interfacial roughness mainly contributes to the residual resistivity, and the spin dependence in the scattering at interfaces is weaker than that in the bulk.

6.1 Introduction

A great number of attempts have been made to clarify the origin of the giant magnetoresistance (GMR) observed in various magnetic multilayers [1–3]. Most of them have focused on the spin-dependent scattering of conduction electrons. Some theoretical studies attribute the GMR to the spin-dependent potential at interfaces [4–6]. In these theories, interfacial roughness is required as the scattering center. The strong spin-dependent scattering also comes from the spin-split density-of-states (SSDOS) for majority- and minority-spin d bands in the magnetic layers and occurs both in the bulk and at the interfaces [7, 8].

On the other hand, many experimental studies deal with the correlation between the GMR and the interfacial roughness to understand the role of interfaces [9–14]. For Fe/Cr superlattices [9, 10], the enhancement of both the magnitude and temperature dependence of the GMR due to interfacial roughness has been reported, so that the origin of the GMR in Fe/Cr is attributed to the interfacial scattering [5]. However, for transition metal/Cu superlattices, no one has reported that the interfacial roughness enhances the GMR [11–14]. Nevertheless, the importance of interfacial scattering has been pointed out indirectly in studies on the layer thickness dependence of the GMR [15, 16]. The mechanism of the GMR in transition metal/Cu superlattices still remains unclear.

This lack of understanding lies in the difficulty of quantitatively understanding the relationship between the interfacial structure and the transport properties since the interfacial structure is difficult to control and analyze. As reported in Chapter 4 [17], we succeeded in preparing Co/Cu superlat-

tices with well-controlled interfacial roughness. In these samples, only the atomic interfacial roughness has been modified, while the morphology and the crystallinity remain unchanged. This enables us to study the effect of interfacial roughness on the magnetization and the temperature dependence of the GMR. In this chapter, our experimental data are analyzed by the SSDOS model based on the theory proposed by Xing *et al.* [7,8]. The results suggest that the GMR in Co/Cu superlattices mainly comes from the spin-dependent *s*–*d* scattering in the Co layers.

6.2 Experiment

Since the details of the sample preparation and characterization have been reported in Chapter 2 and 4 [17], we only briefly describe them here. The Co/Cu superlattices with artificially mixed interfaces were deposited on an Fe buffer layer of a thickness of 5.0 nm prepared on a surface-oxidized Si substrate in the same manner as described in Chapter 4. The number of Co/Cu bilayers was 16, and the thicknesses of Co and Cu in a period were kept constant at 1.0 and 2.2 nm, respectively. The nominal structure of a sample was as follows: substrate/Fe(5.0)/Cu(2.2$-t_{\mathrm{mix}}/2$)/CoCu(t_{mix})/[Co(1.0$-t_{\mathrm{mix}}$)/CoCu(t_{mix})/Cu(2.2$-t_{\mathrm{mix}}$)/CoCu(t_{mix})]$_{15}$/Co(1.0$-t_{\mathrm{mix}}$)/Cu(2.2$-t_{\mathrm{mix}}/2$), where t_{mix} is the nominal thickness of the codeposited regions, and the values in the parentheses are the thickness of respective layers in unit of nm. The value of t_{mix} was varied between 0 and 0.25 nm. The thickness fluctuation of each layer, characterized using x-ray diffraction, was less than 0.1 nm for all samples independently of t_{mix}. On the other hand, ^{59}Co NMR revealed that Co and Cu atoms were atomically mixed at the interfaces and that the

amount of interfacial mixing increased according to the value of t_{mix}.

The in-plane magnetoresistance (MR) was measured with a standard dc four-terminal geometry as a function of the temperature in the range $2 \leq T \leq 300$ K. The dimension of the samples for the measurement was 2×15 mm^2, and the current used was 1 mA. This confirms that the resolution of the measured resistance is better than 10^{-3} Ω. In order to minimize the error due to the thermoelectric power in the measurement circuit, we averaged two sequential measurements with different polarities of the current. This sequence was repeated more than 50 times keeping the temperature constant for 10 min, and the collected data were averaged. The standard deviation for the data was smaller than the order of 10^{-4} Ω. The resistance-to-resistivity conversion was performed by scaling using the resistivity measured with samples at 300 K large enough to obtain an accuracy of 10^{-2} $\mu\Omega\,$cm. As a result, for one sample, the accuracy of the absolute value of resistivity was 10^{-2} $\mu\Omega\,$cm, while the resolution was better than 10^{-3} $\mu\Omega\,$cm. Furthermore, the scattering of the data due to the sample reproducibility, which was obtained from measurements for five series of samples, was within ± 1 $\mu\Omega\,$cm.

The magnetization was also measured with a superconducting quantum interface device (SQUID) magnetometer.

6.3 Results and discussion

6.3.1 Relationship between GMR and magnetization

Figure 6.1 shows the MR curves measured at 5 K for one of the series of the samples with different t_{mix}. The MR ratio is defined as $(\rho - \rho_{\mathrm{s}})/\rho_{\mathrm{s}}$, where ρ is the resistivity in an arbitrary field and ρ_{s} is the saturation resistivity. In

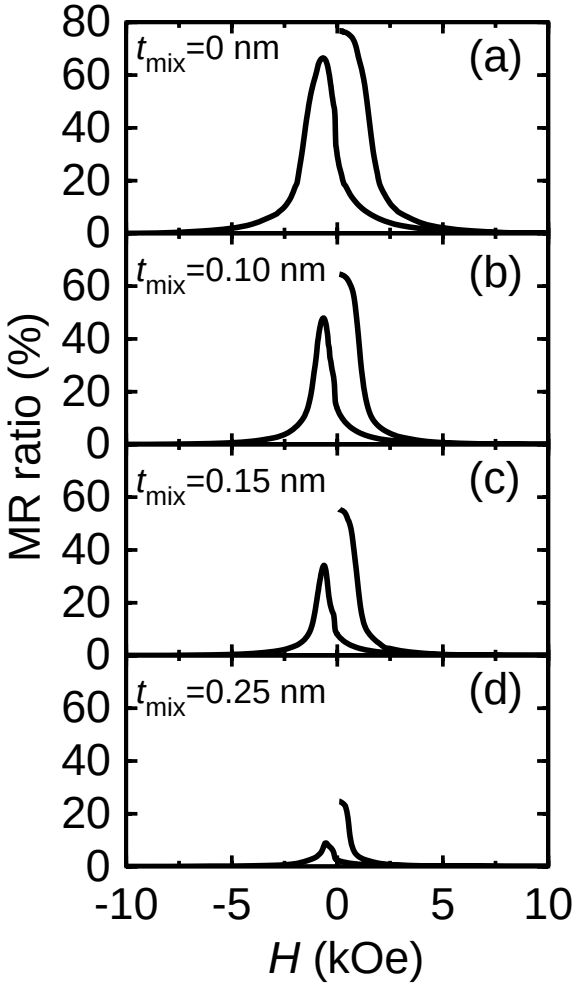

Fig. 6.1: The magnetoresistance curves measured at 5 K for samples with different interfacial roughness.

general, the resistivity of our samples decreases from the initial value with increasing magnetic field H and saturates at the value of ρ_s in a field larger than the saturation field H_s. After saturation, the resistivity has a peak near the coercive field. Since the value of the initial resistivity is larger than that of the peak one, the antiferromagnetic (AF) alignment of the magnetization of the Co layers is closer to perfection at the initial state than that in the field where the resistivity has the peak.

Figure 6.2 shows the relationship between ρ and $(M/M_s)^2$ during the initial magnetization process, where M is the total magnetization and M_s is the total saturation magnetization of the samples. In this figure, the magnetization of the Fe buffer layer is corrected for. The linear dependence on $(M/M_s)^2$ at 5 K is clearly observed for all the samples. On the other hand, at 300 K, ρ no longer depends linearly on $(M/M_s)^2$, and no significant enhancement of the deviation from $(M/M_s)^2$ dependence due to the interfacial roughness is observed. In order to describe the magnetization dependence of the GMR in Co/Cu, we use a two-current model with spin mixing [18]. It gives the electrical resistivity

$$\rho = \frac{\rho_\uparrow \rho_\downarrow + \rho_{\uparrow\downarrow}\left(\rho_\uparrow + \rho_\downarrow\right)}{\rho_\uparrow + \rho_\downarrow + 4\rho_{\uparrow\downarrow}}, \tag{6.1}$$

where $\rho_\uparrow$, $\rho_\downarrow$, and $\rho_{\uparrow\downarrow}$ are the resistivity of spin-$\uparrow$ and spin-$\downarrow$ channels and spin mixing, respectively. In the temperature range where $\rho_\uparrow$ and $\rho_\downarrow$ are much larger than $\rho_{\uparrow\downarrow}$, one derives the following from Eq. (6.1):

$$\rho = \frac{\rho_\uparrow \rho_\downarrow}{\rho_\uparrow + \rho_\downarrow} + \frac{\left(\rho_\uparrow - \rho_\downarrow\right)^2}{\left(\rho_\uparrow + \rho_\downarrow\right)^2}\rho_{\uparrow\downarrow}. \tag{6.2}$$

When the mean free path of conduction electrons is longer than the super-

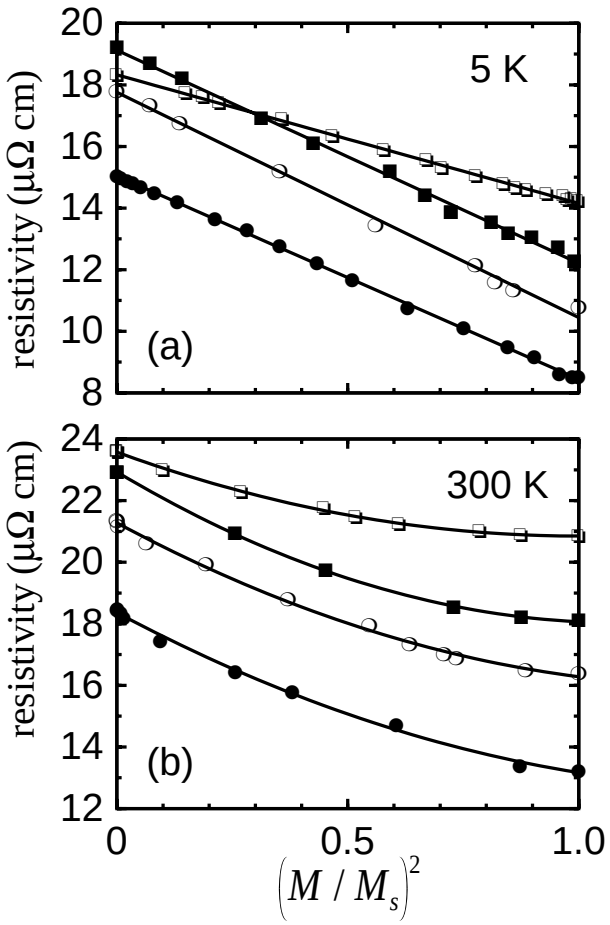

Fig. 6.2: The relationship between $\rho(m)$ and $(M/M_s)^2$ during the initial magnetization process measured at 5 K (a) and 300 K (b) for the samples of $t_{mix} = 0$ (•), 0.10 (○), 0.15 (■), and 0.25 (□) nm. The magnetization of the Fe buffer layer is corrected for. The lines indicate a guide for the eyes.

lattice period, $\rho_\uparrow$ and $\rho_\downarrow$ are given as [7, 8, 19]

$$\begin{aligned}\rho_\uparrow(m) = \quad & \frac{\eta}{2}\left\{\frac{2(1-\eta)}{\eta}\rho_N + \rho_+ + \rho_-\right\} \\ & + \frac{\eta}{2}(\rho_+ - \rho_-)m, \end{aligned} \tag{6.3}$$

$$\begin{aligned}\rho_\downarrow(m) = \quad & \frac{\eta}{2}\left\{\frac{2(1-\eta)}{\eta}\rho_N + \rho_+ + \rho_-\right\} \\ & - \frac{\eta}{2}(\rho_+ - \rho_-)m, \end{aligned} \tag{6.4}$$

where ρ_N is the resistivity of the nonmagnetic layer, ρ_+ and ρ_- are the resistivities of the magnetic layer for majority- and minority-spin electrons, respectively, and η is the thickness fraction of the magnetic layer in one superlattice period. The value of m is determined by the geometric configuration of the magnetization of the magnetic layers. For completely AF coupled superlattices, $m = M/M_\mathrm{s}$ [7, 8, 20]. We write here the resistivities for both spin channels as $\rho_\uparrow(m)$ and $\rho_\downarrow(m)$ to express the dependence on m explicitly. Substituting Eqs. (6.3) and (6.4) into Eq. (6.2), the resistivity in a field is given by

$$\rho(m) = \rho_\mathrm{AF} - \left\{\frac{\eta\,(\rho_+ - \rho_-)}{4}\right\}^2 \left(1 - \frac{\rho_{\uparrow\downarrow}(m)}{\rho_\mathrm{AF}}\right)\frac{m^2}{\rho_\mathrm{AF}}, \tag{6.5}$$

where ρ_AF is the resistivity when the magnetization of the magnetic layers is perfectly AF aligned and is written as

$$\rho_\mathrm{AF} \equiv \rho(m=0) = \frac{\eta}{4}\left\{\frac{2\,(1-\eta)}{\eta}\rho_N + \rho_+ + \rho_-\right\}. \tag{6.6}$$

Here, we allow the spin mixing to depend on m. As can be seen from Eq. (6.5), $\rho(m)$ changes linearly with m^2, when $\rho_{\uparrow\downarrow}(m)$ is negligible. If the AF alignment of the magnetization of Co is perfect, $\rho(m)$ changes linearly with

$(M/M_s)^2$ [20]. Therefore the magnetic configuration of our samples is very close to the perfect AF alignment at the initial state (see Fig. 6.2). Nevertheless, the magnitude of the saturation MR ratio decreases with increasing t_{mix} as shown in Fig. 6.1. This indicates that the spin dependence in the scattering of conduction electrons from interfacial roughness is weaker than that in the Co layers.

In addition to the imperfect AF alignment, the spin mixing [7, 8] and Hasegawa's valve effect [21,22] cause deviation from the $(M/M_s)^2$ dependence of $\rho(m)$. Thus the existence of significant spin mixing and the valve effect are precluded for our samples at 5 K. Xing *et al.* [7, 8] indicated that the spin mixing at low temperature comes from the spin-dependent diagonal matrix elements of the potential for the scattering of electrons with each spin direction. They showed that it made the resistivity larger than the $(M/M_s)^2$ dependence in any field of $0 < H < H_s$. The present result suggests that the spin dependence in the scattering potential for both bulk and interfacial scattering is not very strong. Therefore the GMR in Co/Cu arises from the spin-dependent *s*–*d* scattering rate due to the different density of states (DOS) for majority- and minority-spin *d* bands in the magnetic layer.

The deviation from $(M/M_s)^2$ dependence at 300 K is likely to be due to the spin mixing. Since $\rho(m)$ deviates downwards from the linear dependence on $(M/M_s)^2$ in a field of $0 < H < H_s$, this does not come from the spin dependence of the scattering potential. We believe that the spin mixing at 300 K is due to thermal excitation of magnons and we have to take account of not only the diagonal but also the off-diagonal matrix elements. However, the interfacial roughness does not play an important role in the spin mixing,

since no significant difference in the magnitude of the deviation from the $(M/M_s)^2$ dependence between the samples with different t_{mix} is observed.

6.3.2 Temperature dependence of GMR

We examined the effect of the interfacial roughness on the temperature dependence of the GMR with our attention on the initial resistivity ρ_0 and the saturation resistivity ρ_s. As mentioned above, the samples in the initial state have almost perfect AF alignment. Furthermore, we can keep the magnetic configuration constant during the measurements of temperature dependence of ρ_0 and ρ_s. Figure 6.3 shows the temperature dependence of ρ_0 and ρ_s together with that of $\Delta\rho_0 = \rho_0 - \rho_s$ for the samples of various t_{mix}. With increasing temperature, both ρ_0 and ρ_s increase due to electron-phonon, electron-magnon, or other scattering processes. The residual resistivity of ρ_s increases with increasing t_{mix} due to the increase in interfacial scattering, though the difference in the temperature coefficient is small. Since the temperature coefficient of ρ_s is larger than that of ρ_0, $\Delta\rho_0$ decreases with increasing temperature. The deviations of ρ_0 and ρ_s from their values at 2 K are shown in Fig. 6.4. A minimum in ρ_0 is found at around 15 K for the samples of $t_{mix} \leq 0.15$ nm, while ρ_s increases monotonically with increasing temperature. As indicated in Ref. [23], the minimum in ρ_0 is the characteristic feature for AF coupled Co/Cu superlattices. However, the minimum is not found for the sample of $t_{mix} = 0.25$ nm.

Since the spin mixing does not contribute to ρ_0 explicitly [see Eq. (6.5)], the spin mixing in ρ_s is one of the processes reducing the value of $\Delta\rho_0$ with increasing temperature. However, the minimum in ρ_0 [Fig. 6.4(a)] indicates

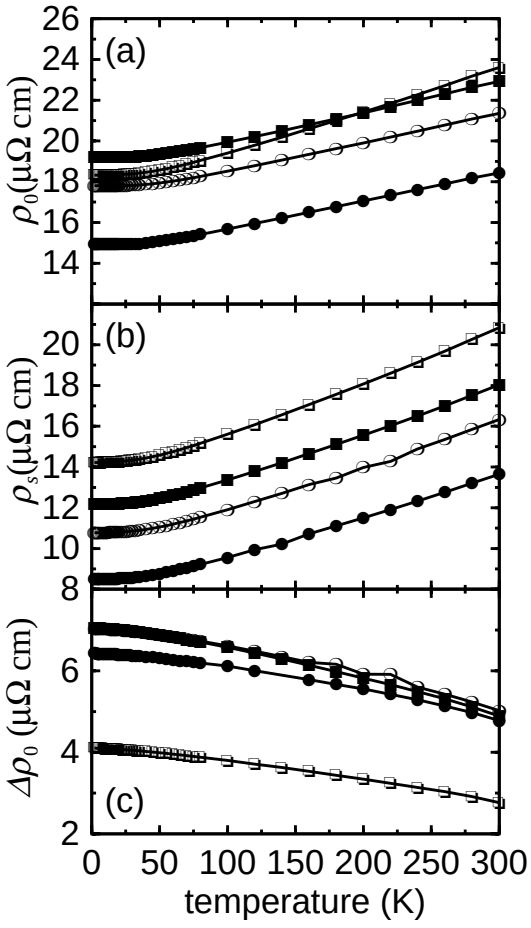

Fig. 6.3: Temperature dependence of (a) ρ_0, (b) ρ_s, and (c) $\Delta\rho_0$ for the samples of $t_{mix} = 0$ (•), 0.10 (○), 0.15 (■), and 0.25 (□) nm. Note that the vertical scale for (c) is different from the others. The lines indicate a guide for the eyes.

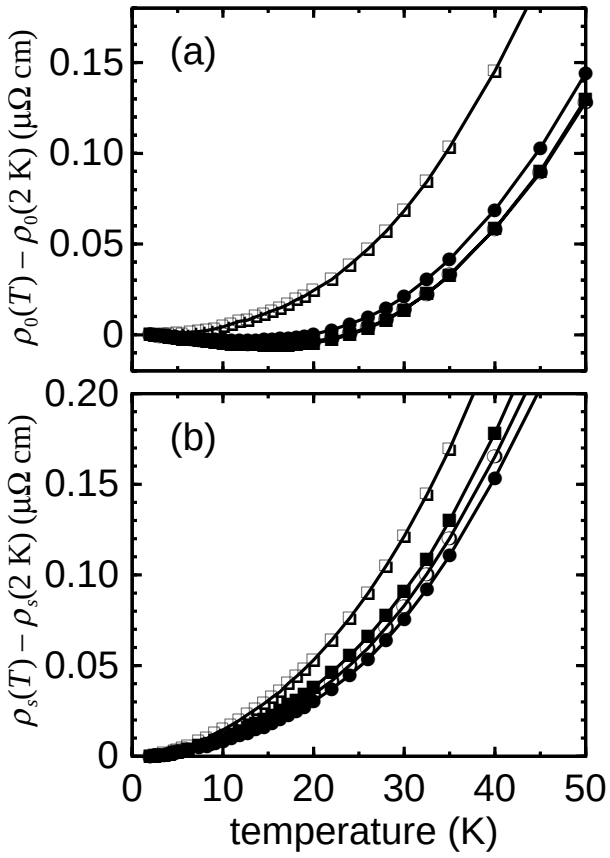

Fig. 6.4: Deviation of (a) ρ_0 and (b) ρ_s from their values at 2 K for the samples of $t_{mix} = 0$ (•), 0.10 (○), 0.15 (■), and 0.25 (□) nm. The lines indicate a guide for the eyes.

that there exist other processes of reducing the GMR. The difference in the scattering mechanism would be reflected in the power law for the temperature dependence of the resistivity. Thus we focus here on the power law for $\Delta\rho_0$ and ρ_s. Before we discuss the effect of interfacial roughness on the temperature dependence of $\Delta\rho_0$ and ρ_s, we deduce the general expression for them in any given field. Defining the MR in any given field as $\Delta\rho(m) \equiv$

$\rho(m) - \rho(m=1) = \rho(m) - \rho_{\rm s}$, Eq. (6.4) is written as

$$\Delta\rho(m) = \left\{\frac{\eta\,(\rho_+ - \rho_-)}{4}\right\}^2 \frac{1}{\rho_{\rm AF}} \left\{1 - m^2 - \frac{\rho_{\uparrow\downarrow}(m=1) - m^2\rho_{\uparrow\downarrow}(m)}{\rho_{\rm AF}}\right\}. \quad (6.7)$$

In the temperature range where $\rho_{\uparrow\downarrow} \ll \rho_{\rm AF}$,

$$\Delta\rho(m) = \left(1 - m^2\right)(\rho_{\rm AF} - \rho_{\rm s})\,. \quad (6.8)$$

Equation (6.8) indicates that $\Delta\rho(m)$ is proportional to $\rho_{\rm AF} - \rho_{\rm s}$, whenever the geometric factor m is kept constant. Note that this is correct even in the case that the AF alignment of magnetization of Co is imperfect (nonzero m). In the high temperature region, care must be taken to interpret the temperature dependence of $\Delta\rho(m)$, since the spin mixing comes into the expression for $\Delta\rho(m)$.

Figures 6.5 and 6.6 show double logarithmic plots of $\rho_{\rm s}(T) - \rho_{\rm s}(2\ {\rm K})$ and $\Delta\rho_0(2\ {\rm K}) - \Delta\rho_0(T)$. At temperatures lower than 100 K, $\rho_{\rm s}$ closely approximates a T^2 power law. The temperature dependence of $\rho_{\rm s}$ changes to T^n ($n = 1-1.5$) over 100 K. This temperature dependence cannot be attributed only to the spin mixing, since spin mixing obeys a $T^{3/2}$ power law at low temperatures and a T^2 power law at high temperatures [18]. The spin mixing found in Fig. 6.2(b) will be superimposed on the large temperature dependence due to other excitations. The electron-electron or electron-magnon scattering is a possible mechanism to explain the T^2 dependence, although details of the process have not been clarified. On the other hand, $\Delta\rho_0$ changes linearly with $T^{3/2}$ over the whole measurement temperature range. As can be seen from Eqs. (6.6) and (6.7), decrease in $\Delta\rho_0$ is caused by a decrease in $|\rho_+ - \rho_-|$ and increase in $\rho_{\rm AF}$. Since $1/\rho_{\rm AF}$ does not simply depend on

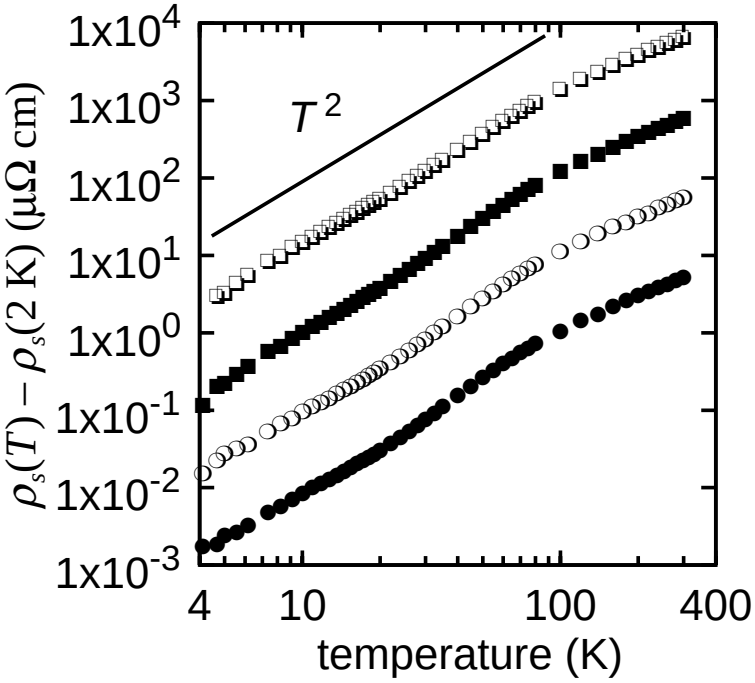

Fig. 6.5: Double logarithmic plot of $\rho_{\rm s}(T) - \rho_{\rm s}(2\ {\rm K})$ versus temperature for the samples of $t_{\rm mix} = 0$ (•), 0.10 (○), 0.15 (■), and 0.25 (□) nm. For the better understanding, the data for the sample of $t_{\rm mix}$ =0.10, 0.15, and 0.25 nm are multiplied by 10, 10^2,and 10^3, respectively.

$T^{3/2}$, the term $|\rho_+ - \rho_-|$ plays an important role in the temperature dependence of $\Delta\rho_0$. Since $|\rho_+ - \rho_-|$ reflects the difference in population between the majority- and minority-spin d bands in Co, it should be closely related to the spontaneous magnetization. Saito *et al.* [23] indicated that $\Delta\rho_0$ and the spontaneous magnetization showed a similar temperature dependence. In fact, the spontaneous magnetization of our samples also shows the $T^{3/2}$ dependence. However, the relationship between them is more complicated than a simple linear relation.

As shown in Figs. 6.5 and 6.6, the power laws for $\Delta\rho_0$ and $\rho_{\rm s}$ are inde-

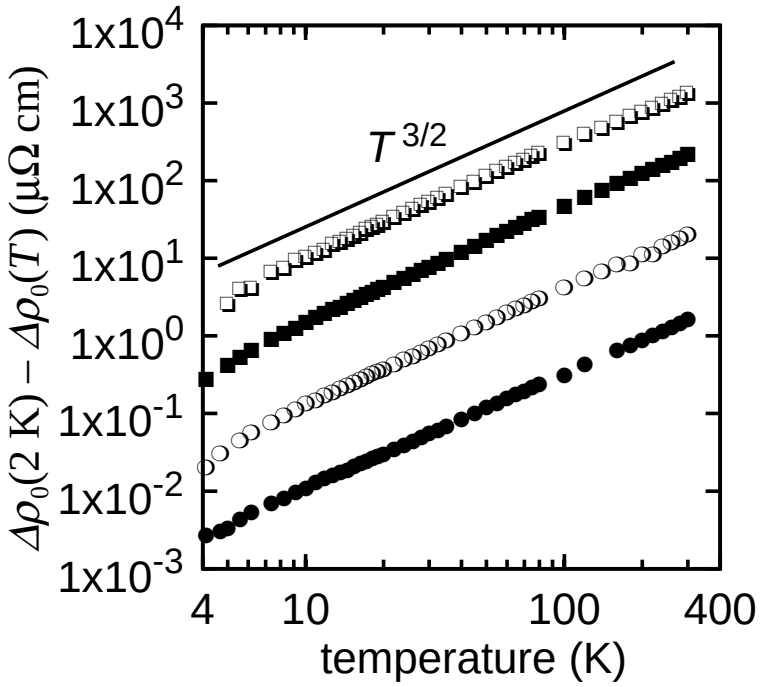

Fig. 6.6: Double logarithmic plot of $\Delta\rho_0(2\text{ K}) - \Delta\rho_0(T)$ versus temperature for the samples of $t_{\text{mix}} = 0$ (•), 0.10 (○), 0.15 (■), and 0.25 (□) nm. For the better understanding, the data for the sample of t_{mix} =0.10, 0.15, and 0.25 nm are multiplied by 10, 10^2,and 10^3, respectively.

pendent of t_{mix}, although the residual $\Delta\rho_0$ and ρ_{s} change significantly due to the increase in interfacial roughness (see Fig. 6.3). This suggests that the interfacial scattering mainly contributes to the residual resistivity, while the temperature dependence mainly comes from the bulk scattering. On the assumption that the bulk scattering is crucial for the GMR, the small value of $\Delta\rho_0$ for the sample of $t_{\text{mix}} = 0.25$ nm is likely to be attributed to the decrease in the effective thickness of Co layers due to the significant interfacial mixing. As a result, the minimum in ρ_0 is only found for the samples of $t_{\text{mix}} \leq 0.15$ nm but not for the sample of $t_{\text{mix}} = 0.25$ nm.

In the SSDOS model for GMR, the scattering of s electrons to unfilled d bands with a large difference in the DOS is crucial [7,8]. In the Co/Cu superlattices, s electrons near the Fermi level do not experience a large potential difference at any of the interfaces [19], since the s bands for Co and Cu are well aligned. Therefore s electrons have almost free-electron-like properties. On the other hand, the d band in Cu and the majority-spin d band in Co lie well below the Fermi level, while the minority-spin d band in Co has a large DOS at the Fermi level [24]. Thus the minority-spin d band may be localized in the Co layers. In this situation, the wave function of the electron in the minority-spin d band does not have a large amplitude near the Co/Cu interface, while that of s-electrons shows no considerable change in the superlattice. Therefore the interfacial roughness will weaken the spin dependence in the scattering.

There are many studies attributing the origin of the GMR in Co/Cu superlattices to interfacial scattering [15,16]. Most of them are accomplished by measuring the dependence of the GMR on the thickness of the magnetic layers. However, the thickness dependence reveals only that the scattering centers are concentrated in a small region. We propose a hypothesis that the scattering centers causing the GMR are *in* the Co layer and concentrated *near* the interfaces. To verify the hypothesis, a detailed structural analysis to clarify the position and the kind of the scattering centers will be required.

6.4 Conclusion

We have measured the magnetization and temperature dependence of the GMR in Co/Cu superlattices with artificially modified interfaces. The mag-

netization dependence indicates that there is no significant spin dependence in the potentials for the bulk and interfacial scattering. The temperature dependence of the GMR is almost independent of the interfacial roughness, while the residual resistivity changes significantly. The residual MR ratio decreases with increasing interfacial roughness. A logical conclusion is, therefore, that the spin-dependent bulk s–d scattering is crucial for the GMR in Co/Cu superlattices.

References

[1] M. N. Baibich, J. M. Broto, A. Fert, F. Nguyen Van Dau, F. Petroff, P. Etienne, G. Creuzet, A. Friederich, and J. Chazelas, Phys. Rev. Lett. **61**, 2472 (1988).

[2] S. S. P. Parkin, R. Bhadra, and K. P. Roche, Phys. Rev. Lett. **66**, 2152 (1991).

[3] D. H. Mosca, F. Petroff, A. Fert, P. A. Schroeder, W. P. Pratt Jr., and R. Laloee, J. Magn. Magn. Mater. **94**, L1 (1991).

[4] P. M. Levy, S. Zhang, and A. Fert, Phys. Rev. Lett. **65**, 1643 (1990).

[5] S. Zhang and P. M. Levy, Phys. Rev. B **43**, 11048 (1991).

[6] J. Inoue, A. Oguri, and S. Maekawa, J. Phys. Soc. Jpn. **60**, 376 (1991).

[7] L. Xing and Y. C. Chang, Phys. Rev. B **48**, 4156 (1993).

[8] L. Xing, Y. C. Chang, M. B. Salamon, D. M. Frenkel, J. Shi, and J. P. Lu, Phys. Rev. B **48**, 6728 (1993).

[9] F. Petroff, A. Barthélémy, A. Hamzić, A. Fert, P. Etienne, S. Lequien, and G. Creuzet, J. Magn. Magn. Mater. **93**, 95 (1991).

[10] E. E. Fullerton, D. M. Kelly, J. Guimpel, I. K. Schuller, and Y. Bruynseraede, Phys. Rev. Lett. **68**, 859 (1992).

[11] M. J. Hall, B. J. Hickey, M. A. Howson, C. Hammond, M. J. Walker, D. G. Wright, D. Greig, and N. Wiser, J. Phys. Condens. Mater. **4**, L495 (1992).

[12] Y. Saito, K. Inomata, A. Goto, and H. Yasuoka, J. Phys. Soc. Jpn. **62**, 1450 (1993).

[13] V. S. Speriosu, J. P. Nozieres, B. A. Gurney, B. Dieny, T. C. Huang, and H. Lefakis, Phys. Rev. B **47**, 11579 (1993).

[14] M. Suzuki and Y. Taga, J. Appl. Phys. **74**, 4660 (1993).

[15] S. S. P. Parkin, Phys. Rev. Lett. **71**, 1641 (1993).

[16] S. K. J. Lenczowski, M. A. M. Gijs, J. B. Geisbers, R. J. M. van de Veerdonk, and W. J. M. de Jonge, Phys. Rev. B **50**, 9982 (1994).

[17] M. Suzuki, Y. Taga, A. Goto, and H. Yasuoka, Phys. Rev. B **50**, 18580 (1994).

[18] A. Fert and I. A. Campbell, J. Phys. C **6**, 849 (1976).

[19] D. M. Edwards, J. Mathon, and R. B. Muniz, IEEE Trans. Magn. **27**, 3548 (1991).

[20] J. Shi, S. S. P. Parkin, L. Xing, and M. B. Salamon, J. Magn. Magn. Mater. **125**, L251 (1993).

[21] H. Hasegawa, Phys. Rev. B **47**, 15073 (1993).

[22] H. Hasegawa, Phys. Rev. B **47**, 15080 (1993).

[23] Y. Saito, K. Inomata, S. Uji, T. Terashima, and H. Aoki, J. Phys. Soc. Jpn. **63**, 1263 (1994).

[24] R. A. Ballinger and C. A. W. Marshall, J. Phys. F **3**, 735 (1973).

Chapter 7

Influence of bound d state on GMR

Abstract

We discuss the giant magnetoresistance (GMR) in magnetic superlattices with an s–d scattering model on the assumption that d states are bound in magnetic layers. The GMR is calculated by using the quantum Boltzmann equation using Kronig-Penney type potentials. Spin-dependent interfacial scattering depends on the number of scatterers, the height of the scattering potentials and the amplitude of the wave function of the d state at interfaces, while spin-dependent bulk scattering is attributed to the spin-dependent density of states (DOS) of d states. Our model agrees well with the measured GMR in Co/Cu superlattices with artificially mixed interfaces, when we assume that the minority spin d states are strongly bound in Co layers. Therefore, the spin-dependent scattering in Co/Cu superlattices is attributed to the spin-dependent DOS of the d states in the Co layers.

7.1 Introduction

The giant magnetoresistance (GMR) exhibited in many magnetic superlattices and granular alloys arises from the spin-dependent scattering of conduction electrons [1–5]. It has been pointed out that the interfacial scattering of conduction electrons plays an important role in the spin-dependent scattering [1]. For M/Cu (M =Co, NiFe) systems, however, no one has reported the enhancement of the GMR owing to the interfacial roughness [6–10]. In Chapter 6 [7], we have reported that the spin-dependent bulk scattering is important for the occurrence of the GMR. On the other hand, Parkin [11] has reported that the GMR is enhanced by very thin Co layers inserted at interfaces of NiFe/Cu multilayers. He claimed that the *interfacial state* as well as roughness plays an important role in the GMR. These experimental results require a theory to take account of both the spin-dependent bulk scattering and the interfacial electronic states.

For M/Cu systems, Edwards *et al.* [12] and Xing *et al.* [13, 14] insist on the importance of a spin-dependent density of states (DOS) of d bands in magnetic layers. In these models, the GMR is attributed to the scattering of s electrons to unfilled d bands which have spin-dependent DOS. These models semi-quantitatively agree with the layer thickness dependence of GMR in M/Cu systems. However, the influence of the interfacial state has not been treated explicitly, since the Fermi surfaces of s and d bands are treated as simple sphere. Recently, Schep *et al.* [15] calculated the GMR in a method based on the full electronic structure. They reported the importance of the s–d hybridization for the origin of the GMR in the current-perpendicular-to-the-plane (CPP) geometry. However, their theory does not satisfactorily

explain the considerable MR observed in the current-in-the-plane (CIP) geometry. They suggest that some additional scattering mechanism is necessary for explaining the CIP MR.

In this chapter, we have extended the resistor network theory to include the interfacial state explicitly, on the basis of the method developed by Visscher [16]. The simple expression we have deduced neglecting the s–d hybridization agrees well with our experimental results of the GMR observed in CIP geometry for the Co/Cu superlattices with artificially mixed interfaces.

7.2 Model

We confine our discussions to low temperatures, neglect magnon and phonon scattering and assume that the effective mean free path of the conduction electrons is much larger than the superlattice period. This assumption limits our discussion to scattering processes that do not cause spin mixing, so that the current is carried separately by up- and down-spin conduction electrons (two-current model) as [17]

$$\rho = \frac{\rho_\uparrow \rho_\downarrow}{\rho_\uparrow + \rho_\downarrow}, \tag{7.1}$$

where $\rho_\uparrow$ and $\rho_\downarrow$ are the resistivity of up- and down-spin channels, respectively, and ρ is the total resistivity. We assume that the current is carried only by s electrons and neglect the current carried by d electrons with heavy effective mass. The non-zero residual resistivity is due to the scattering of s electrons by impurities or defects at $\mathbf{r}_{\mathrm{SC}}$ with a potential of the form

$$V(\mathbf{r}) = V_0 \delta(\mathbf{r} - \mathbf{r}_{\mathrm{SC}}). \tag{7.2}$$

In the transition metals, the s electrons can be scattered into holes in s band (s–s scattering) or d band (s–d scattering) when they are scattered either at interfaces or inside layers. The scattering rate of s–s and s–d scattering will be determined by the scattering amplitude for the transition between an initial and a final state and the availability of states into which the electrons can be scattered. Since only electrons near Fermi surface contribute to the resistivity, these scattering rate can be written in terms of Fermi's golden rule as

$$P_{if}^{\sigma} = \frac{2\pi}{\hbar} \left| \left\langle \Phi_f^{\sigma} | V(\mathbf{r}) | \Psi_i^{\sigma} \right\rangle \right|^2 N(E_{\mathrm{F}}), \tag{7.3}$$

where Ψ_i^{σ} and Φ_f^{σ} are an initial s and a final s or d state for the σ spin, respectively, and $N(E_{\mathrm{F}})$ is the DOS of the final state at the Fermi energy E_{F}. The total scattering rate is the summation of the s–s and s–d scattering rate. Therefore, the properties of s and d bands near the Fermi surface play an important role in the GMR. We treat the s and d bands with the effective-mass approximation. Since the CIP MR due to s–d hybridization is small [15], we neglect it and assume that the bulk of each metal constituting the superlattice has two free electron bands with different effective masses. One corresponds to an s band, and another corresponds to a d band. The effective masses and potentials for the bands may depend on spin directions for the ferromagnetic metals. When two metals are layered alternately, the superlattice states will be formed owing to the potential modulation. For systems such as M/Cu, s electrons see small potential differences at interfaces between magnetic and nonmagnetic layers, since the bottoms of s bands of these metals are well aligned on the scale of the Fermi energy [18,19]. Owing to the superlattice state due to the superlattice potential, the anisotropy in

the Fermi wave number will arise. Although this anisotropy affects the CPP MR, its influence on the CIP MR can be negligible [20]. This means that the s states can be treated as simple plain waves when the potential differences are small. For simplicity, we assume that s electrons do not see any potential differences when crossing the interfaces between magnetic and non-magnetic layers, since we are now interested in the CIP MR. On the other hand, d states see a large potential difference at interfaces, since there is an exchange interaction in ferromagnetic layers. Assuming the superlattice to be infinite in the z direction, the superlattice potentials are modeled by Kronig-Penney-type potentials. We assume that the potentials for the d states are constant within each layer but depend on spin and material. For systems such as M/Cu, the d band of Cu and the majority-spin d band of the ferromagnetic layers lie well below the Fermi energy, so they do not contribute to the resistivity [18, 19]. Therefore, we take account of only the minority-spin d band of ferromagnetic layers. The potential for the d band is composed of a periodic array of barriers of thickness a with height U_{b} and wells of thickness b with depth U_{w} as shown in Fig. 7.1. For a ferromagnetic (F) configuration of the magnetization of ferromagnetic layers, the potential for down-spin electrons has $a = t_{\mathrm{NM}}$ and $b = t_{\mathrm{M}}$, where t_{NM} is the thickness of nonmagnetic layers and t_{M} of magnetic layers; for up-spin electrons, $b = 0$, i.e., there are no wells. For antiferromagnetic (AF) configurations, the potentials for up- and down-spin electrons are the same and are shifted in space relative to one another; $a = 2t_{\mathrm{NM}} + t_{\mathrm{M}}$ and $b = t_{\mathrm{M}}$. The potential for the s band is at U_s and is constant in a superlattice as mentioned above. For these step-function potentials, we calculate the scattering matrix elements from

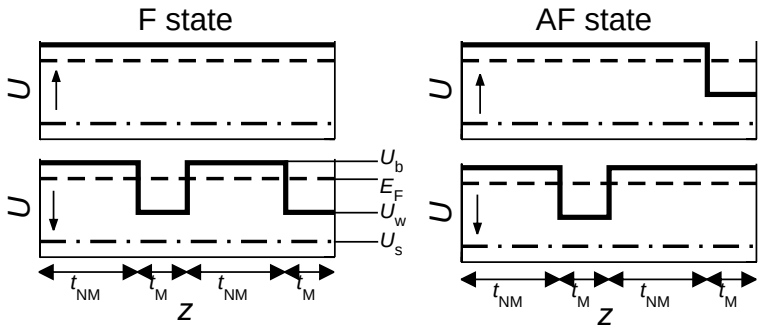

Fig. 7.1: A schematic diagram of the superlattice potentials for ferromagnetic (F state) and antiferromagnetic (AF state) configuration and for electrons with up (↑) and down (↓) spin. The lines indicate the potentials for d states (solid lines), the potentials for s states (dashed and dotted lines) and the Fermi energy (dashed lines).

the exact quantum-mechanical wave functions.

7.3 Superlattice state for d band

Since the potential for s electrons is constant in the superlattice, s electrons travel in the superlattice as ordinary plane waves. Thus, the Fermi surface of the s band is spherical. However, the Fermi surface of the d band is no longer spherical due to the superlattice potential. In order to calculate the resistivity, we must know the shape of the Fermi surface of the d band. The wave functions of the d state $\Psi(\mathbf{r})$ have the Bloch form

$$\Psi(\mathbf{r}) = \psi(z)\exp\left(\mathrm{i}k_x x + \mathrm{i}k_y y\right), \tag{7.4}$$

where $\psi(z)$ satisfies the Bloch condition for some k_z

$$\psi(z+D) = \exp\left(\mathrm{i}k_z D\right)\psi(z), \tag{7.5}$$

where $D = a + b$. The Brillouin zone is infinite in the x and y directions, and $2\pi/D$ wide in z (k_z) direction. Here, we normalize the wave function Ψ as

$$\Omega^{-1} \int |\Psi(\mathbf{r})|^2 \, \mathrm{d}^3 r = 1, \tag{7.6}$$

where Ω is the volume of a normalization box. The solution of $\psi(z)$ is a linear combination of $\exp(\pm \mathrm{i} k_L z)$, where k_L on the Fermi surface is defined in the well as

$$k_L = \left[\frac{2m_d}{\hbar^2} (E_\mathrm{F} - U_\mathrm{w}) - {k_r}^2 \right]^{1/2} \equiv K, \tag{7.7}$$

and in the barrier as

$$k_L = \left[\frac{2m_d}{\hbar^2} (E_\mathrm{F} - U_\mathrm{b}) - {k_r}^2 \right]^{1/2} \equiv \mathrm{i}Q, \tag{7.8}$$

where $k_r = \left({k_x}^2 + {k_y}^2 \right)^{1/2}$ and m_d is the effective mass of the d states. From Eq. (7.5) and the boundary conditions where ψ and $\mathrm{d}\psi/\mathrm{d}z$ are continuous, we obtain

$$\frac{e^{Qb}}{2} \left[\frac{Q^2 - K^2}{2QK} \sin(Ka) + \cos(Ka) \right] = \cos(k_z D). \tag{7.9}$$

In this study, we consider a case in which the barrier height is large enough to satisfy $e^{Qb} \gg 1$. In this case, the minority-spin d states are confined to the magnetic layers and have eigenstates quantized to the thickness of magnetic layers. Therefore, the Fermi surface becomes a set of cylinders (subbands) parallel to the z (or k_z) direction.

7.4 Calculation of resistivity

Resistivities are calculated by the relaxation time approximation of the Boltzmann equation. Since we neglect the shift of the Fermi surface for the d

states, the relaxation time $\tau_\sigma(\mathbf{k})$ ($\sigma = \uparrow,\ \downarrow$) is given as [13, 14, 17]

$$\frac{1}{\tau_\sigma(\mathbf{k})} = \frac{1}{\tau_\sigma^{ss}(\mathbf{k})} + \frac{1}{\tau_\sigma^{sd}(\mathbf{k})}, \tag{7.10}$$

$$\frac{1}{\tau_\sigma^{ss}(\mathbf{k})} = \int \left(1 - \frac{\mathbf{k}\cdot\mathbf{k}'}{k^2}\right) P(\mathbf{k}'s\sigma, \mathbf{k}s\sigma)\mathrm{d}^3k', \tag{7.11}$$

$$\frac{1}{\tau_\sigma^{sd}(\mathbf{k})} = \int P(\mathbf{k}'d\sigma, \mathbf{k}s\sigma)\mathrm{d}^3k', \tag{7.12}$$

where $P(\mathbf{k}'i, \mathbf{k}j)$ is the scattering rate between states $(\mathbf{k}'i)$ and $(\mathbf{k}j)$, i and j stand for $s\uparrow$, $s\downarrow$, $d\uparrow$ and $d\downarrow$. The first term in Eq. (7.10) comes from s–s scattering, and the second from s–d scattering. For simplicity, we assume here that the bulk scatterers with the potential strength $V_0 = V_\mathrm{B}$ distribute in the superlattices with uniform volume density of η_B. In addition, we assume that the interfacial scatterers with the potential strength $V_0 = V_\mathrm{I}$ distribute within the region of $z = z_i \pm \varepsilon$ with the uniform volume density of η_I, where z_i is the position of the ith interface. Here, we do not assume any spin dependence in V_B and V_I as in [12] and [13, 14].

7.4.1 s–s scattering

Since the wave function of the s state is a plane wave, it is easy to calculate the rate of s–s scattering. Using Fermi's golden rule, the scattering rate is given as [16]

$$P(\mathbf{k}'s\sigma, \mathbf{k}s\sigma)\mathrm{d}^3k' = \frac{2\pi}{\hbar}\left({V_\mathrm{B}}^2\eta_\mathrm{B} + n_\mathrm{I}^{ss}\frac{2\varepsilon}{D}{V_\mathrm{I}}^2\eta_\mathrm{I}\right)\mathrm{d}N(E_\mathrm{F}), \tag{7.13}$$

where n_I^{ss} is the number of interfaces in a period of superlattice potential and $\mathrm{d}N(E_\mathrm{F})$ denotes the number of states per unit volume and unit energy at E_F in the volume element d^3k' near $\mathbf{k}'$. Integrating Eq. (7.13), we obtain

the relaxation time due to s–s scattering as

$$\frac{1}{\tau_\sigma^{ss}} = \frac{2\pi}{\hbar} g_s(E_\mathrm{F}) \left({V_\mathrm{B}}^2 \eta_\mathrm{B} + n_\mathrm{I}^{ss} \frac{2\varepsilon}{D} {V_\mathrm{I}}^2 \eta_\mathrm{I} \right), \tag{7.14}$$

$$g_s(E_\mathrm{F}) = \frac{m_s k_\mathrm{F}^s}{2\pi^2 \hbar^2}, \tag{7.15}$$

where m_s and k_F^s are the effective mass and the Fermi wave number of s electrons. The first term in the parentheses of Eq. (7.14) comes from the bulk scattering, while the second term is due to the interfacial scattering.

7.4.2 s–d scattering

The scattering rate of s–d scattering is written as

$$P(\mathbf{k}'d\sigma, \mathbf{k}s\sigma)\mathrm{d}^3k' = \frac{2\pi}{\hbar} \left({V_\mathrm{B}}^2 \eta_\mathrm{B} + \sum_i \frac{2\varepsilon |\psi_{\mathbf{k}'}(z_i)|^2}{D} {V_\mathrm{I}}^2 \eta_\mathrm{I} \right) \mathrm{d}N(E_\mathrm{F}), \tag{7.16}$$

when $\varepsilon \ll 2\pi/k'$. The summation in Eq. (7.16) is taken over the interfaces in a period of the superlattice potential. In the case of $Qb \gg 1$, d states are confined in the well layers, so the amplitude of $\psi_{\mathbf{k}'}(z)$ has a non-zero value in the well layers and near the interfaces between the well and the barrier layers. Thus, it is enough to take the summation in Eq. (7.16) over the well-barrier interfaces. From the analogy with the simple quantum well problem, $|\psi_{\mathbf{k}'}(z_i)|^2$ has the same value at the interfaces as at both edges of the well layers. Hence, Eq. (7.16) is written with the number of the well-barrier interfaces in a period n_I^{sd} as

$$P(\mathbf{k}'d\sigma, \mathbf{k}s\sigma)\mathrm{d}^3k' = \frac{2\pi}{\hbar} \left({V_\mathrm{B}}^2 \eta_\mathrm{B} + n_\mathrm{I}^{sd} \frac{2\varepsilon |\psi_{\mathbf{k}'}(z_\mathrm{I})|^2}{D} {V_\mathrm{I}}^2 \eta_\mathrm{I} \right) \mathrm{d}N(E_\mathrm{F}), \tag{7.17}$$

where z_I is the position of one of the interfaces causing non-zero s–d scattering. As mentioned in the previous section, allowed-wave-number vectors

$\mathbf{k}'$ are discrete. In each subband, the value of k'_r and the wave function are constant, since $Qb \gg 1$. Thus, we obtain

$$\mathrm{d}N(E_\mathrm{F}) = \frac{m_d}{(2\pi\hbar)^2}\mathrm{d}k'_z, \tag{7.18}$$

for each subband, where dk'_z is a length increment along the Fermi surface in the z direction. Integrating Eq. (7.17) using Eq. (7.18), the relaxation time due to s–d scattering is given with the k'_r in the jth subband $k'^{\,j}_r$ as

$$\frac{1}{\tau^{sd}_\sigma} = \frac{2\pi}{\hbar} g_d(E_\mathrm{F}) \frac{a}{D} \left({V_\mathrm{B}}^2 \eta_\mathrm{B} + n_\mathrm{I}^{sd} \frac{2\varepsilon\phi}{D} {V_\mathrm{I}}^2 \eta_\mathrm{I} \right), \tag{7.19}$$

$$\phi = \frac{1}{n_d} \sum_{j=1}^{n_d} \left| \psi_{k'^{\,j}_r}(z_\mathrm{I}) \right|^2, \tag{7.20}$$

$$g_d(E_\mathrm{F}) = \frac{m_d n_d}{2\pi\hbar^2 a}, \tag{7.21}$$

where n_d is the number of d subbands. The first term in the parentheses of Eq. (7.19) comes from the bulk scattering, while the second term is due to the interfacial scattering. Since the relaxation time due to both s–s and s–d scattering [Eqs. (7.14) and (7.19)] is independent of $\mathbf{k}$, the resistivity is written with the density of s electrons N_s as

$$\begin{aligned} \rho_\sigma = \quad & \frac{2\pi m_s}{\hbar N_s e^2} \left\{ g_s(E_\mathrm{F}) \left({V_\mathrm{B}}^2 \eta_\mathrm{B} + n_\mathrm{I}^{ss} \frac{2\varepsilon}{D} {V_\mathrm{I}}^2 \eta_\mathrm{I} \right) \right. \\ & \left. + g_d(E_\mathrm{F}) \frac{a}{D} \left({V_\mathrm{B}}^2 \eta_\mathrm{B} + n_\mathrm{I}^{sd} \frac{2\varepsilon\phi}{D} {V_\mathrm{I}}^2 \eta_\mathrm{I} \right) \right\}. \end{aligned} \tag{7.22}$$

Equation (7.15) indicates that $g_s(E_\mathrm{F})$ is the DOS of the s states per spin at the Fermi energy for the bulk. On the other hand, $g_d(E_\mathrm{F})$ depends on n_d due to the quantum size effect. When the barrier height U_b is large enough, n_d is approximated by the maximum integer satisfying $n_d \leq (a/\pi) \left[2m_d(E_\mathrm{F} - U_\mathrm{w})/\hbar^2 \right]^{1/2}$. If we neglect the discreteness in n_d, $g_d(E_\mathrm{F})$

is identical with the DOS of the d states at the Fermi energy for the bulk ferromagnetic metals. In this case, Eq. (7.22) has the same form as the resistor network theory except for the terms due to the interfacial scattering. The interfacial scattering depends on the number of the scattering centers ($2\varepsilon\eta_{\rm I}$), the strength of the scattering potential ($V_{\rm I}$) and the amplitude of the wave function of the d state at interfaces ($|\psi_{\mathbf{k}}(z_{\rm I})|^2$). The first one corresponds to the magnitude of the interfacial roughness, and the last one corresponds to interfacial electronic state. Therefore, our model includes not only the interfacial roughness but also the interfacial electronic states.

7.5 GMR

In this section, we calculate the GMR using Eq. (7.22). The parameters dependent on the spin and magnetic configuration are D, $n_{\rm I}^{ss}$, $n_{\rm I}^{sd}$ and ϕ. Defining the superlattice period as $\lambda = t_{\rm M} + t_{\rm NM}$, the value of D for the F state is λ and that for the AF state is 2λ. According to this, the value of $n_{\rm I}^{ss}$ for the F state is 2, and that for the AF state is 4. The values of $n_{\rm I}^{sd}$ for the down-spin electrons for the F state and for the up- and down-spin electrons for the AF state are 2, while $n_{\rm I}^{sd} = 0$ for up-spin electrons for the F state. Since the normalization condition depends on the superlattice period (see Eq. (7.6)), ϕ for the AF state is two times larger than that for the F state. Thus, $\phi = 2\phi_{\rm F}$ for the AF state, where $\phi_{\rm F}$ is the ϕ for the F state. The number of the subbands n_d is constant, unless the thickness of the magnetic layers changes. With these parameters, we obtain the expressions for the

spin-dependent resistivities for the F state $\rho_\sigma^{\rm F}$ as

$$\rho_\uparrow^{\rm F} = \frac{2\pi m_s}{\hbar N_s e^2}\left[g_s(E_{\rm F})\left({V_{\rm B}}^2\eta_{\rm B} + \frac{4\varepsilon}{\lambda}{V_{\rm I}}^2\eta_{\rm I}\right)\right], \tag{7.23}$$

$$\begin{aligned}\rho_\downarrow^{\rm F} = \quad & \frac{2\pi m_s}{\hbar N_s e^2}\left[g_s(E_{\rm F})\left({V_{\rm B}}^2\eta_{\rm B} + \frac{4\varepsilon}{\lambda}{V_{\rm I}}^2\eta_{\rm I}\right)\right. \\ & \left. + g_d(E_{\rm F})\frac{t_{\rm M}}{\lambda}\left({V_{\rm B}}^2\eta_{\rm B} + \frac{4\varepsilon\phi_{\rm F}}{\lambda}{V_{\rm I}}^2\eta_{\rm I}\right)\right],\end{aligned} \tag{7.24}$$

and the resistivities for the AF state $\rho_\sigma^{\rm AF}$ as

$$\begin{aligned}\rho_\uparrow^{\rm AF} &= \rho_\downarrow^{\rm AF} \\ &= \frac{2\pi m_s}{\hbar N_s e^2}\left[g_s(E_{\rm F})\left({V_{\rm B}}^2\eta_{\rm B} + \frac{4\varepsilon}{\lambda}{V_{\rm I}}^2\eta_{\rm I}\right)\right. \\ &\quad \left. + g_d(E_{\rm F})\frac{t_{\rm M}}{2\lambda}\left({V_{\rm B}}^2\eta_{\rm B} + \frac{4\varepsilon\phi_{\rm F}}{\lambda}{V_{\rm I}}^2\eta_{\rm I}\right)\right].\end{aligned} \tag{7.25}$$

Although the GMR can be calculated numerically assuming the appropriate superlattice potentials, here we discuss the GMR phenomenologically, treating $g_d(E_{\rm F})$ and $\phi_{\rm F}$ as independent parameters for better transparency in the physics. Figure 7.2 shows the calculated MR ratio with respect to 2ε and $\phi_{\rm F}$. We assume here that $t_{\rm M} = 1$ nm, $t_{\rm NM} = 2$ nm, $g_d(E_{\rm F})/g_s(E_{\rm F}) = 12$ and ${V_{\rm I}}^2\eta_{\rm I}/{V_{\rm B}}^2\eta_{\rm B} = 5$. These values are suitable for explaining the experimental results for Co/Cu superlattices, as we mention in the next section. A considerable MR ratio is obtained even without the interfacial scattering ($2\varepsilon = 0$ nm) because of the strong spin dependence in the DOS of the d states. The MR ratio decreases with increasing 2ε for $\phi_{\rm F} \leqslant 1$, while it increases with increasing 2ε for $\phi_{\rm F} \geqslant 1$. This tendency remains unchanged if we use different values for the layer thicknesses, the ratios of the DOS and the interfacial to bulk scattering. Thus, the relationship between the MR

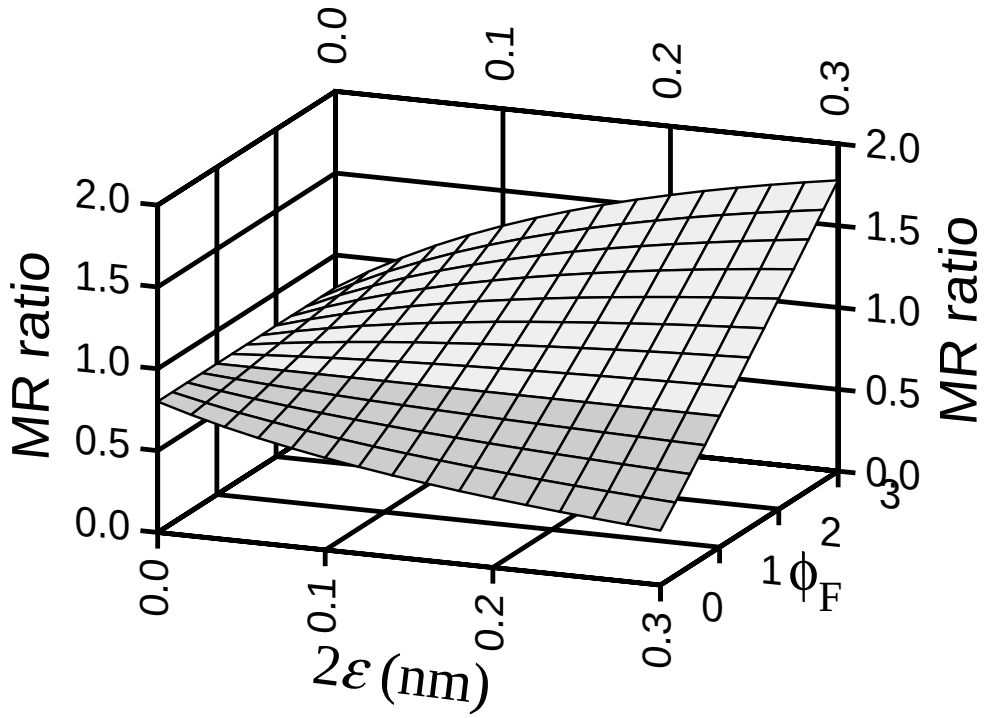

Fig. 7.2: Calculated MR ratio with respect to 2ε and $\phi_{\rm F}$. The parameters are assumed to be $t_{\rm M} = 1$ nm, $t_{\rm NM} = 2$ nm, $g_d(E_{\rm F})/g_s(E_{\rm F}) = 12$ and ${V_{\rm I}}^2\eta_{\rm I}/{V_{\rm B}}^2\eta_{\rm B} = 5$. The regions of $\phi_{\rm F} < 1$ and $\phi_{\rm F} > 1$ are indicated by the different tones.

ratio and the interfacial roughness strongly depends on $\phi_{\rm F}$. In other words, the GMR in superlattices with interfacial roughness strongly depends on the amplitude of the wave function of the d state at interfaces. In the next section, we estimate the magnitude of $\phi_{\rm F}$ for Co/Cu superlattices by comparing our calculation with experiments.

7.6 Interfacial scattering in Co/Cu

We have reported the structure and the GMR properties of Co/Cu superlattices with artificially mixed interfaces in Chapters 4–6 [6,7,21]. The interfaces in Co/Cu have been modified by codeposition. The Co and Cu atoms are mixing randomly in the interfacial regions, which increases with increasing nominal thickness of the codeposited region $t_{\rm mix}$.

The resistivity of these samples decreases from the initial value at zero field with increasing magnetic field, and saturates at the value of $\rho_{\rm s}(=\rho_{\rm F})$ in a field larger than the saturation field. After saturation, the resistivity has a peak near the coercive field. Since the value of the initial resistivity is larger than that of the peak one, the AF alignment of the magnetization of the Co layers is closer to perfection in the initial state than that in the field where the resistivity has the peak. The magnetization of all samples is zero in initial state, and the relationship between the resistivity and the square of the magnetization is linear at low temperatures. From the discussion in Chapter 6, this indicates that magnetic configuration of our samples is very close to the perfect AF alignment at the initial state. Therefore we denote the resistivity in the initial states as $\rho_{\rm AF}$ here. Furthermore, linear dependence of the resistivity on the square of the magnetization precludes the strong spin dependence of the scattering potential for both bulk and interfacial scattering.

Figure 7.3 shows the $t_{\rm mix}$ dependence of the GMR measured at 5 K for $[{\rm Co(1.0nm)/Cu(2.2nm)}]_{16}$. Data are taken from Chapter 6 [7]. Both $\rho_{\rm AF}$ and $\rho_{\rm F}$ increase with increasing $t_{\rm mix}$, while the MR ratio decreases. It is clear that the interfacial scattering is crucial but less spin dependent.

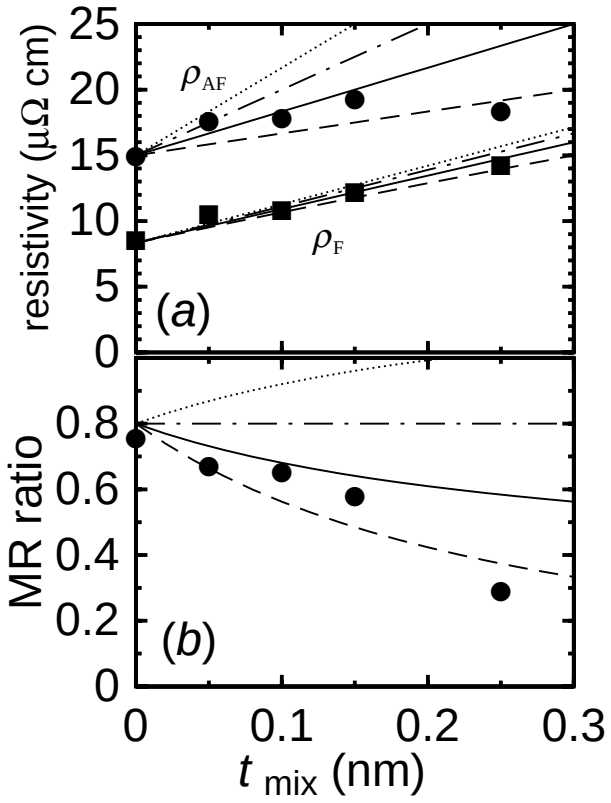

Fig. 7.3: The measured (symbols) and calculated (lines) resistivities (a) and MR ratios (b). Measurement was performed at 5K on [Co(1.0 nm)/Cu(2.2 nm)]$_{16}$ with artificially mixed interfacial regions of thickness $t_{\rm mix}$. In (a), the measured $\rho_{\rm AF}$ (•) and $\rho_{\rm F}$ (■) correspond to the resistivities for antiferromagnetic and ferromagnetic configurations, respectively. Data are taken from Chapter 6. Parameters used in the calculation are $t_{\rm M} = 1$ nm, $t_{\rm NM} = 2.2$ nm, $g_d(E_{\rm F})/g_s(E_{\rm F}) = 12$ and ${V_{\rm I}}^2\eta_{\rm I}/{V_{\rm B}}^2\eta_{\rm B} = 5$. The lines indicate the results for $\phi_{\rm F} = 0$ (dashed lines), $\phi_{\rm F} = 0.5$ (solid lines), $\phi_{\rm F} = 1.0$ (dashed and dotted lines) and $\phi_{\rm F} = 1.5$ (dotted lines).

Despite the large difference in the resistivities at low temperature, no significant differences in the temperature dependence of the GMR between the samples with different $t_{\rm mix}$ have been observed (see Figs. 6.3–6.6). For all samples, $\rho_{\rm F}$ closely approximates a T^2 power law, while $\rho_{\rm AF} - \rho_{\rm F}$ changes linearly with $T^{3/2}$. The difference between the temperature coefficients of the samples of $t_{\rm mix} \leqslant 0.15$ nm is small. This indicates that the interfacial scattering can be attributed to the impurity or defect scattering.

Although the mean free path roughly estimated for the maximum resistivity in Fig. 7.3 ($\approx 20\mu\Omega$ cm) is about 4.0 nm, Edwards *et al.* [12] indicated that the limit of long mean free path is already reached rapidly for a mean free path comparable with the superlattice period. Therefore, it is appropriate to adopt the present model for interpreting the $t_{\rm mix}$ dependence of the GMR at 5 K. We can estimate the value of $g_d(E_{\rm F})/g_s(E_{\rm F})$ at about 12 from the measured MR ratio of the sample of $t_{\rm mix} = 0$ nm, if we neglect the interfacial scattering [assuming $\varepsilon = 0$ nm in equations (7.23)–(7.25)]. This value of $g_d(E_{\rm F})/g_s(E_{\rm F})$ is close to the ratio of the calculated DOS at $E_{\rm F}$ in the majority- and minority-spin bands in bulk Co [18,19]. The calculated resistivities and the MR ratio for the parameters of $t_{\rm M} = 1$ nm, $t_{\rm NM} = 2.2$ nm, $g_d(E_{\rm F})/g_s(E_{\rm F}) = 12$ and ${V_{\rm I}}^2\eta_{\rm I}/{V_{\rm B}}^2\eta_{\rm B} = 5$ are also indicated by lines in Fig. 7.3, where we assume that $t_{\rm mix} = 2\varepsilon$. The calculated results are normalized at $t_{\rm mix} = 0$ so as to make the calculated $\rho_{\rm F}$ equal to the measured one. It is clear that the behavior of $\rho_{\rm F}$ is insensitive to $\phi_{\rm F}$. The agreement between measured and calculated $\rho_{\rm F}$ is good when ${V_{\rm I}}^2\eta_{\rm I}/{V_{\rm B}}^2\eta_{\rm B} = 5.0 \pm 1.0$. It is reasonable that the density of the scattering centers is larger, or the scattering potential is stronger at interfaces than in the bulk ($\eta_{\rm I} > \eta_{\rm B}$ or $V_{\rm I} > V_{\rm B}$).

On the other hand, ρ_{AF} is sensitive to ϕ_{F}. Comparing the measured and the calculated results, $\phi_{\mathrm{F}} \simeq 0.5$ is suitable for explaining the behavior of ρ_{AF} and the MR ratio for the samples for which $t_{\mathrm{mix}} \leqslant 0.15$ nm. The approximation of $\varepsilon \ll 2\pi/k'$ in Eq. (7.16) will no longer hold when t_{mix} becomes comparable with the period of $|\psi_{\mathbf{k}}(z)|^2$. This affect ρ_{AF} much more than it does ρ_{F}, and may cause the deviation between the measured and calculated ρ_{AF} at $t_{\mathrm{mix}} = 0.25$ nm. Detailed numerical calculation will be necessary to study the GMR for the samples with such large roughness. The value of $\phi_{\mathrm{F}} < 1$ indicates that amplitude of the d states is attenuated at interfaces, since the average value of $|\psi_{\mathbf{k}}(z)|^2$ is about λ/t_{M} (> 1) in the magnetic layers. Thus, d states are strongly bound in magnetic layers.

Our model agrees well with the experimental results. However, the contribution of the interfacial scattering to the resistivity of the sample with $t_{\mathrm{mix}} = 0$ nm remains unclear, although we neglect it in the above discussion. In fact, we have confirmed the existence of a small amount of interfacial mixing for the sample with $t_{\mathrm{mix}} = 0$ nm (see Chapter 4 and reference [21]). The influence of the interfacial mixing can also be discussed by the layer thickness dependence of the resistivities. Thus, we focus our attention on the dependence of ρ_{F} (which is not influenced by the interlayer coupling between adjacent Co layers) on the thickness of the Co and Cu layers for samples without intentionally mixed interfaces. As a result, ρ_{F} increases with increasing Co layer thickness, while it decreases with increasing Cu layer thickness. This indicates clearly that the resistivity of Co layers is larger than that of not only Cu layers but also the interfaces. This layer thickness dependence is reproduced only when ε is very small in Eqs. (7.23) and (7.24). Therefore,

our assumption of $\varepsilon = 0$ for the sample with $t_{\rm mix} = 0$ nm is appropriate.

If superlattices have slightly rougher interfaces than those of our samples with $t_{\rm mix} = 0$ nm, the interfacial scattering will influence the GMR significantly depending on the interfacial electronic state. The interfacial electronic state should be sensitive to the combination of metals. Parkin [11] has reported that the MR ratio is enhanced by inserting very thin Co layers at the interfaces between Cu and NiFe layers. This can be interpreted in our model as the change in $\phi_{\rm F}$ depending on materials. The virtual bound state indicated by Inoue and Maekawa [22] may also affect the magnitude of the GMR. However, the bulk s–d scattering will be the most important process giving rise to the GMR in M/Cu superlattices, since a very large MR ratio is observed, at least for our sample whose interfacial scattering is very small.

Consequently, the GMR in Co/Cu superlattices mainly comes from the spin-dependent bulk scattering due to spin-dependent DOS in the Co layers. The interfacial scattering due to interfacial roughness is less spin dependent than the bulk scattering. This is understood in terms of the d states bound in the Co layers.

7.7 Conclusion

We have extended the resistor network theory to include the interfacial scattering explicitly and discussed the role of bound d state in the CIP MR. The interfacial states are described in our model with the number of interfacial scattering centers ($2\varepsilon\eta_{\rm I}$), the height of the scattering potentials ($V_{\rm I}$) and the amplitude of the wave function of the d states ($|\psi_{\mathbf{k}}(z_{\rm I})|^2$). The first is concerned with the interfacial roughness, and the last corresponds to the

interfacial electronic state. Our model is consistent with the experiments for Co/Cu superlattices with artificially mixed interfaces, when we assume that the minority spin d states are strongly bound in Co layers. Therefore, the GMR in Co/Cu superlattices mainly comes from the spin-dependent s–d scattering in the Co layers, and the interfacial scattering is less spin-dependent than bulk scattering. This is because of the attenuation of the wave function of d states at interfaces.

References

[1] M. N. Baibich, J. M. Broto, A. Fert, F. Nguyen Van Dau, F. Petroff, P. Etienne, G. Creuzet, A. Friederich, and J. Chazelas, Phys. Rev. Lett. **61**, 2472 (1988).

[2] S. S. P. Parkin, R. Bhadra, and K. P. Roche, Phys. Rev. Lett. **66**, 2152 (1991).

[3] D. H. Mosca, F. Petroff, A. Fert, P. A. Schroeder, W. P. Pratt Jr., and R. Laloee, J. Magn. Magn. Mater. **94**, L1 (1991).

[4] A. E. Berkowitz, J. R. Mitchell, M. J. Carey, A. P. Young, S. Zhang, F. E. Spada, F. T. Parker, A. Hutten, and G. Thomas, Phys. Rev. Lett. **68**, 3745 (1992).

[5] J. Q. Xiao, J. Samuel, and L. Chien, Phys. Rev. Lett. **68**, 3749 (1992).

[6] M. Suzuki and Y. Taga, J. Appl. Phys. **74**, 4660 (1993).

[7] M. Suzuki and Y. Taga, Phys. Rev. B **52**, 361 (1995).

[8] V. S. Speriosu, J. P. Nozieres, B. A. Gurney, B. Dieny, T. C. Huang, and H. Lefakis, Phys. Rev. B **47**, 11579 (1993).

[9] M. J. Hall, B. J. Hickey, M. A. Howson, C. Hammond, M. J. Walker, D. G. Wright, D. Greig, and N. Wiser, J. Phys. Condens. Mater. **4**, L495 (1992).

[10] T. Thomson, P. C. Riedi, and D. Greig, Phys. Rev. B **50**, 10319 (1994).

[11] S. S. P. Parkin, Phys. Rev. Lett. **71**, 1641 (1993).

[12] D. M. Edwards, J. Mathon, and R. B. Muniz, IEEE Trans. Magn. **27**, 3548 (1991).

[13] L. Xing and Y. C. Chang, Phys. Rev. B **48**, 4156 (1993).

[14] L. Xing, Y. C. Chang, M. B. Salamon, D. M. Frenkel, J. Shi, and J. P. Lu, Phys. Rev. B **48**, 6728 (1993).

[15] K. M. Schep, P. J. Kelly, and G. E. W. Bauer, Phys. Rev. Lett. **74**, 586 (1995).

[16] P. B. Visscher, Phys. Rev. B **49**, 3907 (1994).

[17] A. Fert and I. A. Campbell, J. Phys. C **6**, 849 (1976).

[18] R. A. Ballinger and C. A. W. Marshall, J. Phys. F **3**, 735 (1973).

[19] M. Mehta-Ajmani, I. P. Batra, E. E. Lafon, and C. S. Fadley, J. Phys. C **13**, 2807 (1980).

[20] S. Zhang and P. M. Levy, in *Mat. Res. Soc. Symp. Proc.*, Vol. 313, p. 53.

[21] M. Suzuki, Y. Taga, A. Goto, and H. Yasuoka, Phys. Rev. B **50**, 18580 (1994).

[22] J. Inoue and S. Maekawa, J. Phys. Soc. Jpn. **61**, 1149 (1992).

Chapter 8

GMR sensors using Co/Cu superlattices

Abstract

We have demonstrated the usefulness of giant magnetoresistance (GMR) in Co/Cu superlattices for practical application to the magnetic rotation sensor. Optimized Co/Cu superlattices have been fabricated into sensors with appropriate passivation layers. The sensor output changes more than 20%, synchronizing the rotation of the magnet rotor. It is remarkable that there is no significant degradation of the GMR sensors even after they are left in the atmosphere of the air at 150 °C for 1000 h. This confirms the high reliability of the GMR sensors and promises that they can be used in automobiles and aircraft under sever conditions.

8.1 Introduction

Giant magnetoresistance (GMR), first found in magnetic superlattices [1–3], has attracted much attention from both fundamental and practical standpoints. For a large change in the resistance, antiferromagnetic (AF) alignment of the magnetization of adjacent magnetic layers is essential. In superlattices with GMR, the AF alignment is realized by means of AF exchange coupling through the nonmagnetic layers. Since the AF coupling is rather strong, it is difficult to improve the sensitivity of the GMR to the magnetic field, despite its large magnetoresistance (MR) ratio. In order to overcome this difficulty, an uncoupled magnetic sandwich structure, the so-called spin valve, has been proposed [4–7]. In the spin valve structure, the magnetization of magnetic layers is aligned antiferromagnetically by pinning the magnetization of one of the ferromagnetic layers using the exchange-biasing layer. Since the spin valve shows an MR ratio of more than 5% in a few Oe, this device is expected to find the application to the MR head, MR memory, etc. Therefore, most of the recent industrial interest is focused on the application of spin valve GMR for high density data storage.

On the other hand, various commercial MR sensors using conventional MR such as NiFe and NiCo are available on the market. These sensors are used practically in rotation, angular and position sensing. For certain uses, it has been required to enlarge the sensor output rather than enhance the sensitivity to the magnetic field. In such cases, conventional MR sensors can be replaced by GMR sensors of the superlattice type (not spin valve) from the following points of view. (1) Generally, superlattice GMR sensors can produce a larger signal than spin valve and conventional MR sensors. (2)

They are strongly resistant to electromagnetic interference; this is consistent with the low sensitivity of the superlattice GMR to the magnetic field. (3) The preparation of the superlattices is easier than that of spin valve, resulting in high production throughput. Therefore, GMR superlattice sensors have many advantages for application to rotation, angular and position sensing in such as automobiles and aircraft.

However, there has been a prejudice that superlattices may not be durable enough to be used under such sever conditions. In fact, it has been reported that the MR ratio of Co/Cu superlattices is decreased significantly by annealing at a temperature of 250–300 °C [8], while it is not changed by annealing at 150 °C [9]. In these studies, Co/Cu superlattices were annealed in the high vacuum for only a few hours. Contrary to this, for practical sensors, durability for a much longer period in air is required. Up to now, there have been no reports on the thermal durability of superlattices in air for a long period.

The purpose of this chapter is to clarify the usefulness of the GMR superlattice sensors for the practical application to the rotation sensors. We focused our attention on Co/Cu superlattices and refined their GMR properties. Furthermore, we fabricated simple GMR sensors and evaluated the performance and their durability in air.

8.2 Experiments

The Co/Cu superlattices were deposited on surface-oxidized Si substrates in a magnetron sputtering system with a base pressure of 2×10^{-7} Torr. After deposition of a buffer layer, 16–24 Co/Cu bilayers were grown at room tem-

perature in an Ar pressure of 3×10^{-3} Torr at a deposition rate of $0.2 - 0.3$ nm/s.

As described in Chapter 3, we optimized the GMR properties in Co/Cu superlattices for the application to the sensors by changing the combination of the layer thicknesses of Co and Cu. Moreover, the crystallographic orientation and interfacial roughness are controlled by changing the thickness and the substance of the buffer layer to archive a large MR ratio and a small saturation field.

Using the optimized Co/Cu superlattices with a structure of NiFe(5.0 nm)/Cu(2.1 nm)/[Co(1.0 nm)/Cu(2.1 nm)/]$_{16}$, we fabricated the magnetic field sensors. The structure of the GMR sensors is shown in Fig. 8.1. Since the MR ratio of Co/Cu superlattices ($\sim$ 20%) is much larger than that of conventional MR in such as NiFe or NiCo ($\sim$ 3%), and the resistivity of Co/Cu superlattices is comparable with that of NiFe and NiCo, the structure of the GMR sensor element can be very much simpler. In this work, we fabricated a sensing element of 45 μm width and 4.2 mm length in an area of $3 \times 5\text{mm}^2$. To locate the sensing element close to the magnet, element was patterned at 300 μm from the edge of the sensor chip.

The fabrication process is as follows. After the optimized Co/Cu superlattices are deposited on the surface-oxidized Si wafer, they are patterned by the laser trimming apparatus. The sensing element is insulated from the surrounding superlattice by a laser-trimmed line of width 2 μm. As described in Sec 8.3.3, Co/Cu superlattices are easily oxidized in high temperature air. Moreover, they corrode in water containing ions. We must take care not to expose the bare superlattice to high temperature air or to water during the

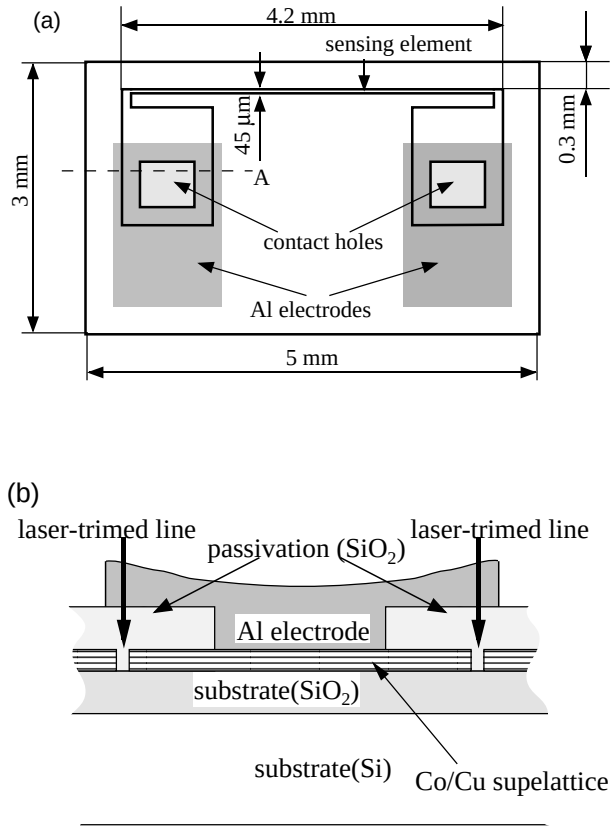

Fig. 8.1: Schematic structure of the GMR sensor element. (a) Top view (b) cross-sectional view along the broken line A in (a).

fabrication process. Laser trimming enables us to pattern the superlattice without heating or using water, both of which are necessary for standard photolithography.

On the patterned superlattices, SiO_2 was deposited as a passivation layer by sputtering at room temperature in an Ar pressure of 3×10^{-3} Torr at a deposition rate of 0.3 nm/s up to a thickness of 800 nm. The contact holes are formed by standard photolithography and reactive ion etching (RIE) with

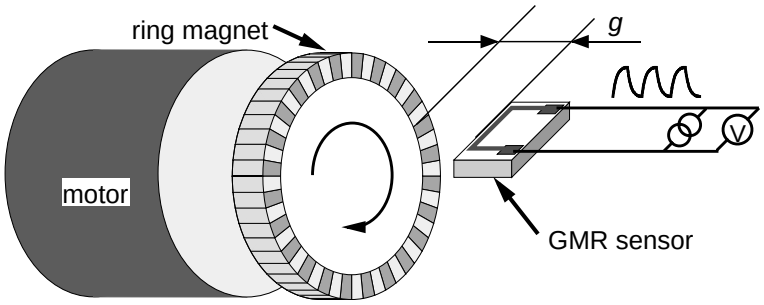

Fig. 8.2: Configuration of the magnetic rotation sensor system using the GMR sensor. The ring magnet with 48 poles is rotated by motor at a rotation speed of 20–2000 rpm.

CF_4 (10 sccm) and O_2 (5 sccm) gases at an RF power of 200 W. Aluminum used as the electrode was deposited by sputtering in an Ar pressure of 3×10^{-3} Torr at a deposition rate of 0.5 nm/s up to a thickness of 1 μm. Patterning of the aluminum was carried out by photolithography and wet etching.

We investigated the MR properties of the GMR sensor in a static magnetic field. Furthermore, its usefulness as a magnetic rotation sensor was demonstrated using a ring-shaped magnet rotor (NEOMAX-P9). The configuration of the simple rotation sensing system is shown in Fig. 8.2. The dimensions of the magnet are 44 mm, 48 mm and 6 mm in inner and outer diameter and thickness, respectively. The number of magnetic poles of the magnet was 48, and the strength of the magnetic field at 1.5 mm from the magnet surface was about 700 Oe. The GMR sensors were operated at a constant current of 5 mA. The air gap between the edge of the sensor chip and the magnet surface was varied. To investigate the response speed of the GMR sensors, the rotation speed of the magnet was varied from 20 rpm to 2000 rpm.

Thermal durability over a long period was also investigated. The bare superlattices and the GMR sensors were left in an oven kept at a constant temperature of 150°C. The atmosphere in the oven was the air. The resistance in zero magnetic field was monitored during the durability test. The MR properties after the durability test were compared with those of virgin samples.

8.3 Results and discussion

8.3.1 Refinement of Co/Cu superlattices

The MR ratio and the saturation field H_s oscillate as a function of the Cu layer thickness and show peaks at Cu layer thicknesses of 0.9 ± 0.05 and 2.1 ± 0.1 nm as shown in Fig 3.1. The MR ratio and H_s at the first peak are 45% and 6 kOe, respectively, whereas they are 33% and 1.0 kOe at the second peak. In this chapter, the MR ratio is defined as

$$\text{MR ratio} = (R_{max} - R_s)/R_s, \tag{8.1}$$

where R_{max} and R_s are maximum and saturation resistance, respectively. On the other hand, as a function of the Co layer thickness, the MR ratio shows a broad peak at a Co layer thickness of around 1.0 nm. Since H_s at the first peak is much larger than that at the second peak, the MR properties at the first peak are not appropriate for the application. Therefore, we focus our attention on the MR properties at the second peak. The optimum structure of the Co/Cu superlattices is as follows: substrate/buffer layer/Cu(2.1 ± 0.1 nm)/[Co(1.0 ± 0.2 nm)/Cu(2.1 ± 0.1 nm)/]$_{16}$.

However, the value of H_s at the second peak for the sample deposited

on the Fe buffer layer of thickness 5.0 nm is still too large for the practical application. As we reported in the previous chapters, the MR properties are closely related to the crystallographic preferred orientation of the Co/Cu superlattice (see Chapter 3 and Ref. [10]), and the interfacial roughness (see Chapters 4–6 and Refs. [11–13]). These can be controlled by changing the thickness and the substance of the buffer layer. As indicated in Table 3.1, the samples with (111) preferred orientation have small H_s and are more appropriate for application than those with (110) preferred orientation. For the samples with (111) orientation, however, the magnitude of the MR ratio varies from 4% to 25% depending strongly on the substance of the buffer layer. The difference in the MR ratio can be attributed to the magnitude of the mesoscopic interfacial roughness. Among the substances we surveyed, NiFe alloy is the best buffer layer, since Co/Cu superlattices deposited on the thin NiFe layer show a large MR ratio (24.5%) and a small H_s ($\sim$ 500 Oe), as indicated in Fig. 8.3(a).

On the basis of these results, we fabricated useful GMR sensors using Cu(2.1 nm)/[Co(1.0 nm)/Cu(2.1 nm)/]$_{16}$ superlattices deposited on the NiFe buffer layer of thickness 5.0 nm. Their properties are discussed in the following sections.

8.3.2 Characteristics of GMR sensors

Figure 8.3(b) shows the MR curves measured in the static magnetic field for the GMR sensors. The values of R_{max} and R_s are 346 Ω and 274 Ω, respectively, and the MR ratio is 26.3%. The resistivities estimated from the dimension of the sensing element are close to the values of the original super-

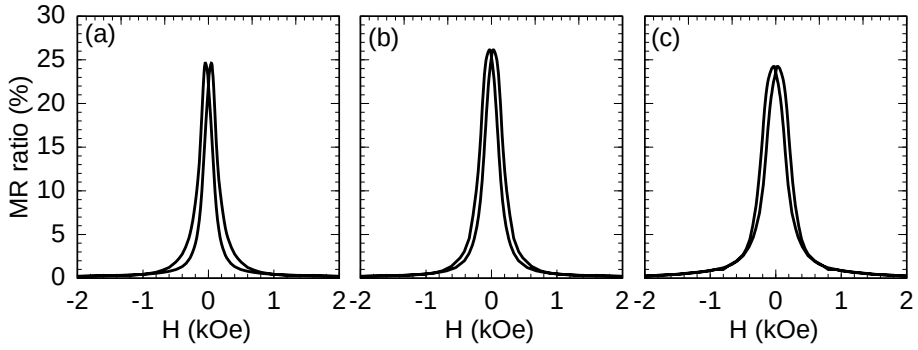

Fig. 8.3: The MR curves measured in the static magnetic field of (a) the optimum Co/Cu superlattice: substrate/NiFe(5.0)/Cu(2.1 nm)/[Co(1.0 nm)/Cu(2.1 nm)]$_{16}$; (b) the initial MR curve of the sensor (Sec. 8.3.2); and (c) the MR curve of the sensor measured after the durability test (Sec. 8.3.3). Sensors were fabricated using the superlattices with the same structure as (a).

lattices. We find small differences in MR properties between the GMR sensors and the original superlattices. These are related to the fact that the Co/Cu superlattices experience the high temperature process of photolithography. During the fabrication of GMR sensors, the Co/Cu superlattices experience the photolithography processes twice, for the patterning of the contact holes and the Al electrodes. In each photolithography process, the superlattices are heated in air up to 90 °C and 120 °C for the pre- and postbaking of the resist, respectively, for 30 min. Nevertheless, the GMR sensors keep their large MR ratio of 26.3% and their H_s are about 500 Oe. The differences in MR ratio and H_s between the GMR sensors and the original superlattices are not significant. It is clear that the MR properties of the GMR sensors are still useful even after fabrication.

As described in Sec. 8.3.3, the MR ratio decreases significantly (to less

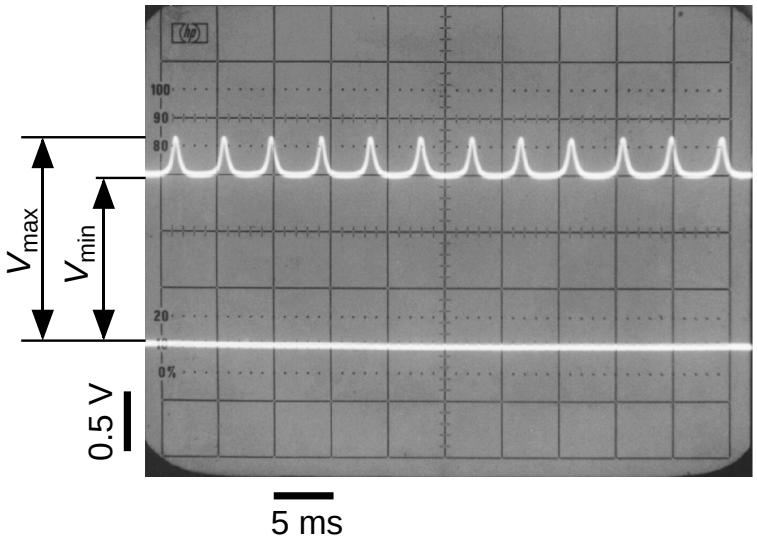

Fig. 8.4: Example of the output waveform from the sensor operated at a constant current of 5 mA. The sensor chip is located at 1 mm from the surface of the ring magnet with 48 magnetic poles.

than 1.0%) after the bare (without any passivation layer) superlattices are heated in air. In the present fabrication processes, however, the Co/Cu superlattices are patterned at room temperature by laser trimming and are passivated before any subsequent high temperature processes. Therefore, the Co/Cu superlattices have not been exposed to high temperature air. This is the key to maintaining the MR ratio and H_s at useful values.

Figure 8.4 shows an example of the output waveform recorded by using the configuration indicated in Fig. 8.2. The GMR sensor is operated at a constant current of 5 mA, and the air gap g is 1 mm. The maximum (V_{max}) and minimum (V_{min}) output voltages are consistent with the values of R_{max} and R_s, respectively. Thus, the maximum variation ratio of the output voltage $\Delta V/V_{min} = (V_{max} - V_{min})/V_{min}$ exceeds 20% and is close to

the MR ratio measured in the static field. It is remarkable that the large ΔV is available when using the very simple sensing element with considerable low resistance ($\sim 300\Omega$). If one expects conventional MR sensors such as NiFe and NiCo to produce ΔV comparable with the present GMR sensor, a sensing element with a resistance of ~ 1.8 kΩ is required because of the small MR ratio of $\sim 3\%$. Thus, the sensing element for conventional MR sensors occupies a 6–10 times larger area than for GMR sensors. In other words, GMR sensors can detect the variation of the magnetic field over a smaller area than conventional MR sensors. As a result, the magnet rotor can be reduced in size, and the number of the magnetic poles can be increased. This leads to a significant improvement of the rotation sensing system, especially in compactness and in capability to detect low rotation speed.

For practical applications, it is important to clarify the response speed and the relation between the sensor output and g. Figure 8.5 shows the relationship between the value of g and the sensor output measured at rotation speeds of 20, 200, 2000 rpm. At $g \leq 2.0$ mm, the value of $\Delta V/V_{\min}$ exceeds 20% at all rotation speeds, whereas it decreases significantly at $g > 2.0$ mm. Figure 8.5(b) indicates that the decrease of $\Delta V/V_{\min}$ is due to increase of $V_{\min}$. The value of $V_{\min}$ almost independent of g at $g \leq 2.0$ mm since the maximum magnetic field applied to the sensing element is large enough to saturate the Co/Cu superlattice. At $g > 2.0$ mm, $V_{\min}$ increases since the maximum applied field weakens with increasing g. As the result, the value of $\Delta V/V_{\min}$ decreases significantly at $g > 2.0$ mm.

For small value of g, the value of $\Delta V/V_{\min}$ measured at a rotation speed of 2000 rpm is smaller than that measured at slower rotation speeds. Since $V_{\min}$

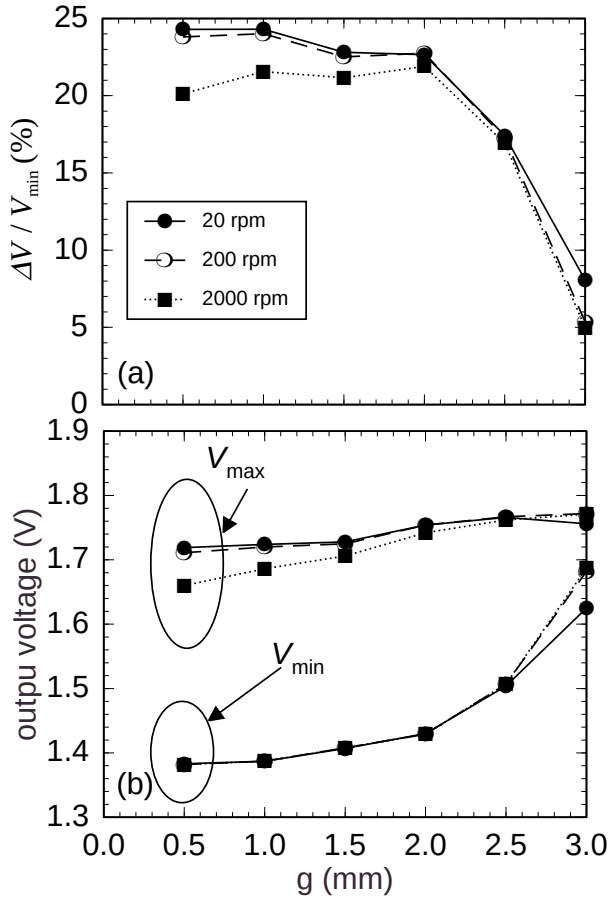

Fig. 8.5: Dependence on the air gap g of (a) the variation ratio of the output voltage, (b) $V_{\max}$ and $V_{\min}$ measured at the rotation speed of the magnet: 20, 200, and 2000 rpm.

is independent of the rotation speed (see Fig. 8.5(b)), the decrease of $\Delta V/V_{\min}$ at 2000 rpm is due to a decrease of $V_{\max}$. This indicates that the some parts of the magnetization of Co layers are reversed simultaneously without aligning antiferromagnetically. In the magnetic field distribution at small g, the region of the small magnetic field will become narrow so that the period when the applied field is small becomes too short to align the magnetization of the Co layers antiferromagnetically. However, $\Delta V/V_{\min}$ is almost independent of the rotation speed at $g = 1.5$ and 2.0 mm. Consequently, the best configuration of our GMR sensors and the ring magnet is obtained at $g = 1.5$–2.0 mm.

Since the GMR sensors are well passivated by the SiO_2 layer, we can measure the temperature dependence of the sensor output in air. Measurements were performed within 24 h in the temperature sequence of: RT $\rightarrow$ 150°C $\rightarrow$ RT $\rightarrow$ -50°C $\rightarrow$ RT $\rightarrow$ 150°C. Figure 8.6 shows the linear temperature dependence of $\Delta V/V_{\min}$; the relationship can be approximated by the following equation:

$$\text{MR ratio}(\%) = -6.44 \times 10^{-2} T(^{\circ}\text{C}) + 25.3 \tag{8.2}$$

The value of $\Delta V/V_{\min}$ is more than 16% even at 150°C, although it decreases with increasing temperature. Clearly, GMR sensors can be used over a wide temperature range if the temperature dependence of the resistance is overcome by using such as AC coupling.

8.3.3 Thermal durability of GMR sensors

To confirm the reliability of the GMR sensors, it is necessary to investigate the thermal durability over a long period. If the actual temperature of use of the GMR sensors is near room temperature, it is meaningful to investigate

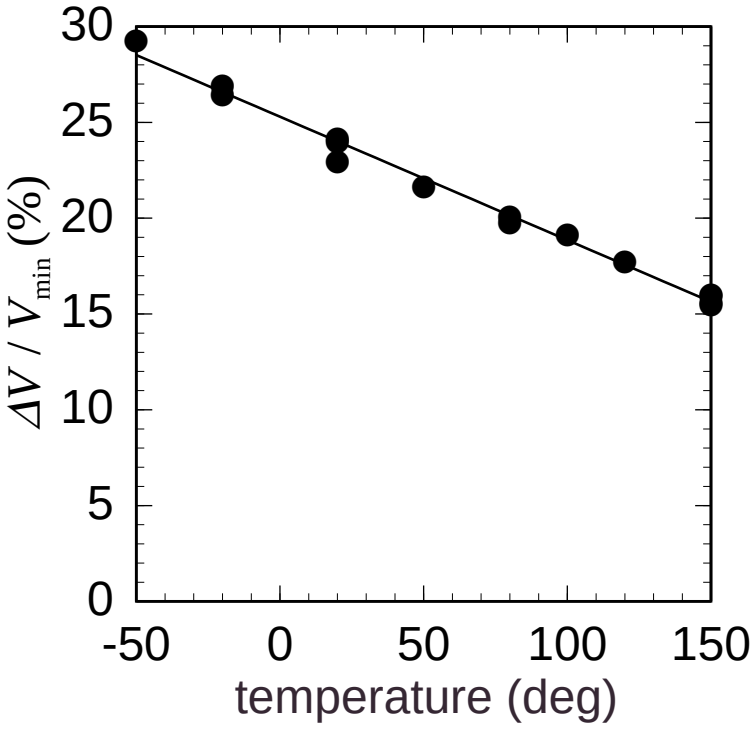

Fig. 8.6: Temperature dependence of the MR ratio of the GMR sensor. The temperature is varied between -50 and 150°C. The line indicates the result of least square fitting to the equation: MR ratio(%) = $-6.44 \times 10^{-2} T(^{\circ}\mathrm{C}) + 25.3$

the durability at high temperature as an accelerated test of the degradation of the GMR near room temperature.

Figure 8.7 shows the variation of the resistance of the bare superlattices and the GMR sensors in zero field in air. The temperature in the oven is raised over 30 min from RT to 150 °C and kept constant for more than 1000 h. In the figure, the resistances are normalized by the values measured at RT.

The resistance of the bare superlattice increases rapidly with the passage

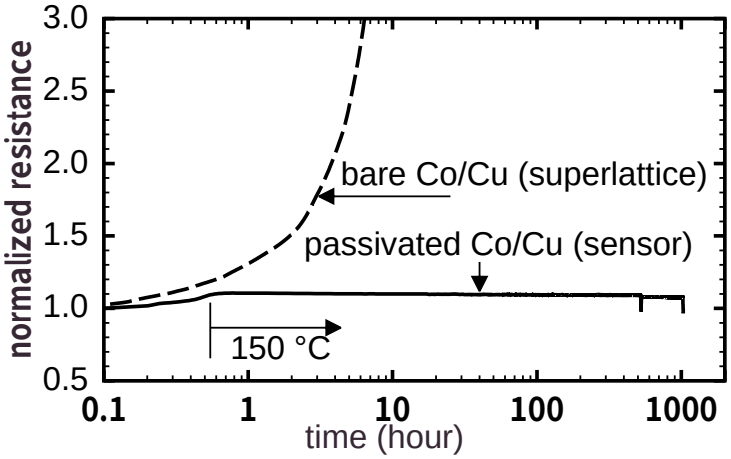

Fig. 8.7: Variation of the resistance of bare superlattices (dashed line) and sensors (solid line) during the durability test at 150 °C in air. After passage of about 500 h, we checked the MR properties of the sensor by using the permanent magnet. Since the magnetization process is irreversible, the step-like changes in the resistance are found at 500 h and are not due to degradation of the sensors.

of time and dose not saturate until 20 h. The resistance at 20 h is 22.2 times larger than the initial value (not plotted in Fig. 8.7). It is difficult to continue the durability test because of the degradation of the electrical contact between the superlattices and the probe. Thus the durability test for the bare superlattice is terminated at 20 h and the MR properties are measured in the static field at RT. The resistance after the durability test does not revert to the initial value and stays at a value of 18.7 times larger. The MR ratio decreases to less than 0.8%. These significant changes in the MR properties are attributed to the oxidation of the Co/Cu superlattice. Therefore, we must take care not to expose the superlattices to high temperature air during the fabrication and use of GMR sensors.

For the GMR sensors, the increase in resistance is confined in the first 30 min. After the passage of about 500 h, we checked the MR properties of the GMR sensors by using the permanent magnet. Since the magnetization process is irreversible, step-like changes in the resistance occur at 500 h and are not due to the degradation of the sensor. Please note the slope of the change in the resistance. Clearly, the resistance is very stable for more than 1000 h. Since the increase in the resistance up to first 30 min is due to the intrinsic temperature dependence of the resistance of the Co/Cu superlattice, the resistance measured after the durability test reverts to a value close to the initial resistance. The difference between R_s measured before and after the durability test is only -2.2% of the initial resistance. The MR curve measured at room temperature after the durability test is shown in Fig 8.3(c). The GMR sensors keep their MR ratio of 24.2% and their H_s of 500 Oe even after the durability test. Although the MR properties change slightly after the durability test, this will not cause significant problems in practical use. This divests us of the prejudice that GMR sensors must be used only in moderate conditions and extends the field of application of GMR sensors.

8.4 Conclusion

We have investigated the GMR in Co/Cu superlattices for the purpose of practical application to magnetic sensors. We find that the superlattices with the structure substrate/NiFe(5.0 nm)/Cu(2.1 nm)/[Co(1.0 nm)/Cu(2.1 nm)/]$_{16}$ shows useful GMR properties.

Using this superlattices, we have fabricated GMR sensors and demonstrated their performance as magnetic rotation sensors. In the appropriate

configuration of the sensor chip and the magnet rotor, the sensor output changes more than 20%, synchronizing the rotation of the magnet, and is almost independent of the rotation speed up to 2000 rpm.

Since the GMR sensors are passivated from the air by an SiO_2 layer, they shows extremely high durability against high temperature air. Even after the sensors are left in the air of 150 °C for 1000 h, the MR ratio of more than 24% and $H_s \approx 500$ Oe are available.

Consequently, GMR sensors using Co/Cu superlattice can be used as magnetic sensors in automobiles and aircraft under severe conditions.

References

[1] M. N. Baibich, J. M. Broto, A. Fert, F. Nguyen Van Dau, F. Petroff, P. Etienne, G. Creuzet, A. Friederich, and J. Chazelas, Phys. Rev. Lett. **61**, 2472 (1988).

[2] S. S. P. Parkin, R. Bhadra, and K. P. Roche, Phys. Rev. Lett. **66**, 2152 (1991).

[3] D. H. Mosca, F. Petroff, A. Fert, P. A. Schroeder, W. P. Pratt Jr., and R. Laloee, J. Magn. Magn. Mater. **94**, L1 (1991).

[4] B. Dieny, V. S. Speriosu, S. S. P. Parkin, B. A. Gurney, D. R. Wilhoit, and D. Mauri, Phys. Rev. B **43**, 1297 (1991).

[5] B. Dieny, V. S. Speriosu, S. Metin, S. S. P. Parkin, B. A. Gurney, P. Baumgart, and D. R. Wilhoit, J. Appl. Phys. **69**, 4774 (1991).

[6] A. Chaiken, P. Lubitz, J. J. Krebs, G. A. Prinz, and M. Z. Harford, Appl. Phys. Lett. **59**, 240 (1991).

[7] A. Chaiken, P. Lubitz, J. J. Krebs, G. A. Prinz, and M. Z. Harford, J. Appl. Phys. **70**, 5864 (1991).

[8] M. J. Hall, B. J. Hickey, M. A. Howson, C. Hammond, M. J. Walker, D. G. Wright, D. Greig, and N. Wiser, J. Phys. Condens. Mater. **4**, L495 (1992).

[9] Y. Saito, K. Inomata, K. Yusu, A. Goto, and H. Yasuoka, Phys. Rev. B **52**, 6500 (1995).

[10] M. Suzuki, Y. Taga, A. Goto, and H. Yasuoka, J. Magn. Magn. Mater. **126**, 495 (1993).

[11] M. Suzuki and Y. Taga, J. Appl. Phys. **74**, 4660 (1993).

[12] M. Suzuki, Y. Taga, A. Goto, and H. Yasuoka, Phys. Rev. B **50**, 18580 (1994).

[13] M. Suzuki and Y. Taga, Phys. Rev. B **52**, 361 (1995).

List of Publications

[1] M. Suzuki, Y. Taga, A. Goto, and H. Yasuoka, *'The critical thickness of Fe buffer layer in giant magnetoresistance of Co/Cu superlattices'*, J. Magn. Magn. Mater. **126**, 495 (1993).

[2] M. Suzuki and Y. Taga, *'Giant magnetoresistance in Co/Cu superlattices with mixed interfaces'*, J. Appl. Phys. **74**, 4660 (1993).

[3] M. Suzuki, Y. Taga, A. Goto, and H. Yasuoka, *'X-ray diffraction and NMR study on the structure of Co/Cu superlattices with artificially modified interfaces'*, Phys. Rev. B **50**, 18580 (1994).

[4] M. Suzuki and Y. Taga, *'Role of interfacial roughness in the giant magnetoresistance in Co/Cu superlattices'*, Phys. Rev. B **52**, 361 (1995).

[5] M. Suzuki and Y. Taga, *'Influence of bound d-state on the magnetoresistance in magnetic multilayers'*, J. Phys. Condens. Mater. **7**, 8497 (1995).

[6] M. Suzuki and Y. Taga, *'Relationship between the interfacial roughness and the giant magnetoresistance in Co/Cu superlattices'*, R&D Review of TOYOTA CRDL **31**, 43 (1996).

[7] M. Suzuki, T. Ohwaki and Y. Taga, *'Durable giant magnetoresistive sensors using Co/Cu superlattices'*, Thin Solid Films **304**, 333 (1997).

[8] M. Takeda, K. Saito, Y. Endo, M. Suzuki and Y. Taga, *'Polarized neutron reflectivity measurements of Co/Cu multilayers'*, KENS report **XI**, 141 (1997).

[9] M. Suzuki and Y. Taga, 「薄膜磁気センサの一課題–界面構造と GMR–」 in 「薄膜作製応用ハンドブック」 (in Japanese), 1st ed., edited by S. Gonda, Y. Taga, T. Tsukada, and T. Hirao (NTS, Tokyo, 1995), Chap. 6, Sec. 3, p. 1065.

---

[10] M. Suzuki and Y. Taga, *'Anisotropy in the optical absorption of Ag–SiO_2 thin films with oblique columnar structure'*, J. Appl. Phys. **71**, 2848 (1992).

[11] M. Suzuki and Y. Taga, *'Optical anisotropy and columnar structure of obliquely deposited thin films containing fine particles'*, J. Non-Cryst. Solids **150**, 148 (1992).

[12] M. Suzuki and Y. Taga, *'Anisotropy in the optical absorption of metal-insulator obliquely deposited thin films –The application for an inorganic polarizer'*, R&D Review of TOYOTA CRDL **29**, 35 (1994).

[13] M. Suzuki and Y. Taga, *'Anisotropy in the optical absorption of Ag–SiO_2 thin films with oblique columnar structure'* in *Selected Papers on Linear Optical Composite Materials*, Vol. MS 120 of *SPIE Milestone Series*, edited by A. Lakhtakia (SPIE Optical Engineering Press, Washington, 1996), Chap. Sec. 3, p. 669.

[14] M. Suzuki, 「光位相差板・偏光膜」 in 「薄膜作製応用ハンドブック」 (in Japanese), 1st ed., edited by S. Gonda, Y. Taga, T. Tsukada, and T. Hirao (NTS, Tokyo, 1995), Chap. 9, Sec. 4, p. 1170.

---

[15] M. Suzuki, H. Kawauchi, K. Kimura, and M. Mannami, *'Surface Structure of SnTe(001) and PbSe/SnTe(001) Studied by RBS/Channeling of MeV He^+ Ions'*, Surface Sci. **204**, 223 (1988).

[16] Y. Fujii, K. Kimura, M. Hasegawa, M. Suzuki, Y. Susuki, and M. Mannami, *'Surface Channeling of MeV He^+ Ions on a SnTe Single Crystal'*, Nucl. Instrum. Meth. **B33**, 405 (1988).

[17] M. Hasegawa, K. Kimura, Y. Fujii, M. Suzuki, Y. Susuki, and M. Mannami, *'Secondary Electron Emission due to MeV Ions at Glancing Incidence Angles on Clean Single Crystal Surfaces'*, Nucl. Instrum. Meth. **B33**, 334 (1988).

[18] K. Kimura, M. Hasegawa, Y. Fujii, M. Suzuki, Y. Susuki, and M. Mannami, *'Specular Reflection of Fast Ions at a Single Crystal Surface'*, Nucl. Instrum. Meth. **B33**, 358 (1988).

[19] Y. Kido and M. Suzuki, *'Direct Formation of Ferromagnetic MnBi Layers with Perpendicular Magnetic Anisotropy by Ion Beam Mixing'*, Materials Letters **7**, 219 (1988).